Stony Brook University

OFFICIAL COPY

The official electronic file of this thesis or dissertation is maintained by the University Libraries on behalf of The Graduate School at Stony Brook University.

© All Rights Reserved by Author.

Mechanics of 3D Printed Architected Materials: Design, Modeling and Testing

A Dissertation Presented

by

Tiantian Li

to

The Graduate School

in Partial Fulfillment of the

Requirements

for the Degree of

Doctor of Philosophy

in

Mechanical Engineering

Stony Brook University

May 2018

Stony Brook University

The Graduate School

Tiantian Li

We, the dissertation committee for the above candidate for the

Doctor of Philosophy degree, hereby recommend

acceptance of this dissertation.

Lifeng Wang – Dissertation Advisor
Assistant Professor, Department of Mechanical Engineering

Fu-Pen Chiang - Chairperson of Defense
Professor, Department of Mechanical Engineering

Shikui Chen – Committee Member
Assistant Professor, Department of Mechanical Engineering

T. Venkatesh – Committee Member (outside)
Associate Professor, Department of Materials Science and Chemical Engineering

This dissertation is accepted by the Graduate School

Charles Taber

Dean of the Graduate School

Abstract of the Dissertation

Mechanics of advanced architected materials: Design, 3D Printing, Modeling and Testing

by

Tiantian Li

Doctor of Philosophy

in

Mechanical Engineering

Stony Brook University

2018

Architecture provides an additional degree of freedom in the design of materials and determines their mechanical properties. This dissertation presents some works on designing, fabricating, modeling and testing architected materials. The goals are to establish the relationships between the internal structure of a material and its mechanical properties and discover existing and potential new materials, especially those with improved and even ‘tunable’ properties for potential mechanical applications.

The first key objective aims at exploring the novel architected cellular materials with negative Poisson’s ratio (NPR) also named as ‘auxetics’. These materials have unusual mechanical behavior, therefore, exhibit many desirable properties and broad potential applications. However, most of studied auxetic materials are two-dimensional and exhibit NPR effect at small mechanical deformation and few of them have been fabricated to the practical stage. To solve these challenging problems, a class of architected cellular materials were created by replacing regular straight beam with sinusoidally shaped ones. These cellular materials exhibit mechanically tunable Poisson’s ratio at an extreme large tensile deformation (≥100%). Moreover, our design concept

can be extended to construct 3D periodic cellular materials by harnessing out-of-plane deformation to achieve a negative Poisson's ratio. Furthermore, a group of sandwich composites with 3D-printed auxetic cellular core materials exhibit a sequential snap-through instability under bending deformation which significantly enhances the energy absorption abilities.

The second key objective aims at discovering the structure-property-function relationships of architected multi-material composites. Combining multiple (contrasting) materials enabling to mix elastic, plastic and viscous materials could lead to completely new classes of mechanical architected materials. Here, a system of 3D periodic glassy polymer/elastomer co-continuous architected composites with different geometric arrangements of the constituents were created through simulations and experiments. These 3D periodic co-continuous composites exhibit enhanced mechanical properties including stiffness, strength, energy absorption, and fracture toughness, which are due to the mutual constraints between two phases of the co-continuous architectures. Another new group of 3D printed architected composites named auxetic composites combining with auxetic lattice reinforcement (glassy polymer) and matrix (elastomer) exhibits enhanced stiffness, hardness and toughness. This improved mechanical performance is due to the NPR effect of the auxetic reinforcements, which makes the matrix in a state of biaxial or triaxial compression and hence provides additional support.

The findings presented here will open new avenues to achieve improved and tunable mechanical properties using architected material systems.

Table of Contents

Chapter 1. Introduction 1

1.1 Background and motivation 1

1.2 Research objective 5

1.3 Outlines of this thesis 7

Chapter 2. Materials and Methods 11

2.1 Design and 3D printing technology 11

2.2 Mechanical testing 13

2.3 Numerical modeling 14

Chapter 3. 2D Lattice metamaterials with mechanical tunable Poisson’s ratio 15

3.1 Introduction 15

3.2 Materials and methods 17

    3.2.1 Description of geometric model 17

    3.2.2 Mechanical testing 19

3.3 Auxetic behavior of 2D lattice metamaterials 23

3.4 Mechanical tunable Poisson’s ratios 26

3.5 Effect of the lattice topology 29

3.6 Conclusions 31

Chapter 4. Harnessing out-of-plane deformation to design 3D architected lattice metamaterial with tunable Poisson's ratios 32

4.1 Introduction 32

4.2 Materials and methods 34

    4.2.1 Description of geometric model 34

    4.2.2 Mechanical testing 35

    4.2.3 Numerical modeling 38

4.3 Auxetic behavior of 3D planar lattice metamaterials 40

4.4 Theoretical model of the 3D planar auxetic metamaterial 43

4.5 Effect of the geometric parameters 52

4.6 Design concept extension from 1D to 3D lattice metamaterials 55

4.7 Conclusion 56

Chapter 5. The design of sandwich composites with cellular cores 58

5.1 Introduction 58

5.2 Design and fabrication of sandwich composites 60

    5.2.1 Structural design 60

    5.2.3 Mechanical testing 64

    5.2.4 Numerical simulation 65

5.3 Poisson's ratio of core design 65

5.4 Static 3point bending behavior of sandwich composites 68

  - 5.4.1 Effect of face sheets 68
  - 5.4.2 Effect of core topology 69
  - 5.4.3 Effect of relative density 77
  - 5.4.4 Discussion 83

- 5.5 Conclusions 84

Chapter 6. Enhanced mechanical performances of auxetic composites 86

- 6.1 Introduction 86
- 6.2 Design and fabrication of auxetic composites 89
  - 6.2.1 Design of auxetic lattice reinforced composites 89
  - 6.2.2 Sample fabrication 89
  - 6.2.3 Mechanical testing 91
  - 6.2.4 Finite element analysis 91
- 6.3 Compression behavior of auxetic composites 92
  - 6.3.1 Mechanical response of auxetic lattice reinforced composites 94
  - 6.3.2 Comparisons between auxetic lattice and auxetic lattice reinforced composites 100
  - 6.3.3 Effect of negative Poisson’s ratio 104
  - 6.3.4 Effect of volume fraction 108
  - 6.3.5 Discussion 113
- 6.4 Conclusion 114

Chapter 7. The fracture behavior of Interpenetration Phase Composites 116

7.1 Introduction.. 116

7.2 Design and fabrication of Interpenetration Phase Composites 118

7.3 Experiment section.. 121

7.4 Compression behavior of Interpenetration Phase Composites 124

7.5 Fracture toughness measurements 128

    7.5.1 Fracture behavior and mechanisms of IPCs.. 128

    7.5.2 Comparison between fracture behavior of IPC, PC, FC, and LC 135

7.6 Tailored fracture toughness.. 136

    7.6.1 Effect of material properties 136

    7.6.2 Effect of volume fraction 139

    7.6.3 Effect of 3D printing orientation.. 140

7.7 Conclusion 141

Chapter 8. Conclusions 143

8.1 Main contributions.. 143

8.2 Future works 146

Bibliography 150

List of Figures/Tables/Illustrations

Figure 1.1 The extraordinary properties of materials found in nature often achieved through complex structures. 2

Figure 1.2 Architecture has been used to increase the mechanical efficiency of buildings. 3

Figure 1.3 New opportunities for the design of architected materials with novel functionalities. 5

Figure 1.4 Schematic of research objective. 6

Figure 2.1 3D Printing technology. 11

Figure 2.2 Four types of architected materials and their 3D printed samples. 13

Figure 2.3 Various mechanical testing set-ups for 3D printed architected materials. 14

Figure 3.1 Schematics and deformation behavior of the sinusoidally architected lattice material. 18

Figure 3.2 Material properties of constituent 3D printed materials. 19

Figure 3.3 Experimental set-up for tension behavior of proposed 3D printed lattice material.... 20

Figure 3.4 FE model for mechanical response simulation. 23

Figure 3.5 Mechanical response of lattice metamaterials under uniaxial stretching. 25

Figure 3.6 Effects of geometric features of the ligament on the mechanical response. 27

Figure 3.7 Effects of geometric features of the ligament on stiffness and Poisson’s ratio. 28

Figure 3.8 Effect of slenderness on the stress-strain relation and Poisson’s ratios of the proposed lattice materials. 29

Figure 3.9 Effect of the topology on the stress-strain curves and Poisson’s ratio. 30

Figure 4.1 Overview of the proposed 3D planar auxetic metamaterials. 35

Figure 4.2 Material properties of constituent 3D printed materials. 36

Figure 4.3 Experimental set-up for tension behavior of proposed 3D printed lattice material.... 38

Figure 4.4 FE model for mechanical response simulation... 40

Figure 4.5 Experimental and FEA results of 3D planar auxetic metamaterials under uniaxial tensile tests... 42

Figure 4.6 Schematics of the theoretical model of the 3D planar auxetic metamaterial subject to a uniform tensile stress along horizontal stretching. 44

Figure 4.7 Schematics of the curved beam on a 2-D reference configuration............................ 45

Figure 4.8 Theoretical and FEA results of 3D planar auxetic metamaterials under uniaxial tensile tests. 51

Figure 4.9 Effect of *A/L*, *w/L*, *t/L*, and n on the macroscopic Poisson's ratio of the 3D planar metamaterials, v_{yx}. Evolution of v_{yx} as a function of *A/L*. 54

Figure 4.10 The system of lattice metamaterials with curved beams. 56

Figure 5.1 Design of unit cell of the truss, conventional honeycomb, and re-entrant honeycomb structure.. 61

Figure 5.2 Three-point bending test set-up and the sandwich samples. 63

Figure 5.3 Three cellular core materials under uniaxial compression test (the volume fraction is 20%)... 67

Figure 5.4 Bending characteristic of sandwich composite specimens with face sheets of different materials... 69

Figure 5.5 Bending characteristic of sandwich composite specimens with different core structures and U-CFRP face sheets. 72

Figure 5.6 Comparison of the experiments and FEA predications for mechanical response of sandwich composites under bending deformation.. 74

Figure 5.7 Bending characteristic of sandwich composite specimens with re-entrant honeycomb core design and U-CFRP face sheets. 77

Figure 5.8 Bending properties of the sandwich structures. 79

Figure 6.1 Schematics of lattice structures, lattice reinforced composite structures and 3D-printed lattice reinforced composite specimens. 90

Figure 6.2 The stress-strain response of 3D printed constituent materials. 93

Figure 6.3 Mechanical response of the 3D-printed lattice reinforced composites during uniaxial compression tests. 95

Figure 6.4 Experimental images of deformation and the calculated Poisson's ratios for each composite design. 98

Figure 6.5 Experimental displacement contours for each composite design. 100

Figure 6.6 The comparison of mechanical properties for the lattice reinforced composites and the lattice counterpart structures are shown. 102

Figure 6.7 The von Mises stress distribution in the lattice reinforced composites and the corresponding cellular structures at a nominal compressive strain of 0.05. 104

Figure 6.8 Effect of Poisson's ratio on the mechanical properties of various honeycomb reinforced composites during the uniaxial compression test. 107

Figure 6.9 The stress-strain responses of four types of composites at different volume fractions of the reinforcing phase. 109

Figure 6.10 Comparison of mechanical properties of the lattice reinforced composites as a function of the volume fraction of reinforcement phase: (a) Young's modulus, (b) energy absorption. 112

Figure 7.1 Schematics of 3D IPCs with different lattice symmetries. 120

Figure 7.2 Mechanical response of 3D printed composites during uniaxial compression tests. 127

Figure 7.3 3-point bending tests of the SENB specimens.. 129

Figure 7.4 3-point bending tests of the SENB specimens of IPC-BCC and IPC-FCC.............. 132

Figure 7.5 Representative responses of IPC SENB samples with SC, BCC and FCC lattice symmetries showing the load as a function of (a) the load line displacement, and (b) the crack mouth opening displacement, δ. The crack-growth (c) J-integral, JIC and (d) and fracture toughness, KJIC are plotted as a function of crack extension, Δa, for IPC SENB samples, respectively. 133

Figure 7.6 3-point bending tests of the SENB specimens of IPCs, PCs, FCs and LCs. 136

Figure 7.7 The effect of stiffness ratio, EB/EA, on the mechanical response of FCC IPCs...... 138

Figure 7.8 The effect of the volume fraction of material A on the mechanical response of FCC IPCs. 140

Acknowledgments

First, I would like to express my deep gratitude towards my advisor, Professor Lifeng Wang, who gave me this great opportunity to pursue my PhD degree. Without his continuous encouragements and mentoring, I won't be able to complete this thesis timely. I also would like to thank my thesis committee members, Professor Fu-pen Chiang, Professor Shikui Chen, and Professor T. Venkatesh, whose insightful comments were a tremendous help to improve this thesis.

I highly appreciate the department of Mechanical engineering at Stony Brook University, where I received great course learning and research training. I would also like to thank Professor Toshio Nakamura, Professor Foluso Ladeinde, Professor Sam Huang, Professor Maen Alkhader and Professor Lei Zuo for their intellectual instruction of graduate courses and lectures.

I would also like to thank all my collaborators: Dr. Yanyu Chen, Professor Fu-pen Chiang, Professor Shikui Chen, Professor Fabrizio Scarpa, Professor Nicholas Fang, Professor Howon Lee, Professor Yangbo Li, Nicolas Casazzone, Dr. Shuyu Wang, Zian Jia, Professor Arash Afshar, Xuedong Zhai, Panagiotis Vogiatzis, Yue Wang, Shaoyu Hou, Mang Zhang and Fan Liu. I have benefited substantially from the discussions and exchange of ideas with them.

Also, I would like to take this opportunity to thank Dr. Shuyu Wang, Gwen Wright, Dr. Ming Lu, and Dr. Charles Black who provided assistance for conducting the experiments in Brookhaven National Lab. My experiments could not have been carried out smoothly without their support.

I would also like to thank my undergraduate supervisor Professor Jingfeng Li, Professor Zhengcao Li and my master supervisor Professor Koichi Tsuchiya. Without their significant support, I could

not have this precious opportunity to come to US and study for my PhD degree here. I am very grateful for the financial support from the SUNY at Stony Brook, NSF and ONR.

Last but not least, I would like to express my sincerest and deepest gratitude to my parents for their devoted love and understanding. I would like to give my special thanks to my girlfriend Xiaoyi Hu, whose selfless love, deep care and constant supports enable me to complete this thesis.

Vita, Publications and/or Fields of Study

1. Panagiotis Vogiatzis, Shikui Chen, Xiao Wang, **Tiantian Li** and Lifeng Wang. "Topology optimization of multi-material negative Poisson's ratio metamaterials using a reconciled level set method", Computer-Aided Design, 2017, 83, P. 15-32.

2. Yanyu Chen, **Tiantian Li**, Fabrizio Scarpa and Lifeng Wang. "Lattice Metamaterials with Mechanically Tunable Poisson's Ratio for Vibration Control", Physical Review Applied, 2017, 7(2): 024012.

3. **Tiantian Li** and Lifeng Wang. "Bending behavior of sandwich composite structures with tunable 3D-printed core materials", Composite Structures, 2017,175, P.46-57.

4. **Tiantian Li**, Xiaoyi Hu, Yanyu Chen and Lifeng Wang. "Harnessing out-of-plane deformation to design 3D architected lattice metamaterials with tunable Poisson's ratio", Scientific Reports, 2017, 7(8949).

5. Yanyu Chen, **Tiantian Li**, Zian Jia, Fabrizio Scarpa, Chun-Wei Yao and Lifeng Wang. "3D printed hierarchical honeycombs with shape integrity under large compressive deformations", Materials & Design, 2018, 137, P.226-234.

6. Zian Jia, **Tiantian Li**, Fu-pen Chiang and Lifeng Wang. "An experimental investigation of the temperature effect on the mechanics of carbon fiber reinforced polymer composites", Composite Science and Technology, 2018, 154, P.53-63.

7. **Tiantian Li**, Yanyu Chen, Xiaoyi Hu, Yangbo Li and Lifeng Wang. "Exploiting negative Poisson's ratio effect to design 3D-printed composites with enhanced mechanical performance", Materials & Design, 2018, 142, P.247-258.

8. Yangbo Li, Yanyu Chen, **Tiantian Li**, Siyu Cao and Lifeng Wang. "Hoberman-sphere-inspired lattice metamaterials with tunable negative thermal expansion", Composite Structures, 2018, 189, P. 586-597.

9. **Tiantian Li**, Yanyu Chen and Lifeng Wang. "Enhanced fracture toughness in 3D printed architected interpenetrating phase composites", submitted, 2018.

Chapter 1. Introduction

The research in this thesis lies with the area of architected material design, 3D printing, mechanical testing, analytical and numerical modeling. The theme is establishing the relationships between the internal structure of a material and its mechanical properties and discovering existing and potential new materials, especially those with improved and even tailorable properties for potential mechanical applications. The background, motivation, research objective and the outline of this thesis will be addressed in this chapter.

1.1 Background and motivation

Architecture has played an important role in not only human-made structures such as buildings, tools, transportations but also natural materials such as bone, nacre, tissues in plants and among others. Nature evolved architected materials for many situations in which low density as well as high stiffness and strength are needed. Examples are the beaks and bones of birds that consist of thin, solid skins attached to a highly porous, cellular core. The complex core structures are producing an efficient structure for resisting bending and buckling loads with little increase in weight. Moreover, researchers found that in nature the complex structures can achieve some extraordinary properties of materials. (Figure 1.1) For example, the deep-sea sponge has a square lattice cage-like structures with hierarchical levels which can not only provide lightweight, high stiffness and strength but also overcome the brittleness of its constituent material [1]. Another example is from the Morpho butterfly, which uses multiple layers of cuticle structures to produce their striking blue color which is also a natural photonic structure [2]. The third example is the feet of Gecko with hierarchical fiber structures which provide a good ability of adhesion [3]. Therefore, nature usually use architecture to achieve functionality.

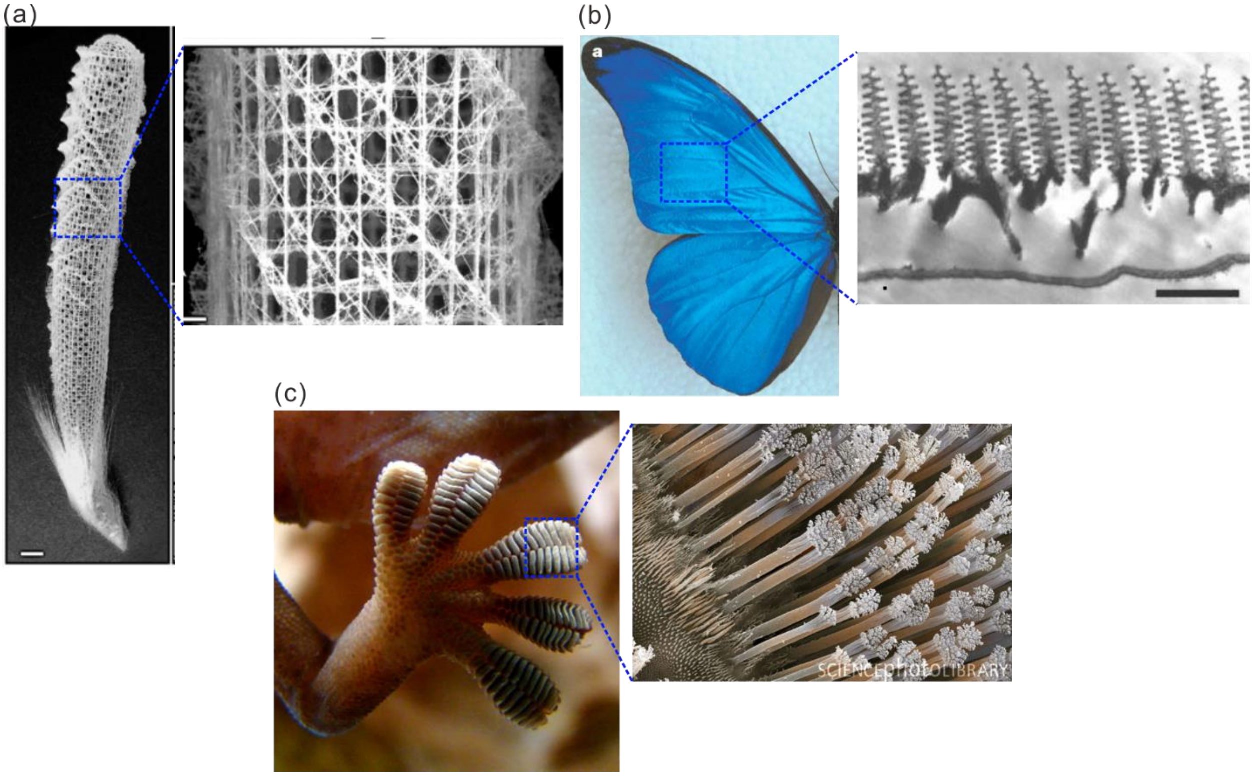

Figure 1.1 The extraordinary properties of materials found in nature often achieved through complex structures. (a) Deep-sea sponge has a square lattice cage-like structures with hierarchical structures which can overcome the brittleness of its constituent material. (b) Morpho butterfly uses multiple layers of cuticle structures to produce their striking blue color which is also a natural photonic structure. (c) Gecko feet have hierarchical fiber structures to achieve adhesion.

Architecture has also played an important role in human society. Humankind always has the knowledge to develop architectures to enhance the structural efficiency. The good examples are from the revolution of buildings over centuries. From the Pyramids of Giza in 2500 BC to St. Peter's Basilica in 1500 AD and from the Eiffel Tower in 1880 AD to the highest building Burj Khalifa today, it can be found that the modern buildings have a superior architecture in which more than 99.8 % of the material has been replaced with air. In large scale, we are able to use architectures to increase the mechanical efficiency of buildings and many other familiar structures.

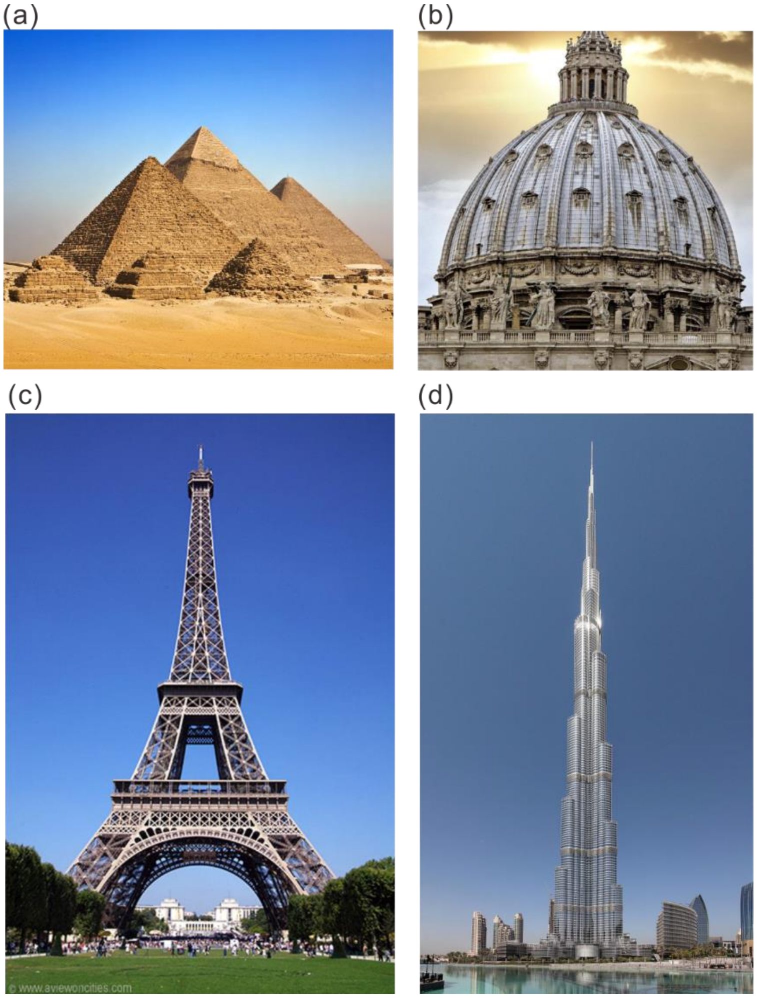

Figure 1.2 Architecture has been used to increase the mechanical efficiency of buildings. (a) Pyramids of Giza, 2500 BC; (b) St Peter's Basilica, 1500 AD; (c) Eiffel Tower, 1880 AD; (d) Burj Khalifa, 2009 AD.

The same engineering and architectural principles that have been used to increase the mechanical efficiency of structures can be applied at the material scale. Modern materials with complex architecture can achieve higher structural efficiency. Furthermore, architecture provides an additional degree of freedom in the design of a material. In recent years, there are many new opportunities for the design of architected materials with novel functionalities. This is because the computational power and computational methods have improved enough to enable design and simulation of materials and structures with complex architecture. Moreover, the emergence of additive manufacturing technologies enables fabrication of materials with more complex architectures, and many novel architected materials have been created over the last few years and some of them exhibit novel functionalities. Figure 1.3 exhibits several top of novel functionality of architected materials. Researchers from Prof. Greer's group can fabricate the hierarchical lattice structures [4] in micro even nano meters level and these hollow ceramic lattice structures exhibit enhanced mechanical performances including strength, stiffness and superior recovery ability (Figure 1.3 (a)). Figure 1.3 (b) shows the architected metamaterial by using the geometry non-linearity to achieve programmable shape-shifters when uniaxially compressed from Prof. Hecke's group [5]. By combining the 3D printed composite hydrogel architectures with localized, anisotropic swelling behavior, researchers in Prof. Lewis's group generated a shape-morphing system [6] by biomimetic 4D printing (Figure 1.3 (c)). Researchers introduce deterministic routes to hard and soft structural composites with architecture design [7] that can be tailored precisely to match the non-linear properties of biological tissues, with application opportunities that range from soft biomedical devices to constructs for tissue engineering (Figure 1.4 (d)). Moreover, researchers in Professor Studart group report a 3D printing platform for the seamless digital fabrication of robotic soft actuators with bioinspired architectures exhibiting programmable motions [8] (Figure 1.4 (e)). Furthermore, the material scientist even designed the microstructures of steel with hierarchical and laminated, similar to the substructure of bone, realizing the superior crack resistance [9] (Figure 1.4 (f)). Above all, the developing of advanced additive manufacturing methods combining with powerful computational optimization and simulation provide the many opportunities for the design of architected materials with novel functionalities.

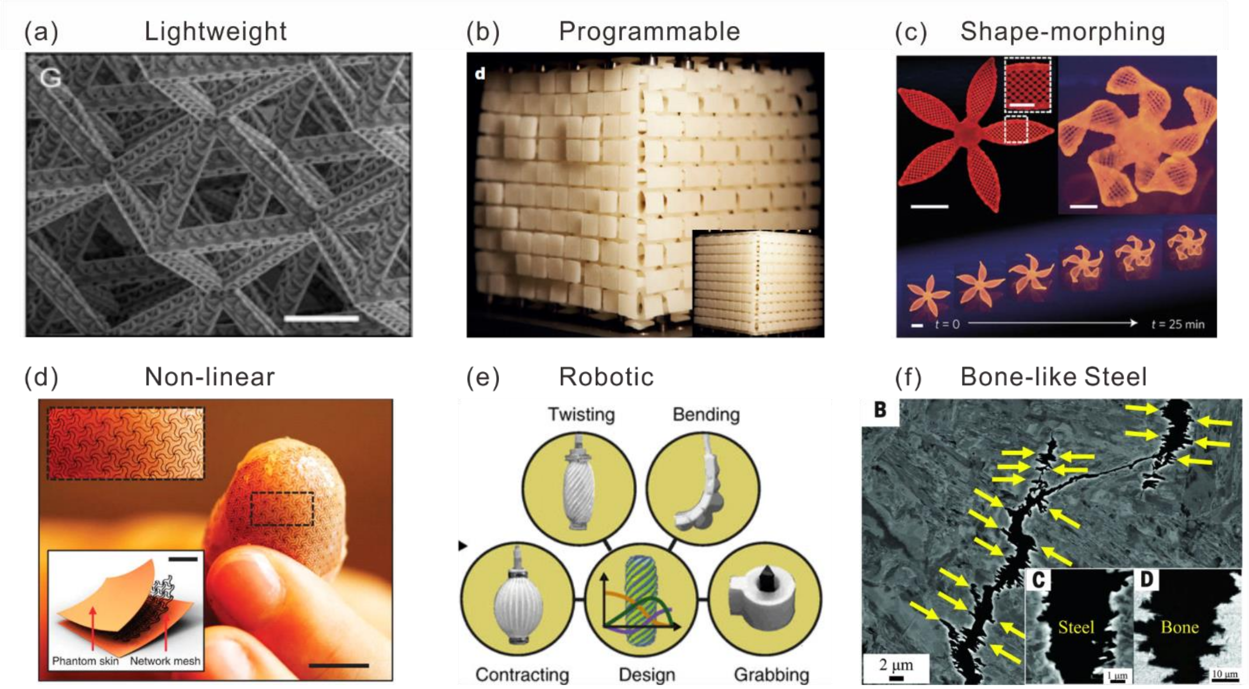

Figure 1.3 New opportunities for the design of architected materials with novel functionalities.

1.2 Research objective

The overall research objective for this thesis is combining the architectures, materials and additive manufacturing to achieve the architected materials with superior performance. On one hand, various architectures of materials will be tailored including the cellular, lattice structures, bio-inspired structures, hierarchical structures, particle, fiber or laminate reinforced composites, co-continuous phases even aperiodic structures with defects. On another hand, the different constituent materials will be utilized including polymer, ceramics, carbon, metals, composites and cells. Combining the developing additive manufacturing methods to achieve three aspects of superior performances of architected materials. The first aspect involves materials with improved mechanical properties such as light weight, enhanced stiffness, strength, toughness, hardness, energy dissipation and damage tolerance. The second aspect involved materials with unusual and tunable properties such as negative Poisson's ratio, negative thermal expansion, negative compressibility and negative stiffness. The third aspect of properties are the multi-functionality of materials including thermoelectric, piezoelectric, shape memory, soft activate, soft robotic and programmable materials.

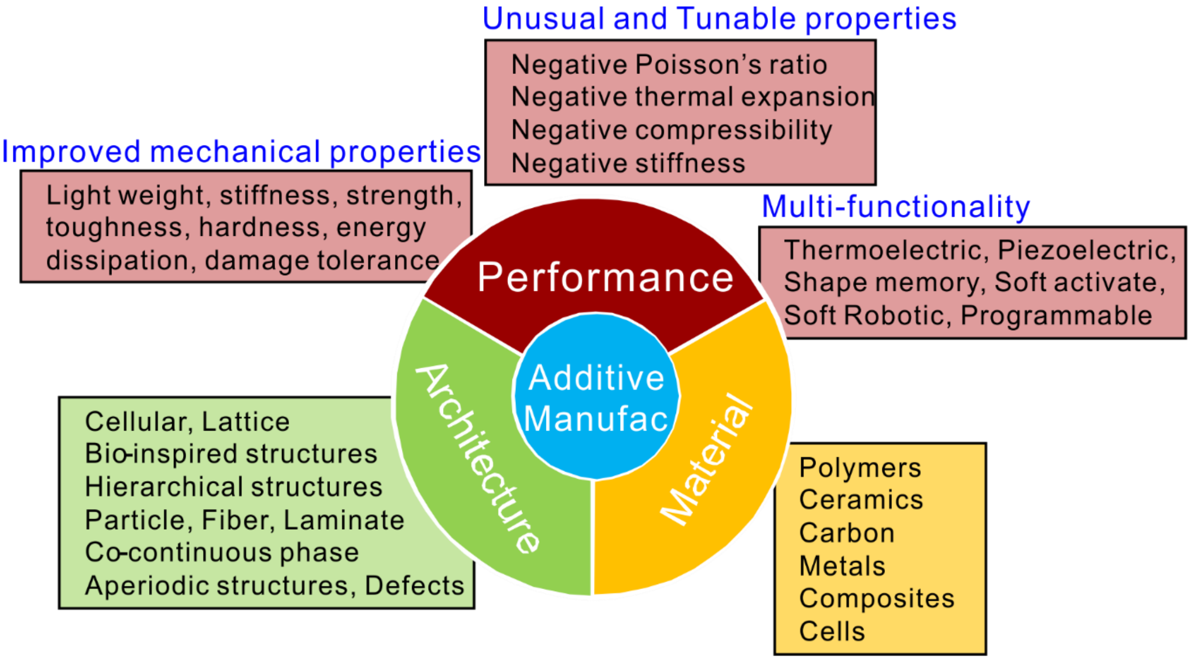

Figure 1.4 Schematic of research objective.

The research objectives and approaches for this thesis are shown in Figure 1.5. Specifically, the optimally architected materials should have tunable mechanical properties, such as tunable Poisson's ratio. In addition, the architected materials with enhanced energy dissipation ability will be explored. Importantly, excellent mechanical properties such as stiffness, toughness, hardness, crack resistance will be considered in the architected materials design. These research objectives will be accomplished by integrating architecture design, 3D printing, mechanical testing and modeling including theoretical and numerical analysis.

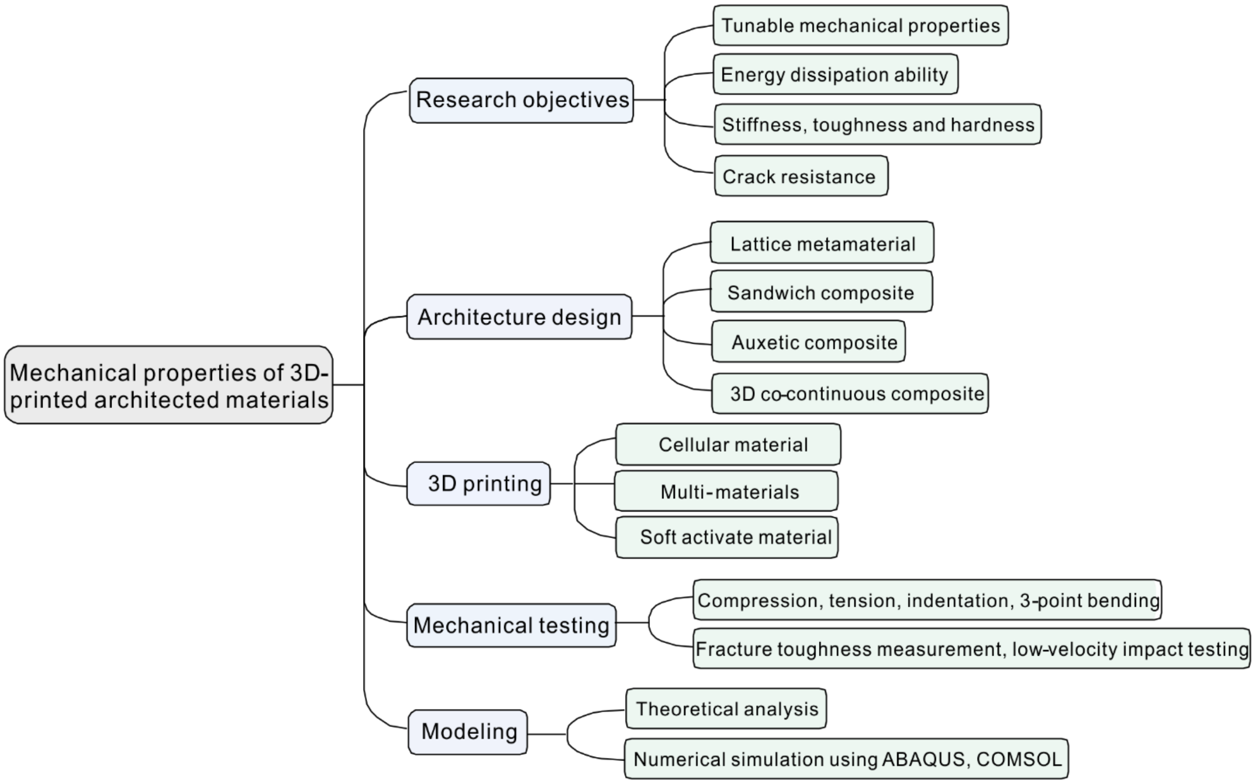

Figure 1.5 Flow chart of the specific objectives and approaches of this thesis.

1.3 Outlines of this thesis

In this these, it will be experimentally and numerically demonstrated that enhanced mechanical performance and novel mechanical properties can be simultaneously achieved using architected material designs and additive manufacturing (3D printing).

In Chapter 2, I will briefly introduce the 3D printing technology involved in this thesis. Four types of rationally designed architected materials will be proposed to achieve various novel mechanical performance. In addition, various experimental testing methods and numerical methods will also be briefly introduced.

In Chapter 3, a classes of stretchable lattice metamaterials with mechanically tunable negative Poisson's ratios will be presented. The proposed architected lattice materials are built by replacing regular straight beams with sinusoidally shaped ones in plane direction, which are highly stretchable under uniaxial tension. Numerical and experimental results indicate that the proposed lattice metamaterials exhibit Poisson's ratios varying between -0.7 and 0.5 over large tensile deformations up to 50%. This large variation of Poisson's ratio values is attributed to the deformation pattern switching from bending to stretching with the sinusoidally shaped beams.

In Chapter 4, a 3D architected lattice system showing a negative Poisson's ratio over a wide range of applied uniaxial stretch was presented. 3D printing, experimental tests, numerical simulation, and analytical modeling are implemented to quantify the evolution of the Poisson's ratio and reveal the underlying mechanisms responsible for this unusual behavior. The auxetic behavior can be controlled by tailoring the geometric features of the ligaments.

In Chapter 5, we combine 3D printing technique, numerical analysis, and experiments to design a new class of sandwich composites that exhibit various bending behaviors. These programmed sandwich structures contain 3D printed core materials with truss, conventional honeycomb and re-entrant honeycomb topologies. Under bending deformation, sandwich composites with truss core materials provide highest flexural stiffness and strength that are desirable in structural components. The sandwich composites with re-entrant honeycomb core exhibit a sequential snap-through instability which significantly enhances the energy absorption abilities. The experimental and numerical results indicate that architected core structures can be utilized to tailor the bending properties as well as failure mechanism.

In Chapter 6, a class of high-performance composites in which auxetic lattice structures are used as the reinforcements and the nearly incompressible soft material is employed as the matrix. This coupled geometry and material design concept is enabled by the state-of-the-art additive manufacturing technique. Guide by experimental tests and finite element analyses, we systematically study the compressive behavior and the static and dynamic indentation behavior of the 3D printed auxetics reinforced composites and achieve a significant enhancement of their stiffness, energy absorption, indentation stiffness and impact resistance. These improved mechanical performance is first due to the negative Poisson's ratio effect of the auxetic reinforcements, which makes the matrix in a state of biaxial compression under compression or indentation and hence provides additional support. Another mechanism for enhanced indentation behavior is due to the negative Poisson's ratio effect of the overall auxetic composites, which makes the composites denser at the site of the impact and therefore more resistant to indentation. Combining experimental tests and numerical simulation, we conclude that auxetic structures can lead to design stiffer, harder and tougher composite materials.

In Chapter 7, a class of Interpenetrating phase composite (IPC), also known as co-continuous composite are fabricated by 3D printing with rationally designed architectures which exhibit a fracture toughness 16 times that of conventionally structured composites. The toughening mechanisms arise from the plastic deformation and stretching of the hard phase that bridges the advancing crack, which is intrinsically controlled by the rationally designed interpenetrating architectures. The prominently enhanced fracture toughness in the architected IPCs can be tuned by tailoring the stiffness contrasts between the compositions.

Finally, main contributions, broad impacts, and future work will be briefly illustrated in Chapter 8.

Chapter 2. Materials and Methods

In this thesis, all specimens for architected materials used in the study have been printed by using an Objet Connex260 multi-material 3D printer (Stratasys) (Figure 2.1). Tango plus and Verowhite will be used as the constitutive materials for the samples. The chemistry of these materials is proprietary to Stratasys. This 3D printing system can fabricate multi-materials simultaneously. Figure 2.1 (b) shows the cellular structures with one constituent material and the composite specimens with multi-materials. This 3D printer can fabricate samples with high resolution of 16 μm at relative low cost and short time. However, within the limitation of 3D printing technology, the layer orientation was found to influence the mechanical properties of the materials; therefore, all the specimens were printed along the same orientation on the printer build platform. The as-fabricated specimens were kept at room temperature for 7 days to allow for the saturation of the curing. The detailed dimensions and topologies for 3D printed can be found in each chapter.

2.1 Design and 3D printing technology

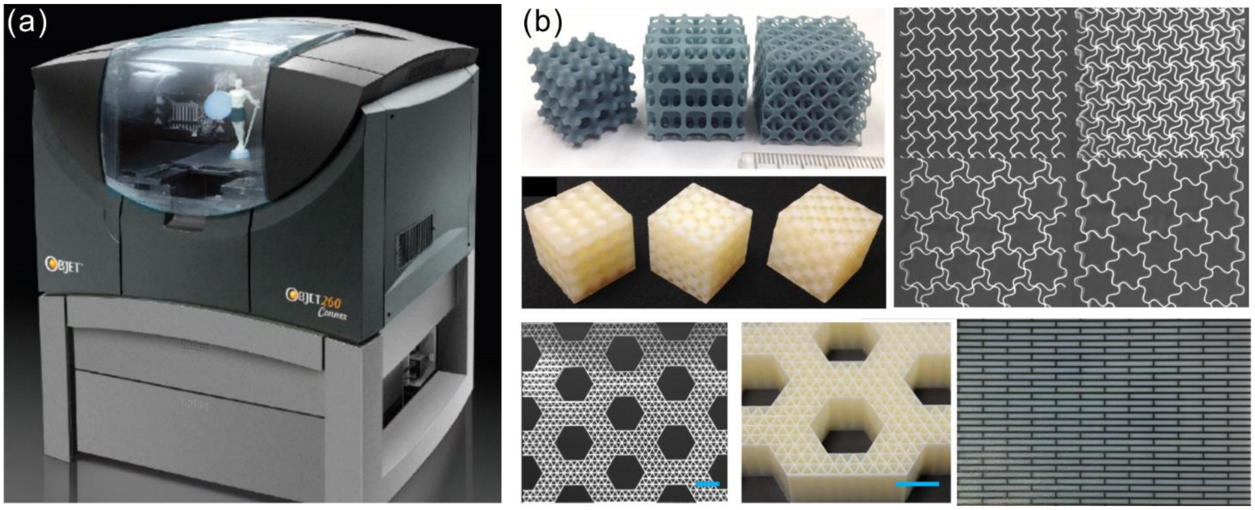

Figure 2.1 3D Printing technology. (a) The Stratasys Objet series 3d printing system and (b) various architected materials fabricated using this 3d printing system.

Here four types of architected materials will be designed: 1) *Lattice metamaterials*. As will be shown in Chapter 3 and Chapter 4, we designed and fabricated a class of 2D and 3D lattice metamaterial with pre-curved ligaments, aiming at achieving novel mechanical performance such as large stretchability, tunable negative Poisson's ratio (Figure 2.2 (a)). 2) *Sandwich composites*. As will be shown in Chapter 5, sandwich composites combining CFRP as face sheet and 3D printed cellular core exhibit tailorable bending performance. Especially, the sandwich composites with re-entrant honeycomb cores structures show a sequential snap-through instability which significantly enhances the energy absorption abilities (Figure 2.2 (b)). 3) *Auxetic composites*. The first two architected materials are cellular materials, where their properties are most relying on their architected structures. In addition, in many applications, multi-material design such as composites will exhibit multi-functionalities, which is highly essential. In this regard, composite materials have great potential applications. Here a group of composites with auxetic structures as the reinforcement will be created (Figure 2.2 (c)). As will be shown in Chapter 6, auxetic composites exhibit enhanced stiffness, hardness, toughness and impact resistance compared to other lattice reinforced composites. 4) *3D co-continuous composites*. As will be shown in Chapter 7, we proposed that the 3D co-continuous composites exhibit a fracture toughness 16 times that of conventionally structured composites. The toughening mechanisms arise from the plastic deformation and stretching of the hard phase that bridges the advancing crack, which is intrinsically controlled by the rationally designed interpenetrating architectures. The prominently enhanced fracture toughness in the architected IPCs can be tuned by tailoring the stiffness contrasts between the compositions (Figure 2.2 (d)).

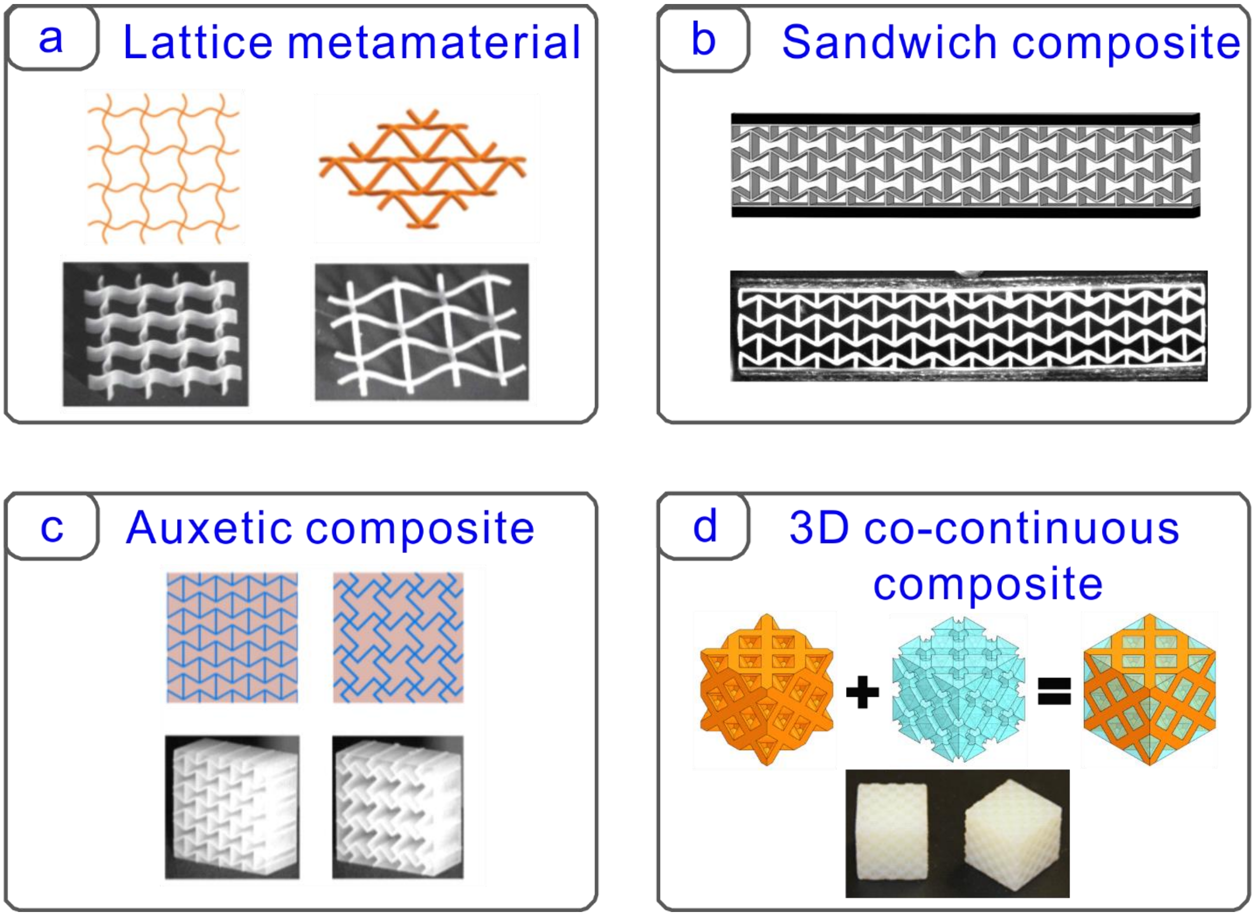

Figure 2.2 Four types of architected materials and their 3D printed samples. (a) Lattice metamaterials, (b) sandwich composites, (c) auxetic composites, (d) 3D co-continuous composites.

2.2 Mechanical testing

To evaluate the mechanical properties of these architected materials, various mechanical testing will be performed. Here we conducted uniaxial tensile testing, uniaxial compressive testing, indentation testing, 3point bending testing and impact testing by using MTS, Instron, and Hopkins Bar mechanical testers. High speed cameras were used to capture the deformation figures of each samples. For some certain specimen, speckles were sprayed on the samples using a spray paint for digital image correlation (DIC) measurements. The deformation and local strain contours of the samples were tracked and processed by using DIC (Vic-2D, Correlated Solution) to acquire the strains of the specimen surfaces. More details for specific experiments can be found in each chapter.

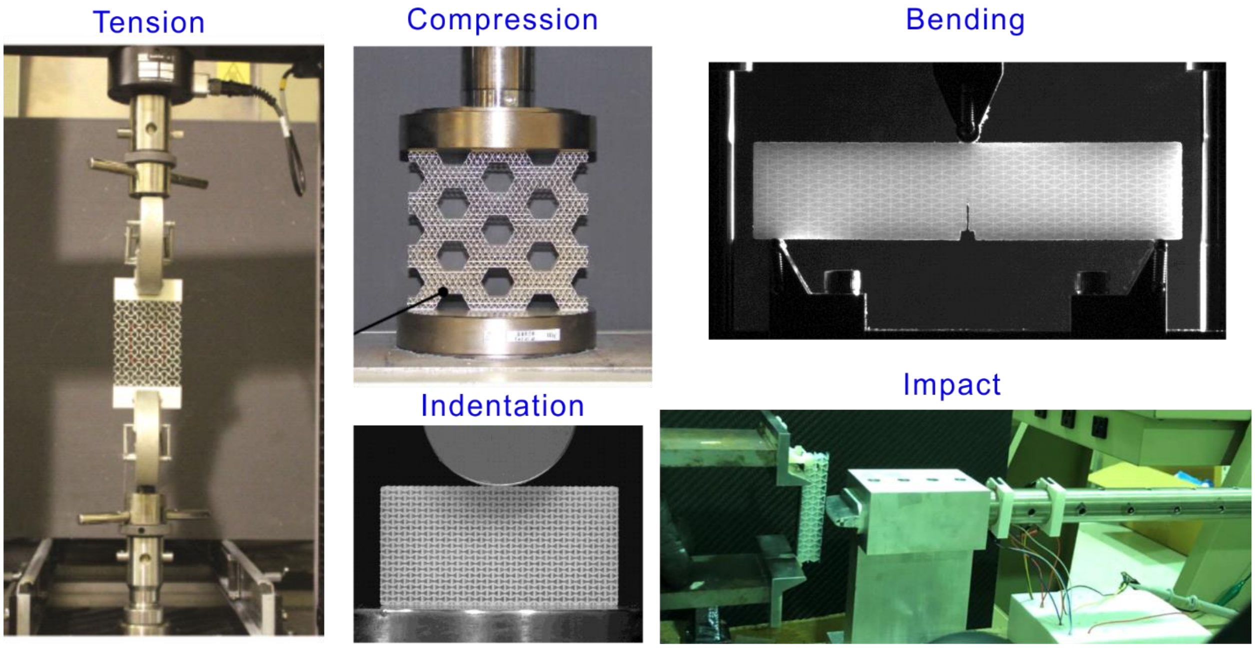

Figure 2.3 Various mechanical testing set-ups for 3D printed architected materials.

2.3 Numerical modeling

The numerical simulations related to the mechanical response of these architected materials are conducted using commercial FE package ABAQUS/Standard (Simulia, Providence, RI). The detailed numerical modeling methods can be found in each chapter.

Chapter 3. 2D Lattice metamaterials with mechanical tunable Poisson's ratio

3.1 Introduction

Metamaterials are rationally designed multiscale structural systems whose unusual equivalent physical properties are dictated by their architectures rather than compositions. Metamaterials have recently attracted significant interest within the research community because of the need to develop various classes of novel properties and broad ranges of potential applications.[10-15] For example, metamaterials with artificially designed architectures can exhibit a negative refractive index that is unattainable for conventional materials.[16-18] The metamaterial concept has been rapidly extended from photonic systems to acoustic[19-22] and mechanical systems.[23-26] Among them, mechanical metamaterials having a negative Poisson's ratio (NPR) are of particular interest.[13,27-32] Most materials (both isotropic and anisotropic) exhibit positive Poisson's ratios, however the existence of negative Poisson's ratios is still permitted under the tenets of the classic theory of elasticity. Materials with a negative Poisson's ratio that will contract (expand) transversally when they are axially compressed (stretched) are also called auxetics.[33-37] Auxetic behavior has been observed in a variety of natural systems, including cubic metals,[38] zeolites,[39,40] natural layered ceramics,[41] silicon dioxides,[42] single-layer graphene,[43,44] and 2D protein crystals.[45] Following the seminal work of Lakes,[36] a significant body of research work has been established to develop materials with a negative Poisson's ratio. For example, the auxetic behavior of materials provides a wrapping effect around a penetrating object when subjected to indentation, a feature that may be useful in protective and blast engineering applications.[15,46] Several microstructure architectures and deformation mechanisms have been developed to obtain the auxetic behavior. Between the various architectures it is worth to note dimpled and perforated elastic sheets,[47] origami/Kirigami-based metamaterials,[27,48,49] hierarchical metamaterials with fractal cuts,[50] and foams.[51-55] Auxetic materials and structures are intrinsically multifunctional because of the coupling originated between their unusual deformation mechanisms and their multiphysics behavior. For example, piezoresistive sensors with a NPR substrate demonstrate a 300% improvement in piezoresistive sensitivity, making them capable of multimodal sensing.[55]

Most of the theoretical and experimental investigations related to NPR cellular materials are related to microstructure configurations with straight ligament topologies. Recent numerical and experimental studies indicate that thin film materials with serpentine microstructures can have improved stretchability, owing to the introduced microstructure and small intrinsic strain in the materials [56-59]**.** A non-straight (corrugated) rib configuration for open cell polyurethane foams has also recently been considered as a likely explanation for the existence of an unusual blocked shape memory effect in auxetic open cell polyurethane foams.[60] Although it has been theoretically shown that the auxetic behavior can also be attained in hierarchically architected lattice materials with triangular topology,[57] convincing experimental evidence of the auxetic behavior of these materials has not been reported. Moreover, no theoretical and numerical evidence exist about the performance of engineered auxetic metamaterial lattices with sinusoidally (non-straight) ligaments in their microstructure, especially at hierarchical level. The goal of this work is to investigate the auxetic behavior and vibration control capability of one of these materials by combining computational modeling with 3D printing techniques and related experimental results.

3.2 Materials and methods

3.2.1 Description of geometric model

We begin by characterizing the geometric features of the proposed sinusoidally architected lattice material. A schematic of our 2D lattice microstructure with auxetic behavior is illustrated in Figures 3.1 (a) – (c). The shape of the sinusoidal beams can be mathematically described as $y = A_n \sin\left(n\pi x/l\right)$, where A_n is the wave amplitude, *n* is the number of half wavelength, and *l* is the length of regular beam. The length of sinusoidal beam is given by:

$$s = \int_0^l \sqrt{1+\left(y'\right)^2}\,dx = \int_0^l \sqrt{1+\left(\frac{A_n n\pi}{l}\cos\left(\frac{n\pi x}{l}\right)\right)^2}\,dx\,, \tag{1}$$

Under the mass equivalence assumption, the width of the sinusoidal beams can be calculated as

$$w = t\cdot l \Bigg/ \int_0^l \sqrt{1+\left(\frac{A_n n\pi}{l}\cos\left(\frac{n\pi x}{l}\right)\right)^2}\,dx\,, \tag{2}$$

Then, for a given $A_n n/l$, the width of the sinusoidal beam is the same for any *n*.

The proposed lattice materials are fabricated using a 3D printer (Objet Connex260, Stratasys). To ensure the stretchability of the lattice materials, a rubber-like material, Shore 95, is taken as the constitutive (core) material for the sinusoidal beams. Details on the fabrication of the specimens and the mechanical behavior of the core material can be found in the Supporting Information. Figure 3.1 (d) shows the center area of the specimen, which consists of an array of 4×5 unit cells with $A_n n/l = 1/3$ and *n*=1 and a representative sequence of images taken at different tensile strains. By simple inspection it is evident that at a small initial strain the lattice material expands transversally, indicating therefore the presence of an auxetic behavior. However, when the macroscopic tensile strain increases to 30%, the lattice material contracts along the *x* direction. These phenomena suggest that the fabricated 2D lattice materials exhibit auxetic behavior and a strain-dependent Poisson's ratio.

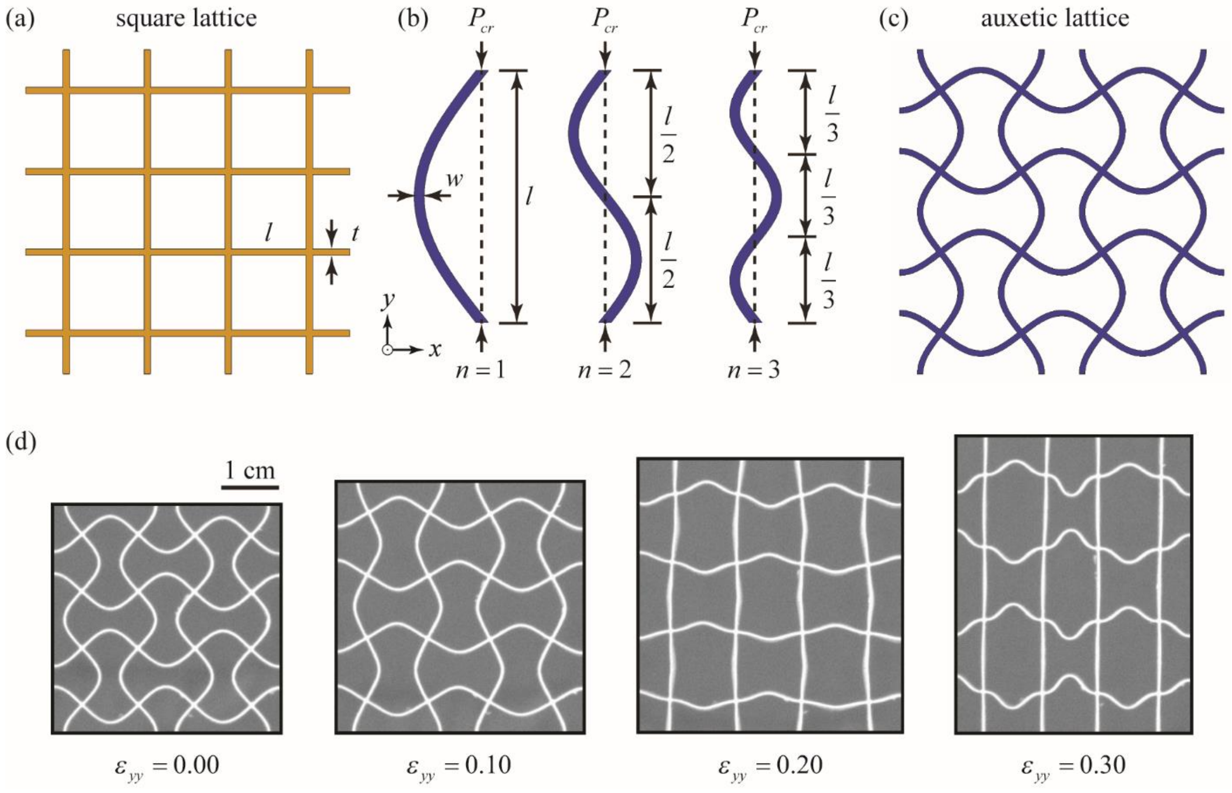

Figure 3.1 Schematics and deformation behavior of the sinusoidally architected lattice material. (a) Regular square lattice with 2×2 unit cells. Here *t* and *l* are the width and length of regular beams. (b) Buckling modes of a single beam under compression. (c) Proposed architected lattice materials with 2×2 unit cells with *n*=1; (d) Deformation behavior of the center area consisting of 2×2 unit cells of the architected lattice material under uniaxial tension.

3.2.2 Mechanical testing

The material properties of the Shore 95 rubber-like material were obtained by measuring the mechanical response of the 3D printed dogbone. The experimental setup is shown in Figure 3.2 (a). Figure 3.2 (b) shows the measured stress-strain curves (true and engineering strain) under uniaxial tension. According to ASTM 412, the basic properties of Shore 95 are characterized by a Young's modulus of E=5.5 MPa, Poisson's ratio ν=0.37, and density ρ=1157 kg/m^3.

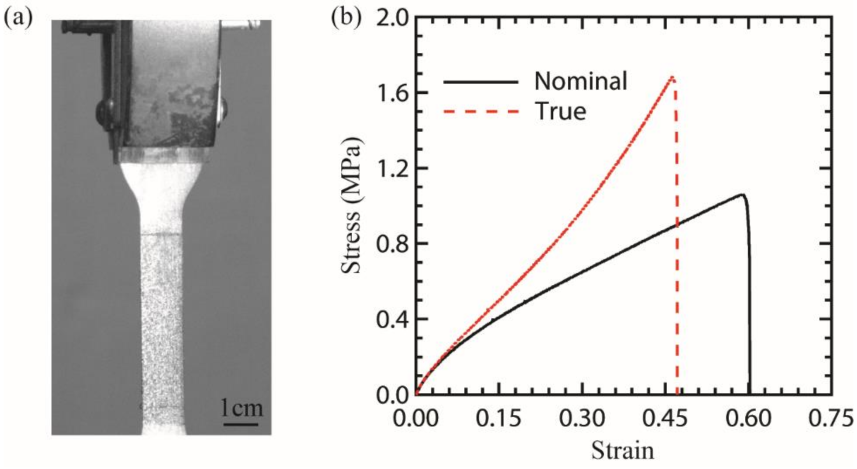

Figure 3.2 Material properties of constituent 3D printed materials. (a) 3D printed dogbone specimen under uniaxial tension. (b) Measured stress-strain relation of the dogbone specimen.

The experimental setup of the tensile testing is shown in Figure 3.3 (a). Uniaxial tensile testing was performed using a MTS mechanical tester (C43) with a 1 kN load cell. All experiments were conducted in a quasi-static regime with a constant strain rate of 0.001 s^{-1}. The load-displacement curves measured from the uniaxial tensile tests were then transferred into nominal stress- strain behaviors based on the measured dimensions of the specimens. Images of the specimens at various loading conditions were taken at a rate of 1 FPS (VicSnap, Correlated Solution). For the dogbone specimen, speckles were sprayed on the samples using a spray paint for digital image correlation (DIC) measurements. The deformation and local strain contours of the samples were tracked by using DIC (Vic-2D, Correlated Solution) to calibrate the nominal stress- strain curves and to obtain the Poisson's ratio of the constitutive material.

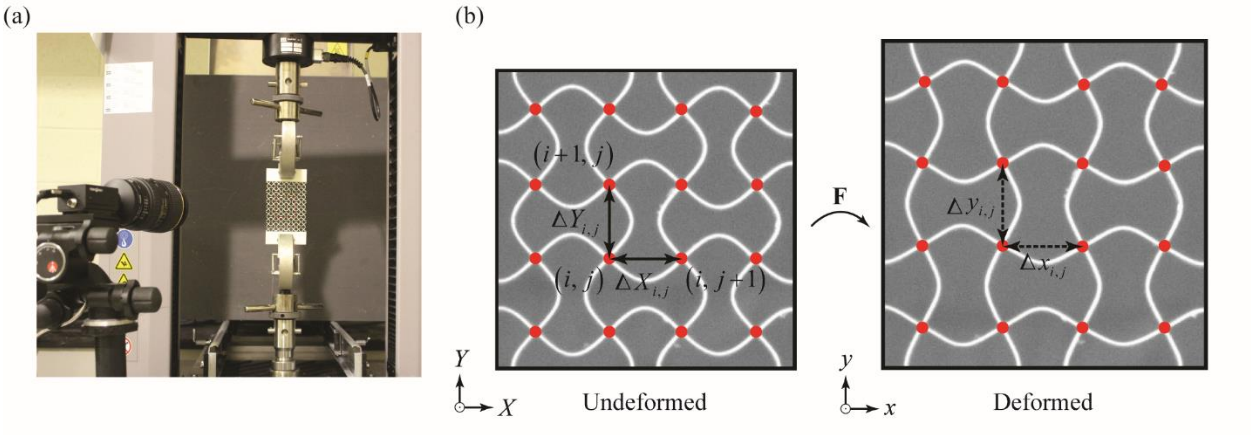

Figure 3.3 Experimental set-up for tension behavior of proposed 3D printed lattice material. (a) Experimental setup of the lattice specimen under uniaxial tension. (b) Calculation of Poisson's ratio.

To quantify the deformation taking place in the lattice materials during the experiments an image processing software (ImageJ) was used to determine the intersection points in the specimen. The deformation near the four edges of the specimen was strongly affected by boundary conditions. Therefore we focused on the behavior of nine unit cells in the central part of the specimens. The intersection points at the corners of the chosen unit cells were determined as $\left(X_{i,j}, Y_{i,j}\right)$ in the undeformed and $\left(x_{i,j}, y_{i,j}\right)$ in the deformed state, respectively. The row and the column indices vary between $1 < i < 4$ and $1 < j < 4$. For each unit cell, the horizontal and vertical distances were calculated from the coordinates $\left(x_{i,j}, y_{i,j}\right)$, i.e., $\Delta x_{i,j} = x_{i,j+1} - x_{i,j}$ and $\Delta y_{i,j} = y_{i+1,j} - y_{i,j}$. Prior to the application of the tensile loading we assessed the deformations in the undeformed state, i.e., $\Delta X_{i,j} = X_{i,j+1} - X_{i,j}$ and $\Delta Y_{i,j} = Y_{i+1,j} - Y_{i,j}$. A schematic diagram of the central region of the lattice structure under consideration with the definitions of $\Delta x_{i,j}$, $\Delta y_{i,j}$, $\Delta X_{i,j}$ and $\Delta Y_{i,j}$ is shown in Figure 3.3 (b). The local homogenized values of the engineering strain for each unit cell were determined as:

$$\varepsilon_{xx,i,j} = \Delta x_{i,j} / \Delta X_{i,j} - 1 \text{ and } \varepsilon_{yy,i,j} = \Delta y_{i,j} / \Delta Y_{i,j} - 1, \tag{3.1}$$

The local values of the engineering strain were then used to calculate local values of the Poisson's ratio as:

$$v_{i,j} = -\frac{\varepsilon_{xx,i,j}}{\varepsilon_{yy,i,j}} \ , \tag{3.2}$$

Finally, the ensemble average Poisson's ratio of the nine central unit cells under consideration was computed as $v_{yx} = \langle v_{i,j} \rangle$.

3.2.3 Numerical modeling

The numerical simulations related to the mechanical response of the lattice materials are conducted using commercial FE package COMSOL Multiphysics. FE models with finite number of unit cells are investigated in this study. After trade-off studies between CPU costs and edge effects provided by the finite number of unit cells, we have used models with 4×5 unit cells in all the simulations (Figure 3.4 (a)). To provide a more uniform tensile displacement distribution we have intentionally added a rectangular beam-like section with 5 mm width on the top and bottom of the finite-size models. Plane strain condition is assumed during the simulations. The models are meshed with 6-node triangular elements and 6 elements are generated along the width of the beam after a test convergence.

During all of the simulations, the mechanical response of the constitutive material is modeled as nonlinear elastic. We did not specifically fit the experimentally measured data using hyperelastic models and did not discriminate between elastic and plastic behavior. Instead, the true stress-strain relation from the dogbone is directly exported to COMSOL Multiphysics and implemented as the constitutive equation for the core material. In addition, geometric nonlinearity is considered to represent the large deformation of the structure. During the simulations a uniaxial displacement loading is applied on the top of the beam, while the bottom is fixed along both the *x* and *y* directions (Figure 3.4 (a)).

The postprocessing of the results was focused on the unit cell in the central region only to avoid finite size and BCs effects (Figure 3.4). The Poisson's ratio can be calculated from the ratio of the nominal strain in the horizontal edge and vertical edge of the rectangular unit cell. Specifically, we first calculated the average displacement components of the four edges, from which the strain along horizontal and vertical directions can be calculated as:

$$\varepsilon_x = \frac{\bar{u}^R - \bar{u}^L}{2l} \text{ and } \varepsilon_y = \frac{\bar{v}^T - \bar{v}^B}{2l}, \tag{3.3}$$

In (3.3) $\bar{u}$ and $\bar{v}$ indicate the averaged horizontal and vertical displacement components respectively; *R*, *L*, *T*, and *B* denote the right, left, top, and bottom edges of the unit cell, (Figure 3.4 (b)). Finally, the Poisson's ratio is calculated as:

$$v_{yx} = -\frac{\varepsilon_x}{\varepsilon_y}.$$

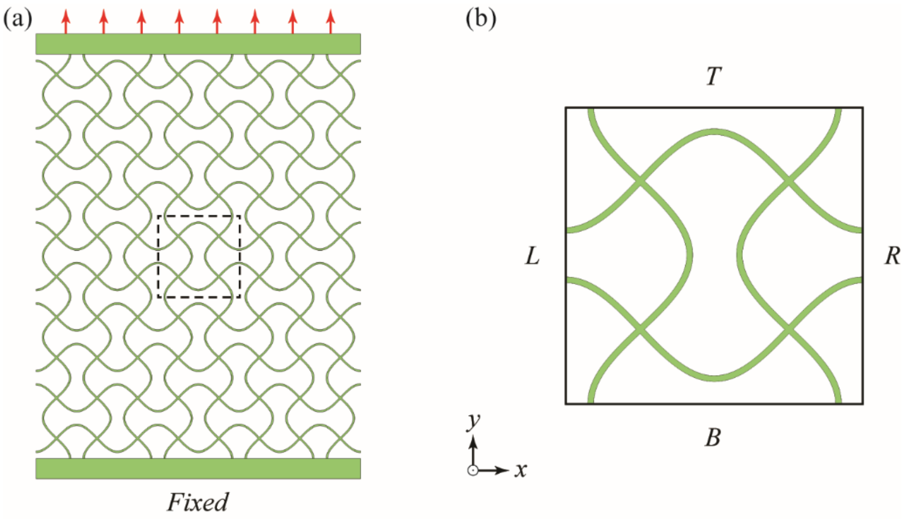

Figure 3.4 FE model for mechanical response simulation. (a) FE model with 4×5 unit cells and (b) Rectangular unit cell in the central area of FE model for the calculation of Poisson's ratio.

3.3 Auxetic behavior of 2D lattice metamaterials

Figure 3.5 (a) shows the nominal stress-strain relations for the three specimens under uniaxial tension. Good agreement can be observed between the numerical and experimental results. We found that these structures exhibit J-shaped stress-strain curves, which are very similar to the mechanical response of bioinspired soft network composite materials and other stretchable electronics.[56-59] The numerical and experimental estimates of the macroscopic Poisson's ratios as a function of the tensile strain are presented in Figure 3.5 (b). For tensile strains below 0.20 the numerical predictions tend to slightly overestimate the experimental results for n=1 and 2 because at small strains unavoidable misalignments in the test setup tends to influence the measurement of the Poisson's ratios. We also note that over this range of strain, the proposed square lattice materials exhibit a nearly constant negative Poisson's ratio. With the increase of the stretching, the Poisson's ratio gradually turns from negative to positive. To elucidate the mechanisms responsible for the transition of the Poisson's ratio we present the mechanical response of a representative unit cell taken from the central area of the specimen under different tensile strains (Figure 2 (c)). Here we only show the mechanical behavior of the lattice materials with n=1 and 3. Again, one can notice an excellent agreement between the numerical and the experimental deformations. At strains below ~0.20, the deformation response of the vertical beams is clearly bending-dominated due to the initial curvature of sinusoidal architecture. With the increase of macroscopic stretching, the sinusoidal architecture will be stretched to an approximate straight beam. As a result, the deformation behavior will become stretching-dominated and very similar to regular materials, which typically exhibit a positive or zero Poisson’s ratio.

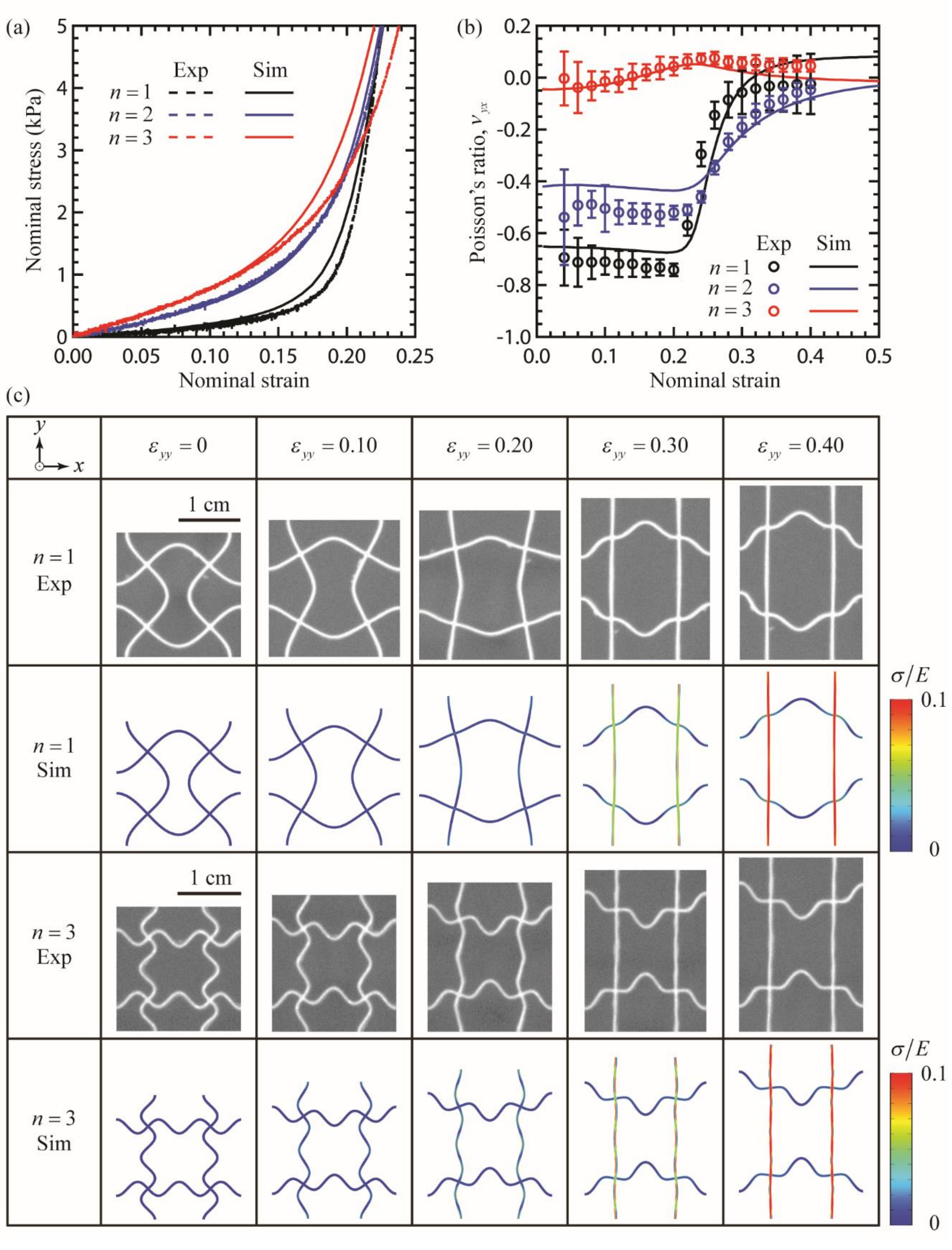

Figure 3.5 Mechanical response of lattice metamaterials under uniaxial stretching. (a) Stress-strain relations of the architected lattice metamaterials. (b) Evolution of the Poisson's ratios as a function

of the applied tensile strain. (c) Deformation behavior at different strains. The von Mises stresses are normalized with respect to the Young's modulus of the constitutive materials. Here $A_n n/l = 1/3$.

3.4 Mechanical tunable Poisson's ratios

Having demonstrated that the sinusoidally architected lattice materials exhibit auxetic behavior under uniaxial tension, we now systematically investigate the effects of amplitude $A_n n/l$ and half wavelength *n* on the mechanical response and the Poisson's ratios. Figure 3.6 (a) shows the stress-strain relations of the lattice materials with different $A_n n/l$ and *n*. Each structure exhibits a J-shaped stress-strain curve, which is similar to our previous experimental observation. For given amplitude a short wavelength (i.e., a large *n*) gives rise to a higher stress-strain curve, indicting the presence of a significantly stiffer mechanical response. For a given value of *n* a smaller wave amplitude (i.e., a smaller curvature but with a larger beam width) however leads to a higher stress-strain curve within the small strains range. These mechanical responses are intrinsically controlled by the bending stiffness of the sinusoidal beams, which is defined as $S = CE\kappa w^3$, where *C* is the geometric constant, *E* is the Young's modulus of the beam, κ is the curvature, and *w* is the width of the beam. The effective stiffness of the lattice materials as a function of $A_n n/l$ and *n* are summarized in Figure 3.7 (a). We further note that for a given wave amplitude a significant auxetic behavior can be observed for *n*=1, 2. Interestingly, the transition strain for the in-plane Poisson's ratio is proportional to the wave amplitude because large macroscopic stretching is needed to make straight vertical beams with larger wave amplitudes. The minimum Poisson's ratios as a function of $A_n n/l$ and *n* are summarized in Figure 3.7 (b).

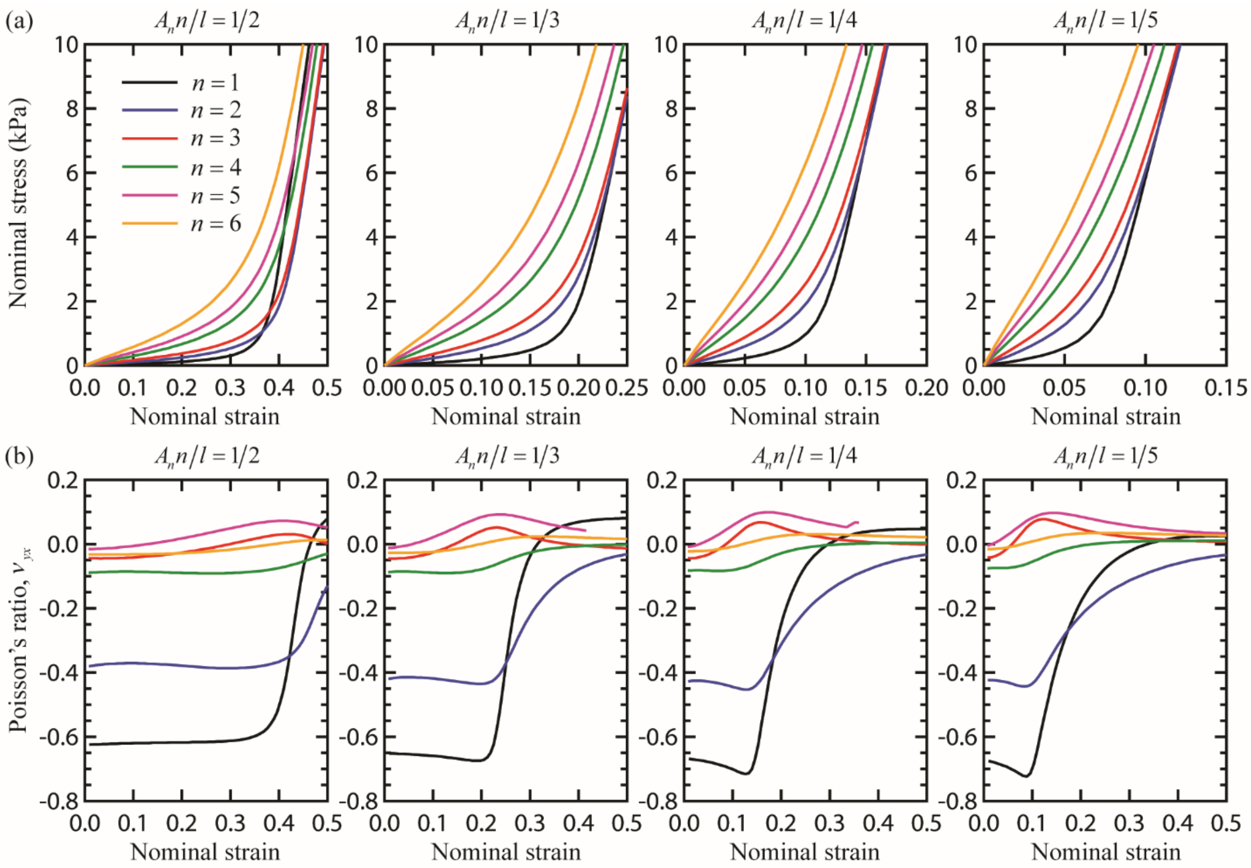

Figure 3.6 Effects of geometric features of the ligament on the mechanical response. Effect of (a) amplitude, $A_n n/l$ and (b) number of half wavelength, n, on the stress-strain relation and Poisson' ratio.

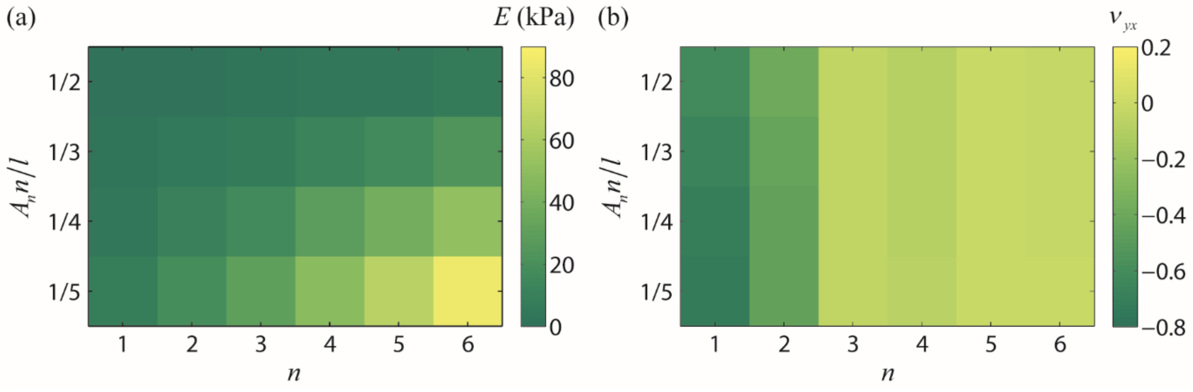

Figure 3.7 Effects of geometric features of the ligament on stiffness and Poisson's ratio. Effect of amplitude, $A_n n/l$ and number of half wavelength, *n*, on the (a) effective stiffness and (b) Poisson' ratio of the proposed lattice materials.

Another geometric parameter with a significant impact on the mechanical response and in-plane Poisson's ratios is slenderness ratio w/l . To demonstrate this, we examine the mechanical response and the auxetic behavior of the lattice material with $A_n n/l = 1/3$ and *n*=1, 2. Highly nonlinear stress-strain curves arise in those cases for a small strain range (Figure 3.8(a)) because the mechanical response of the sinusoidal beam is bending-dominated, with the bending stiffness being proportional to w^3 . Therefore, large slenderness ratio will give rise to higher stiffness. At large strains the mechanical response of sinusoidal beam becomes stretching-dominated and a nearly linear response can be observed in the stress-strain curves.

The bending-dominated and stretching-dominated behaviors at different strains have also a significant impact on the Poisson's ratios. At strains below 0.20 the lattice materials with *n*=1 and 2 have a nearly constant negative Poisson's ratio of ~ -0.65 and ~ -0.45, respectively. This phenomenon indicates that the Poisson's ratio is almost independent of the slenderness ratio when the sinusoidal beams are highly bending-dominated. By contrast, at large stretching strain, the Poisson's ratio rapidly changes from negative to positive for both cases. The transition is much sharper for a smaller slenderness ratio, since the nearly straight beam is in this case more compliant.

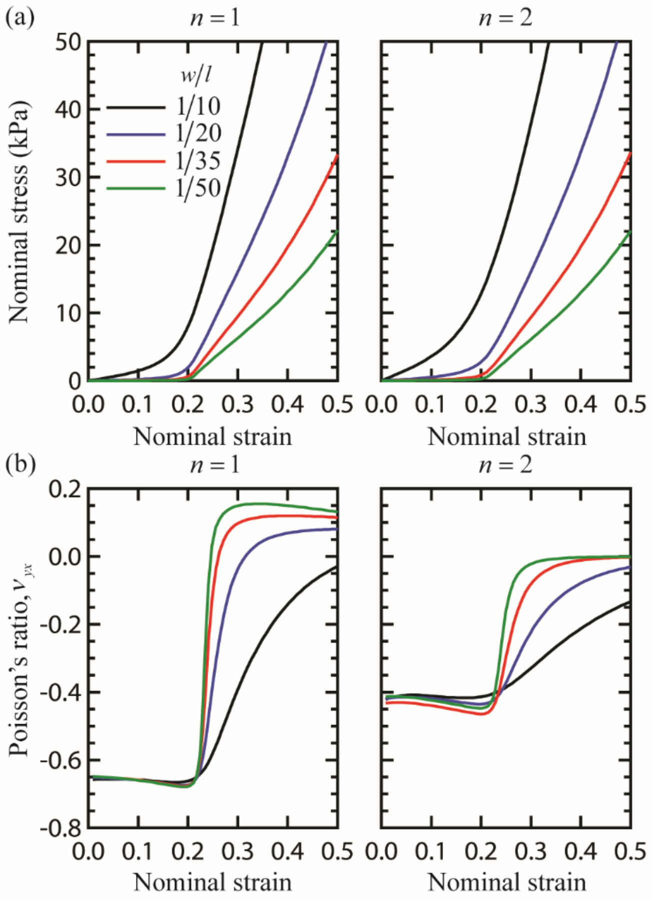

Figure 3.8 Effect of slenderness on the stress-strain relation and Poisson's ratios of the proposed lattice materials. Here $A_n n/l = 1/3$.

3.5 Effect of the lattice topology

Having shown that the mechanical response and the Poisson's ratios can be ~~dynamically~~ tuned by tailoring the geometric features of the sinusoidal beams, we now proceed to examine the effect of the lattice topology on the auxetic behavior from a numerical and experimental standpoint. Four types of sinusoidally architected lattice materials with hexagonal, kagome, square, and triangular topology are fabricated using 3D printing (Figure 3.9 (a)). Here we use as geometry parameters $A_n n/l = 1/3$ and *n*=2. Numerical simulations and mechanical testing are performed following the same procedure as outlined in Section 3.2. The specific lattice topology has a significant impact on the overall mechanical response of the lattice materials under tension (Figure 3.9 (c)). The triangular lattice has (as expected) the largest stiffness, while the hexagonal tessellation is the more compliant.[61] Experimental and numerical results related to the Poisson's ratios for the four types of topology are presented in Figure 3.9 (c), and they all show a good agreement In contrast to the negative Poisson's ratio of square lattice materials, both hexagonal and kagome lattice configurations exhibit a positive Poisson's ratio below 0.40 tensile strains. The evolution of the Poisson's ratio of the triangular lattice is however strongly strain dependent and there is a switch between NPR and PPR at a critical strain of 24%.

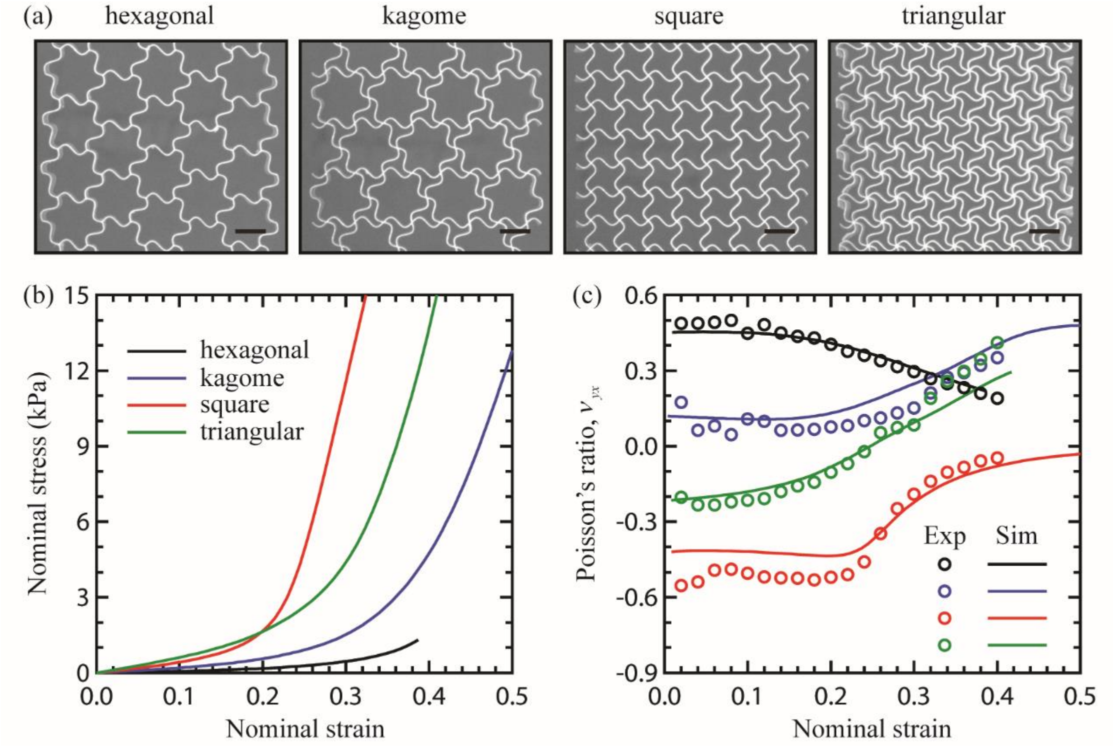

Figure 3.9 Effect of the topology on the stress-strain curves and Poisson's ratio. (a) 3D printed specimens with hexagonal, kagome, square, and triangular topology. (b) Stress-strain relations and (c) Evolution of Poisson's ratio as a function of the strain. The legend is the same as that in (b). Here $A_n n/l = 1/3$ and n=2. Scale bar: 1cm.

3.6 Conclusions

We have proposed a novel class of lattice metamaterials with sinusoidal architected beams and evaluated their mechanical response and wave propagation performances. Under uniaxial tension the proposed sinusoidal architecture in the lattice beams provides an intrinsic deformation mechanism to switch from bending-dominated to stretching-dominated behavior. This transition of deformation mechanisms allows obtaining tunable Poisson's ratios over a large tensile strain range. Our experimental and numerical results show a very good agreement in terms of overall stress-strain relations, Poisson's ratios, and deformation patterns exhibited by these lattices. The investigation into the interplay between the multiscale (ligament and cell) architecture and wave propagation shows that broad and multiple phononic band gaps can be achieved in these lattice materials. Quite importantly, this significant vibration mitigation capability can be dynamically tuned by an external mechanical stimulus, i.e., a uniaxial stretching. The deformation behavior of the proposed metamaterials, together with their vibration mitigation capability makes them particularly suitable for the design of programmable mechanical metamaterials. The findings presented here provide new insights into the development of architected metamaterials with unusual physical properties and a broad range of potential applications, such as tunable particle filters and adjustable acoustic metamaterials for vibration control.

Chapter 4. Harnessing out-of-plane deformation to design 3D architected lattice metamaterial with tunable Poisson's ratios

4.1 Introduction

Cellular structures are widely spread in natural systems, such as wood, human bone, and beaks of birds [14,61]. They hold great promising applications, including aerospace, LED technologies, and automotive, due to their great specific mechanical properties. Recent studies show that by tailoring the architecture of the cellular structures, improved mechanical properties such as light weight [62,63], high energy absorption [64-67], vibration control [68] and enhanced thermal performance [69-71] can be simultaneously achieved. Along with these unusual properties and functionalities, recent advances in additive manufacturing techniques, for example, 3D printing, have enabled to fabricate cellular structures with well-defined topologies, thereby leveraging the possibilities to explore unprecedented properties in architected cellular structures. Here we use architected materials to emphasize that the unusual properties pertaining to the cellular structures strongly depend on the rationally designed architecture, rather than their compositions.

Recently, extensive research efforts have been devoted to investigating the unusual physical properties in architected cellular structures. Among these properties, architected cellular structures with a negative Poisson's ratio (NPR) are of particular interest. These structures exhibit a counterintuitive mechanical response, as they will shrink (expand) laterally under uniaxial compression (stretch). Indeed, auxetic behavior has been reported in many 2D and 3D structures of natural systems, including cubic metals [38], zeolites [72,73], natural layered ceramics [41], silicon dioxides [42], single-layer graphene [43,44], and 2D protein crystals [74]. Lakes has first designed and fabricated the first 3D polymeric foam with isotropic auxetic behavior [75]. Subsequently, a number of geometries have been proposed to achieve negative Poisson's ratio.

Among various architectures, it is worth noting that 2D related structures are the majority, including honeycomb with inverted cells [76,77], planar chiral lattices [51,78,79], rigid rotating hexamers or squares [35,80-82], origami-kirigami based metamaterials [27,49,83-86] and hierarchical metamaterials with fractal cuts [50,87]. It should be pointed out that most of the auxetic effects in these 2D structures are due to the in-plane deformation, for example, the symmetric units with re-entrant angles [75,88-92] and asymmetric units [35,78,82,93-97] both rotate in the plane when deformed.

Most of the theoretical and experimental investigations related to auxetic cellular materials are focused on the microstructures with straight ligament topologies. Recently, it has been theoretically shown that the auxetic behavior can be attained in hierarchically architected lattice consisting of horseshoe microstructures [32]. A nonstraight rib configuration for open-cell polyurethane foams has also recently been considered as a likely explanation for the existence of an unusual blocked-shape memory effect in auxetic open-cell polyurethane foams [98]. Moreover, our previous study reports a class of architected lattice metamaterials with sinusoidally shaped ligaments in the plane, which are highly stretchable with tunable negative Poisson's ratios and vibration-mitigation capability [99]. Comparing with the comprehensive study of various 2D auxetic structures, fewer designs of synthetic 3D auxetic materials have been proposed. Among them, auxetic systems consisting of networks of buckliball [13], chiral-like structures [100], orthotropic laminated open-cell frameworks [101] have been fabricated via 3D printing and very recently, a metallic 3D auxetic cellular structure consisting of cubic chiral unit cells has been fabricated via selective electron beam melting [102]. In all of these systems, however, the auxetic behavior is exhibited only in the limit of small strains, and the design of 3D auxetic systems capable of obtaining these unusual properties at large strains still remains a challenge [12,103].

Recent studies indicate that it is possible to harness out-of-plane deformation to achieve auxetic behavior. For instance, origami-based metamaterials [27,83], the dimpled plastic sheets [47], and smooth curve sheet [104] all exhibit negative Poisson's ratio in a plane through out-of-plane deformation. Since these structures are all non-porous with heavy weight, the solid structures will suppress the large deformation amplitude. Here we report a architected lattice material system that exhibits tunable negative Poisson's ratio over a wide range of applied uniaxial stretch, which is intrinsically governed by the out-of-plane deformation in the curved ligaments. We will demonstrate our design concept through integrative numerical simulation, analytical modeling, 3D printing, and experimental tests.

4.2 Materials and methods

4.2.1 Description of geometric model

The structure presented here is a lattice metamaterial and consists of curved beam components made of the same material. Figure 4.1 shows an overview of the proposed structure, which is fabricated by an additive manufacturing technique (3D printing). A Cartesian coordinate system is used for the in-plane *x*-*y* and out-of-plane *x*-*z* coordinates. Figure 4.1 (a) shows the top view of a unit cell of the structure which is 2D regular square lattice consists of the beams with the width, *w* and the length, *L*. We create the lattice system by replacing the regular straight beams with curved beams in the out-of-plane direction. The shape of the curved beams can be mathematically described as $z = A\sin(\pi x / L)$, where *A* is the wave amplitude and *t* is the thickness of the beam. Figure 4.1 (c) illustrates the 3D lattice microstructure in 2 × 2 unit cells. The geometry of the structure is characterized by three dimensionless parameters: the normalized wave amplitude ratio, A / L, the normalized width of the beam, w / L and the normalized thickness of the beam, t / L. The proposed lattice metamaterials are fabricated using a multimaterial 3D printer (Objet

Connex260, Stratasys). To ensure the stretchability of the cellular configuration, a rubberlike material, FLX9795-DM, is used as the constitutive (core) material for the sinusoidally shaped beams. Figure 4.1 (d) shows a photograph of a real test specimen with 5 × 5 unit cells with $A/L = 0.2$, $w/L = t/L = 0.1$. The dimensions of the structural units without side bars are 100 × 100 × 40 mm. Both ends of the specimens, in the *x*-axial direction, are added a rectangular beam-like section with 5 mm width to provide a more uniform tensile displacement distribution.

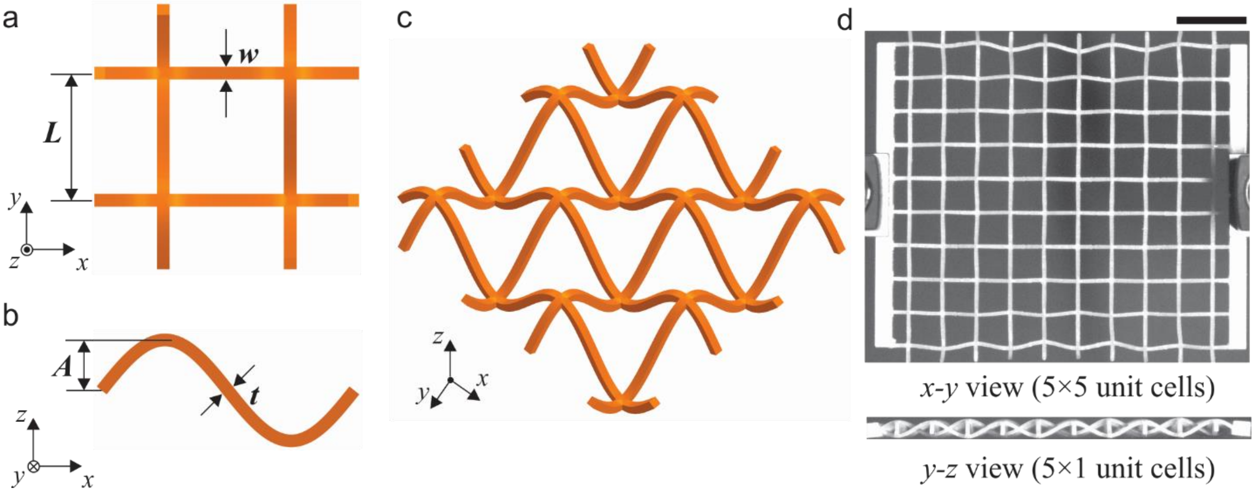

Figure 4.1 Overview of the proposed 3D planar auxetic metamaterials. (a) top and (b) side view of a unit cell, (c) schematic of the proposed construction, (d) photograph of a structure fabricated by 3D printing, comprising 5 × 5 × 1 unit cells in x, y, z coordinates. Scale bar: 2 cm.

4.2.2 Mechanical testing

The material properties of the FLX9795-DM rubber-like material were obtained by measuring the mechanical response of the 3D printed dogbone specimens. The experimental setup is shown in Figure 4.2 (a). For the dogbone specimen, speckles were sprayed on the samples using a spray paint for digital image correlation (DIC) measurements. The deformation and local strain contours of the samples were tracked by using DIC (Vic-2D, Correlated Solution) to calibrate the nominal stress-strain curves and to obtain the Poisson's ratio of the constitutive material. Figure 4.2 (b) shows the measured stress-strain curves (true and engineering strain) under uniaxial tension. According to ASTM 412, the basic properties of FLX9795-DM are characterized by a Young's modulus of $E = 5.5$ MPa, Poisson's ratio $\nu = 0.37$, and density $\rho = 1157$ kg/m^3. Here the Young's modulus is obtained from the measured stress-strain curve of dogbone specimen. Poisson's ratio of dogbone specimen is calculated by following the method in Section 4.2.2. The density is obtained by averaging the densities of five dogbone specimens.

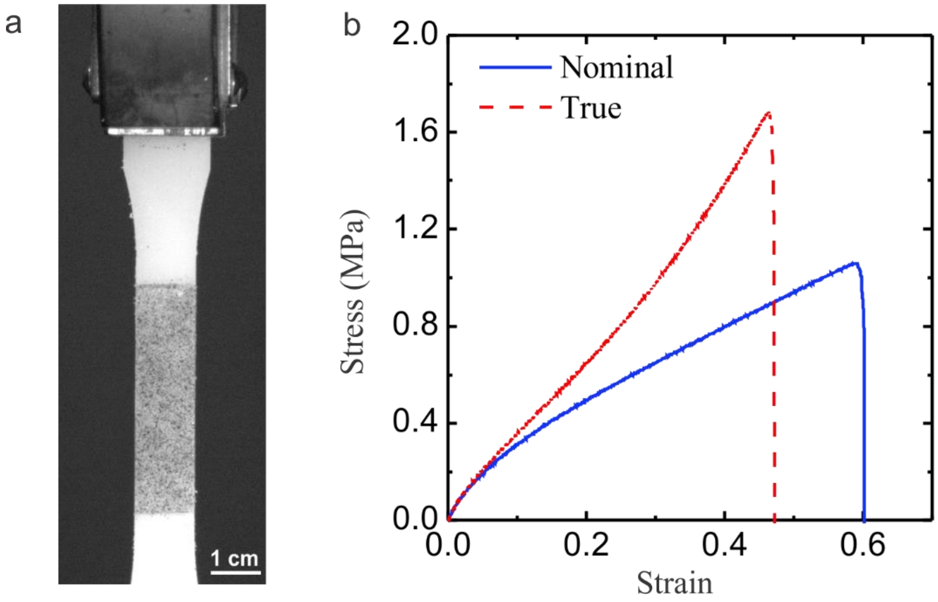

Figure 4.2 Material properties of constituent 3D printed materials. (a) 3D printed dogbone specimen under uniaxial tension. (b) Measured stress-strain relation of the dogbone specimen.

To quantify the deformation taking place in the lattice materials during the experiments an image processing software (ImageJ 1.49 q) was used to determine the intersection points in the specimen. The deformation near the four edges of the specimen was strongly affected by boundary conditions. Therefore, we focused on the central 30% of the specimens to avoid Saint Venant effects from the edges, as shown in Figure 4.3 (b). The intersection points at the corners of the chosen area were determined as $\left(X_{i,j}, Y_{i,j}\right)$ in the undeformed and $\left(x_{i,j}, y_{i,j}\right)$ in the deformed state, respectively. The row and the column indices vary between $1 \le i \le 4$ and $1 \le j \le 4$. For each unit cell, the horizontal and vertical distances were calculated from the coordinates $\left(x_{i,j}, y_{i,j}\right)$, i.e., $\Delta x_{i,j} = x_{i,j+1} - x_{i,j}$ and $\Delta y_{i,j} = y_{i+1,j} - y_{i,j}$. Prior to the application of the tensile loading, we assessed the deformations in the undeformed state, i.e., $\Delta X_{i,j} = X_{i,j+1} - X_{i,j}$ and $\Delta Y_{i,j} = Y_{i+1,j} - Y_{i,j}$. A schematic diagram of the central region of the lattice structure under consideration with the definitions of $\Delta x_{i,j}$, $\Delta y_{i,j}$, $\Delta X_{i,j}$ and $\Delta Y_{i,j}$ is shown in Figure 4.3 (b). The local homogenized values of the engineering strain for each unit cell were determined as:

$$\varepsilon_{xx,i,j} = \Delta x_{i,j} / \Delta X_{i,j} - 1 \text{ and } \varepsilon_{yy,i,j} = \Delta y_{i,j} / \Delta Y_{i,j} - 1. \tag{4.1}$$

The local values of the engineering strain were then used to calculate local values of the Poisson's ratio as:

$$v_{i,j} = -\frac{\varepsilon_{xx,i,j}}{\varepsilon_{yy,i,j}} \ . \tag{4.2}$$

In our case, the loading is nonlinear, the incremental Poisson's ratio, $v_{in,i,j}$, should be calculated as:

$$v_{in,i,j} = \frac{\Delta v_{i,j}}{\Delta \varepsilon_{yy,i,j}}. \tag{4.3}$$

Finally, the ensemble average Poisson's ratio of the nine central unit cells under consideration was computed as $v_{yx} = \left\langle v_{in,i,j} \right\rangle$.

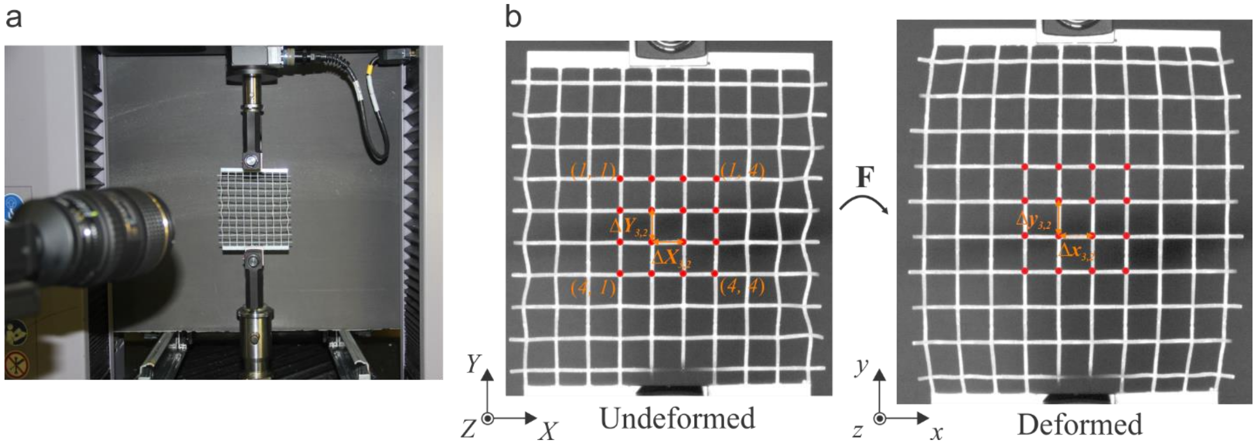

Figure 4.3 Experimental set-up for tension behavior of proposed 3D printed lattice material. (a) Experimental setup of the lattice specimen under uniaxial tension. (b) Calculation of Poisson's ratio.

4.2.3 Numerical modeling

The numerical simulations related to the mechanical response of the lattice metamaterials are conducted using commercial FE package ABAQUS/Standard (Simulia, Providence, RI). We have used models with 5 × 5 unit cells in all the simulations (Figure 4.4 (a) and (b)). All models are generated by beam elements (ABAQUS hybrid element type B22H) and meshed after a convergence test. In addition, geometric nonlinearity is considered to represent the large deformation of the structure.

Here, in our simulation, we use two types of boundary conditions. To simulate the experimental conditions in the numerical analysis, a uniaxial displacement loading is applied on the top surface, while the bottom is fixed along both the x and y directions (Figure 4.4 (a)). Under this boundary condition, the simulated results agree very well with the experimental results, as seen in Figure 4.5. To simulate the ideal conditions with avoiding Saint Venant effects from the edges, a uniaxial displacement loading is applied on the top surface, while the bottom surface is fixed along the y direction and the left surface is fixed along the x direction (Figure 4.4 (b)). Note that the periodic boundary conditions derived above are validated by comparison with analytical expressions and they agree very well, as shown in Figure 4. Therefore, for parametric analysis, the periodic boundary conditions are applied. Material model is critical to achieve better agreement between numerical simulation, experiment, and analytical model. Here we use a linear elastic model with a Young's modulus of $E = 5.5$ MPa, Poisson's ratio $\nu = 0.37$.

The postprocessing of the Poisson's ratio was focused on the unit cell in the central region to avoid finite size and boundary conditions effects (Figure 4.4 (c)). The Poisson's ratio can be calculated from the incremental ratio of the nominal strain in the horizontal edge and vertical edge of the rectangular unit cell. Specifically, we first calculated the average displacement component of the four edges, from which the strain along horizontal and vertical directions can be calculated as:

$$\varepsilon_x = \frac{\bar{u}^R - \bar{u}^L}{2l} \text{ and } \varepsilon_y = \frac{\bar{v}^T - \bar{v}^B}{2l}. \tag{4.4}$$

In equation (4.4) $\bar{u}$ and $\bar{v}$ indicate the average horizontal and vertical displacement components respectively; *R*, *L*, *T*, and *B* denote the right, left, top, and bottom edges of the unit cell, respectively (Figure 4.4 (c)). Finally, the incremental Poisson's ratio is calculated as:

$$\nu_{yx} = -\frac{\Delta\varepsilon_x}{\Delta\varepsilon_y}.$$

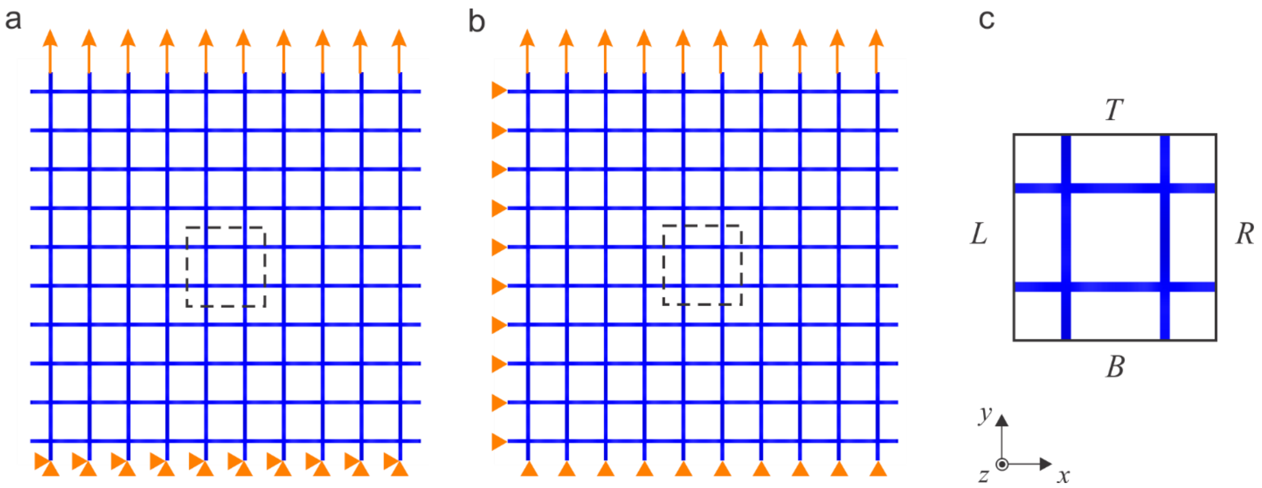

Figure 4.4 FE model for mechanical response simulation. (a) FE model with boundary conditions for comparison with the experimental test. (b) FE model with periodic boundary conditions.

4.3 Auxetic behavior of 3D planar lattice metamaterials

The uniaxial tension testing results of the experiment and numerical analysis are summarized in Figure 4.5. Figure 4.5 (a) shows the stress-strain curve under tensile deformation up to the failure point. It can be noted that a good agreement between the experimental and numerical results. When the applied strain is higher than 0.32, some beams start to break, leading to the drop in the stress-strain curves. These structures exhibit J-shaped stress-strain curves, which are very similar to the mechanical response of the lattice materials previously reported [99]. In Figure 4.5 (b) we present the relations between the horizontal strain and the vertical strain of the lattice material during uniaxial tension test. The experimental data points are shown in comparison with the numerically determined solid lines and it can be seen that there is close agreement between the sets of results. The horizontal strain first increases during the initial linear elastic response of the periodic structures before it reaches around 0.1, afterward, it becomes independent of the vertical strain. Apparently, this structure has an auxetic behavior. Since the response of the structure is non-linear as shown in the stress-strain plot in Figure 4.5 (a), the incremental Poisson's ratio ν is calculated using the relations of horizontal and vertical strain. The experimental and numerical estimates of

ν are plotted as a function of nominal strain in Figure 4.5 (c). At small strain (<0.02), the numerically determined estimate of the Poisson's ratio is approximately constant at $\nu_{num} = -0.875 \pm 0.052$. The experimental result is smaller than the numerical result with a value of $\nu_{\exp} = -0.950 \pm 0.110$. It is true that there is a minor discrepancy between simulation and experiment. We emphasize that the unavoidable misalignments in the test setup tend to influence the measurement of the Poisson's ratios since the lattice materials are very soft. It should be noted that when calculating the Poisson's ratio using DIC, we found that the mark points are also critical. It is ideal that each mark point should be at the intersection of the beams, but due to the small size of the node, it is hard to accurately place the mark point. With the increase of the stretching, the Poisson's ratio gradually turns from negative to marginally positive. Figure 4.5 (d) shows the specimen under deformation during the uniaxial tension test. It is clear that the lattice material expands transversally, indicating the presence of an auxetic behavior. The corresponding deformation images of numerical results are shown in Figure 4.5 (e). Again, similar lattice shapes between numerical and experiment deformations can be observed. Moreover, we find that the applied uniaxial stretch causes out-of-plane shrinking. (see side views in Figure 4.5 (d) and (e)). This is due to the mechanism of deformation of this lattice structure which will be discussed later.

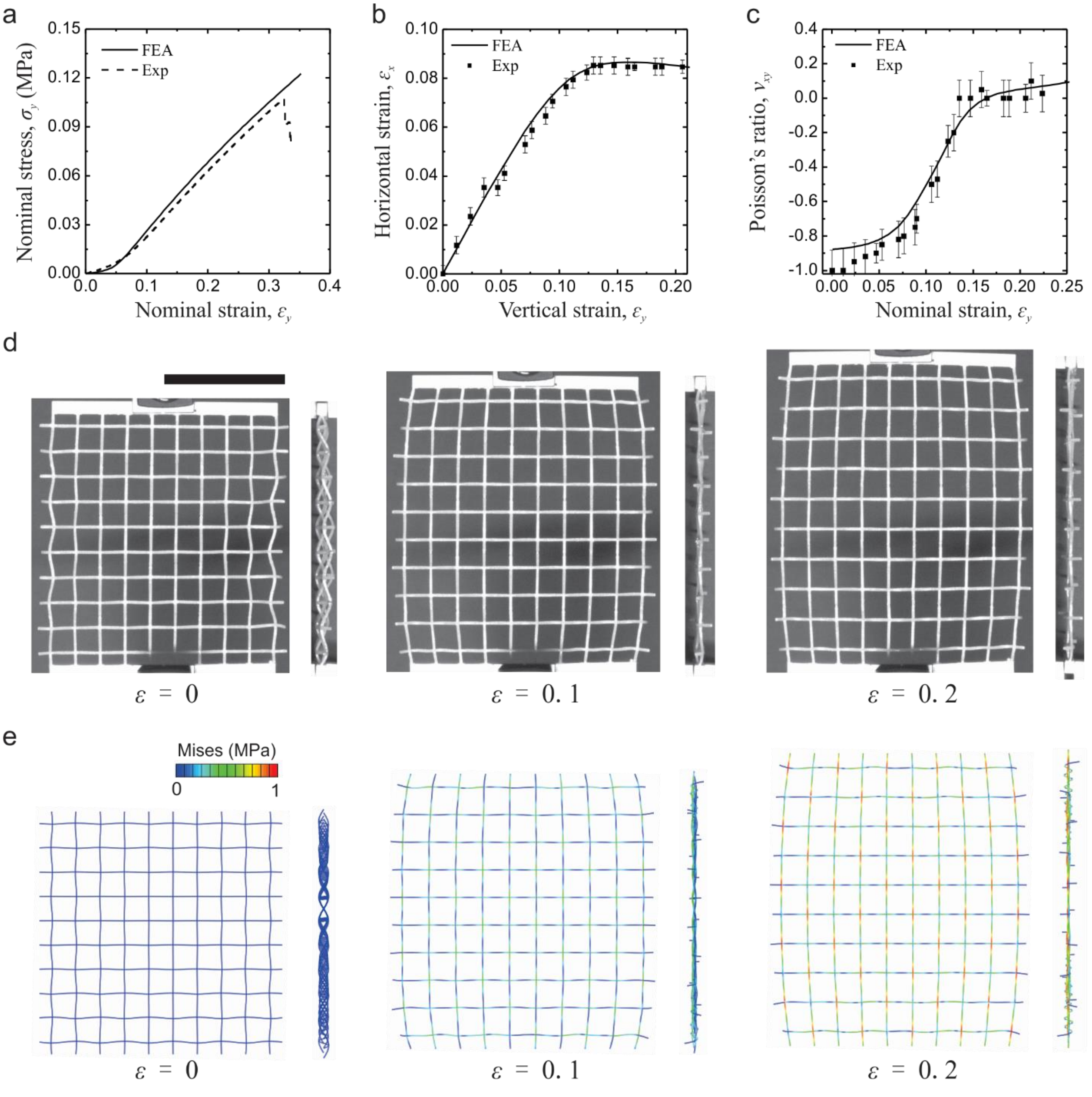

Figure 4.5 Experimental and FEA results of 3D planar auxetic metamaterials under uniaxial tensile tests. (a) Nominal stress vs. nominal strain curve; (b) measured horizontal strain vs. vertical strain; (c) calculated incremental Poisson's ratio curves as a function of nominal strain; (d) experimental and (e) simulation images at different levels of macroscopic strains: 0, 0.1, and 0.2. Scale bar: 5 cm.

4.4 Theoretical model of the 3D planar auxetic metamaterial

To quantitatively understand the mechanisms responsible for the auxetic behavior in the proposed lattice system, we formulate an analytic model for the lattice system under uniaxial tension. The lattice materials with 5 × 5 unit cells under horizontal stretching are taken as an example to illustrate the model, as shown in Figure 4.6 (a). Due to the lattice periodicity, only a representative unit cell (in the red frame of Figure 4.6 (a)) is analyzed, as shown in Figure 4.6 (b). The unit cell consists of four corner structures, while each connected structure undergoes anti-symmetric deformations with respect to the central point of the unit cell. Only one corner structure is selected for the force analysis as shown in Figure 4.6 (c). The inner axial forces, shear force, and the moment at the ends are denoted by N_i, Q_i and M_i, respectively. The static equilibrium of the unit cell gives the relations among the inner forces and the external loading (normal stress σ along horizontal direction):

$$N_2 = 0 \text{ and } N_1 = \sigma L t\,. \tag{4.5}$$

The deformation compatibility requires that the joints of deformed beams should satisfy the following geometric relations:

$$h_1 = h_2 \text{ and } Q_1 = Q_2 = Q \tag{4.6}$$

where h is the height of the curved beam in an out-of-plane direction.

Since the geometry is symmetric with regard to the central point, we consider a curved beam ($z = A\sin(\pi x / L)$, $0 \le x \le 0.5L$) subject to inner forces N_0, Q_0 and a moment, M_0 at one end on the *x*-*z* plane, as shown in Figure 4.6 (d). Based on the classic Elastic theory [32,105-107], if the effect of membrane deformation is neglected, we can introduce a model for small strain but finite rotation, which accounts for both bending and membrane deformation, to analyze the deformation and maximum strain in the microstructure. By solving this model numerically, we can obtain the coordinates of the right end for the curved beam (x_{end}, z_{end}) as:

$$x_{end} = f_1(N_0, Q_0) \text{ and } z_{end} = f_2(N_0, Q_0), \tag{4.7}$$

where $h = z_{end}$. Using Eqs. (4.6) and (4.7), Eq. (1) the becomes

$$f_2(\sigma Lt, Q) = f_2(0, Q) . \tag{4.8}$$

Therefore, for a given normal stress σ, the shear force Q can be solved directly. The deformation horizontal and vertical strain of this structure are:

$$\varepsilon_h = f_1(0, Q) / L \text{ and } \varepsilon_v = f_1(\sigma Lt, Q) / L .$$

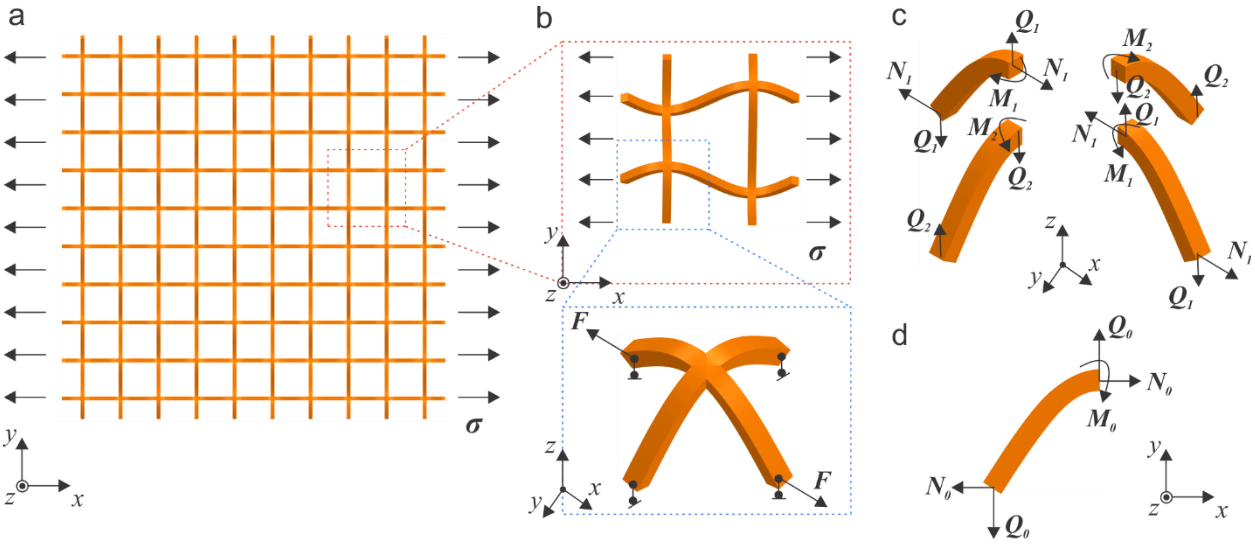

Figure 4.6 Schematics of the theoretical model of the 3D planar auxetic metamaterial subject to a uniform tensile stress along horizontal stretching. (a) The lattice materials with 5×5 unit cells under horizontal stretching is taken as an example to illustrate the model; (b) a representative unit cell is under

horizontal stretching and due to the anti-symmetric one corner structure is analyzed; (c) free body diagrams of the corner structure; (d) a curved beam subject to axial forces, shear forces and a moment at the right end.

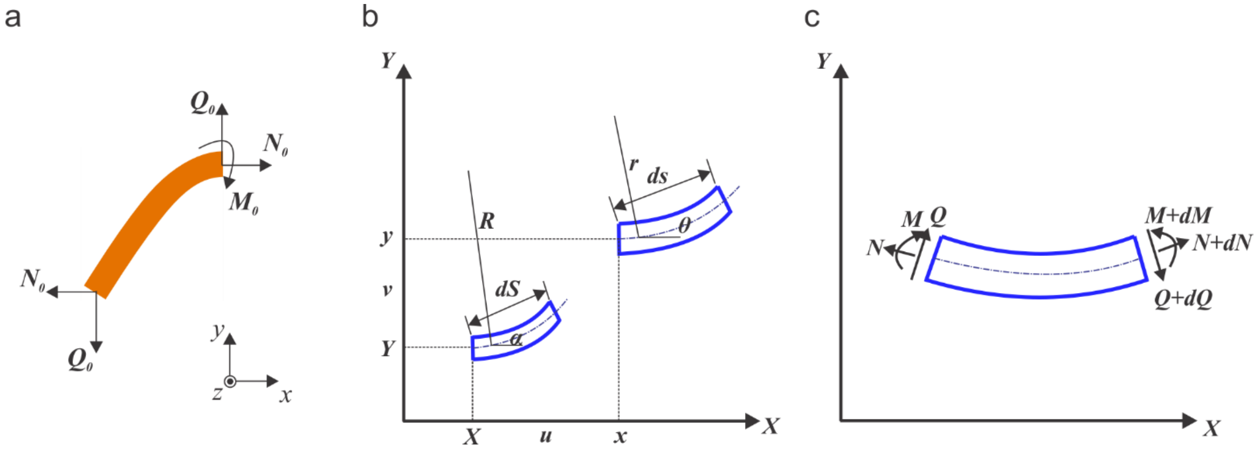

Figure 4.7 Schematics of the curved beam on a 2-D reference configuration. (a) A curved beam subject to axial forces, shear forces and a moment at the right end; (b) deformation of a unit length element; (c) sign conventions of forces and moment.

To describe the curved beam on a 2-D reference configuration, the undeformed length element dS after deformation becomes the deformed length element ds. The coordinate of the end point (X,Y) in the un-deformed state deforms to (x,y) shown as Figure 4.7 (b). At the un-deformed state, the tangent slope angle at (X,Y) is denoted by α. At the deformed state, the tangent slope at (x,y) is denoted by θ. The deformation at (X,Y) is denoted by (u,v) where u is the horizontal displacement, and v is the vertical displacement. Hence

$$x = X + u\,,\ \ y = Y + v\,. \tag{4.9}$$

The rotation angle φ can be found by

$$\varphi = \theta - \alpha\,. \tag{4.10}$$

Since the strain at the centroid axis is defined by $\varepsilon = (ds - dS)/dS$, or

$$ds = (1+\varepsilon)dS\,. \tag{4.11}$$

As in the case of in-extensional curved beam, $\varepsilon = 0$. For any length element dS, there is a corresponding radius of curvature R, such that

$$dS = Rd\alpha\,. \tag{4.12}$$

Here the radius of curvature R does not have to be a constant.

For the deformed length element ds, the corresponding radius of curvature is denoted by r, i.e.

$$ds = rd\theta\,. \tag{4.13}$$

For a linear elastic material with the Young's modulus E_S, integration of the above equation then gives the axial force N, shear force Q and bending moment M (per unit thickness, Figure 4.5 (d)) in the beam as

$$N = E_s A\varepsilon \text{ and } M = E_s I(1+\varepsilon)\frac{d\varphi}{ds}\,. \tag{4.14a, b}$$

The equilibrium equations are

$$\frac{dM}{ds} - Q = 0\,,\ \frac{dQ}{ds} - N\frac{d\theta}{ds} = 0\,, \text{ and } \frac{dN}{ds} + Q\frac{d\theta}{ds} = 0\,. \tag{4.15a, b, c}$$

For the loading condition shown in Figure 4.4 (a-b), the axial and shear forces are

$$N = N_0 \cos\theta + Q_0 \sin\theta \text{ and } Q = N_0 \sin\theta - Q_0 \cos\theta \,, \tag{4.16}$$

which satisfy Eqs. (4.15b) and (4.15c). Its substitution into Eq. (4.15a), together with Eq. (4.14), gives

$$\frac{d^2\varphi}{d^2S} = (1 + \frac{N_0 \cos\theta + Q_0 \sin\theta}{E_s A})(\frac{N_0 \sin\theta - Q_0 \cos\theta}{E_s I}) \,. \tag{4.17}$$

In our case, the shape of the sinusoidal beams can be mathematically described as $Z = A\sin(\pi X / L) = A\sin(BX)$, where A is the wave amplitude and $B = \pi / L$. The length of sinusoidal beam is given by

$$S = \int_0^{L/2} \sqrt{1 + (Z')^2}\, dX = \int_0^{L/2} \sqrt{1 + (AB\cos(BX))^2}\, dX \,, \tag{4.18}$$

which gives that

$$dS = \sqrt{1 + (AB\cos(BX))^2}\, dX \,. \tag{4.19}$$

And for the sinusoidal curve, the radius of curvature R is given by

$$\alpha = \arctan(Z') = \arctan(AB\cos(BX)) = f(X) \,. \tag{4.20}$$

From Eq. (4.14), the derivation $d\varphi / dS$ could be denoted as

$$\frac{d\varphi}{dS} = \frac{d\varphi}{dX}\frac{dX}{dS} = \frac{1}{\sqrt{1 + (AB\cos(BX))^2}}\frac{d\varphi}{dX} = n(X)\frac{d\varphi}{dX} \tag{4.21}$$

Similarly, the derivation $d^2\varphi / dS^2$ could be denoted as

$$\frac{d^2\varphi}{dS^2} = n^2(X)\frac{d^2\varphi}{dX^2} + n'(X)n(X)\frac{d\varphi}{dX} \,, \tag{4.22}$$

Substitute Eq. (4.20) to Eq. (4.10) and derivation gives the expression of $d\varphi/dX$ and $d^2\varphi/dX^2$ as

$$\frac{d\varphi}{dX}=\frac{d\theta}{dX}-\frac{d\alpha}{dX}=\frac{d\theta}{dX}-f'(X)\,, \tag{4.23a}$$

$$\frac{d^2\varphi}{dX^2}=\frac{d^2\theta}{dX^2}-f''(X)\,. \tag{4.23b}$$

Substitute Eq. (4.23a, b) into Eq. (4.22), it becomes

$$\frac{d^2\varphi}{dS^2}=n^2(X)\frac{d^2\theta}{dX^2}+n'(X)n(X)\frac{d\theta}{dX}+(-n'(X)n(X)f'(X)-n^2(X)f''(X))\,. \tag{4.24}$$

Then substitute Eq. (4.24) to Eq. (4.17) and simply gives

$$h(X)\frac{d^2\theta}{dX^2}+g(X)\frac{d\theta}{dX}+m(X)=H(\theta)\,, \tag{4.25a}$$

where $h(X)$, $g(X)$, $m(X)$ and $H(\theta)$ are defined as

$$h(X)=(1+(AB\cos(BX))^2)^{-1}, \tag{4.25b}$$

$$g(X)=A^2B^3\sin(BX)\cos(BX)(h(X))^2\,, \tag{4.25c}$$

$$m(X)=-AB^3\cos(BX)(-1-2A^2B^2+(AB)^2\cos(2BX))h^3(X))\,, \tag{4.25d}$$

$$H(\theta)=(1+\frac{N_0\cos\theta+Q_0\sin\theta}{E_sA})(\frac{N_0\sin\theta-Q_0\cos\theta}{E_sI})\,. \tag{4.25e}$$

For the deform mode as shown in Figure 4.4 (a), the vanishing bending moment at the left end can be written as $d\varphi/d\alpha=0$, which gives the first boundary condition as

$$\frac{d\theta}{dX}\Big|_{X=0} = 0 \tag{4.26}$$

And at the right end, the tangent slope angle keeps unchanged (because of the symmetric geometry), which can be evaluated as

$$\theta\Big|_{X=L/2} = 0 \tag{4.27}$$

And at the right end, the deformed coordinates are $x = x_{end}$ and $z = z_{end}$ (because of the anti-symmetric geometry), which can be evaluated by integrating $dx = \cos\theta ds$ and $dz = \sin\theta ds$ from the left end to the right end, i.e.,

$$x_{end} = \int_0^{l/2} \cos\theta(1 + \frac{N_0\cos\theta + Q_0\sin\theta}{E_S A})h^{-1/2}(X)dX \ , \tag{4.28a}$$

$$z_{end} = \int_0^{l/2} \sin\theta(1 + \frac{N_0\cos\theta + Q_0\sin\theta}{E_S A})h^{-1/2}(X)dX \ . \tag{4.28b}$$

By solving Eqs. (4.26) and (4.27), both the deformed angles and coordinates at the two ends, i.e., θ_{end}, x_{end} and z_{end}, can be. We numerically solve this problem in Matlab by using Runge-Kutta method and several search methods. In other words, the following constitutive relation can be obtained:

$$x_{end} = f_1(N_0, Q_0) \text{ and } z_{end} = f_2(N_0, Q_0) . \tag{4.29}$$

In order to compare theoretical and simulated results, the mechanical response of the lattice materials under uniaxial stretching along vertical directions is presented in Figure 4.8. All theoretical results agree reasonably well with the FEA calculations. Here we use two specimens consist of a representative unit cell with $w/L = t/L = 0.1$ and $A/L = 0.2$ or 0.6, respectively. It is clearly that the specimen with $A/L=0.2$ have a higher stress-strain curve within the small strains range compared with the specimen with $A/L=0.6$, as shown in Figure 4.8 (a). The nominal stress-strain curve increases slowly at a low strain in a bending-dominated deformation mode, and increases rapidly after a critical strain, ε_{cr} due to a transition into stretching-dominated deformation mode. This critical strain is well presented by

$$\varepsilon_{cr}=(\int_0^L\sqrt{1+\left(\frac{A\pi}{L}\cos\left(\frac{\pi x}{L}\right)\right)^2}dx)/L-1, \tag{4.30}$$

denoting the strain to fully extend the curved beam with sin wave, as marked by the dashed line in Figure 4.8 (a)-(c). Fig. 4 (b) shows that the relation of horizontal strain and vertical strain increases linearly at a low strain, but after a vertical critical strain, it approaches to a plateau which is the horizontal critical strain. It can be noticed that the vertical critical strain and horizontal critical strain are equal, which can be estimated as Eqn. 5. The calculated incremental Poisson's ratios show negative values as -0.856 and -0.925 for the specimen with $A/L=0.2$ and 0.6 respectively in Figure 4.8 (c). With the deformation mechanisms switching from bending to stretching at the critical strain, the Poisson's ratio increases dramatically from negative to almost zero. The deformed configurations of the representative unit cell based on the theoretical prediction show very good accordance with the FEA results under different strain levels as shown in Figure 4.8 (d). It can be noted that the negative Poisson effect originates mainly from the dilatation of the lattice-shaped unit cell. Here, the beams deform from curved to straight in both directions which indicate a full expansion along the horizontal direction during vertical stretching. Therefore, our analytical model explains the reason for the auxetic behavior of this lattice structure and demonstrates a clear transition of deformation mode from bending-dominated to stretching-dominated behaviors in the uniaxial stretching.

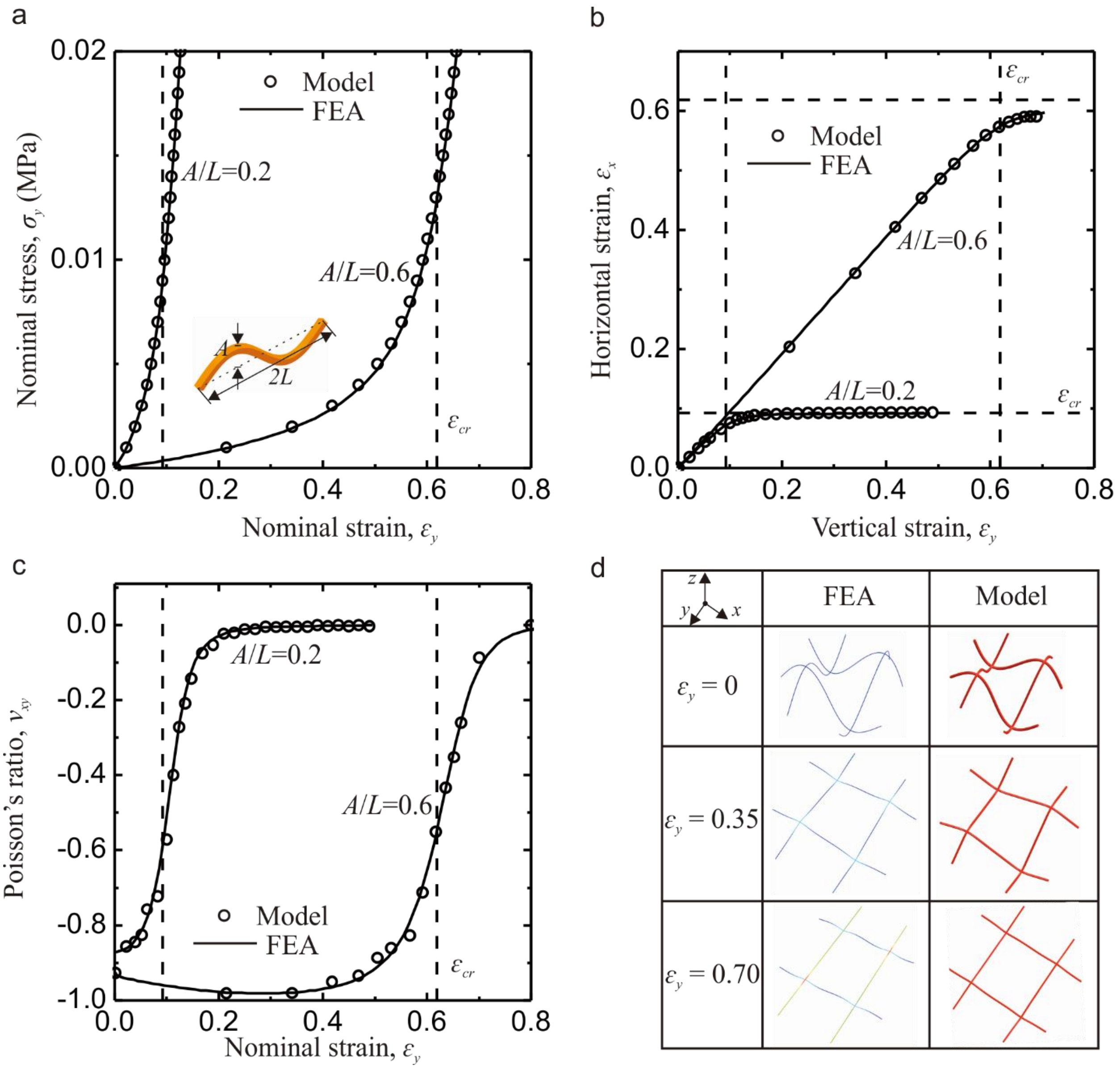

Figure 4.8 Theoretical and FEA results of 3D planar auxetic metamaterials under uniaxial tensile tests. (a) Nominal stress vs. nominal strain curve; (b) measured horizontal strain vs. vertical strain; (c) calculated incremental Poisson's ratio curves as a function of nominal strain; (d) Theoretical and (e) simulation images for the specimen with $A/L = 0.6$ at different levels of macroscopic strain:

0, 0.35, and 0.7. Here the dash lines present the critical strain which is the strain to fully extend the curved beam with sin wave.

4.5 Effect of the geometric parameters

Having demonstrated that the lattice metamaterials exhibit auxetic behavior under uniaxial tension at specific strain ranges, we now systematically investigate the effects of geometry parameters on the evolution of Poisson's ratios, ν . Because the Poisson's ratio is highly strain-dependent, we select the values at very small strains (≤ 0.02) for each specimen. In Figure 4.9 (a), we report the evolution of ν as a function of A/L for different values of w/L (0.01-0.20), while t/L is kept constant of 0.1. First, the results indicate that, as A/L increases, ν initially drops, reaches a minimum value and then increases. Moreover, we find that the macroscopic Poisson's ratio slightly decreases as the normalized width of the beam increases. In Figure 4.9 (b), we present the evolution of ν as a function of A/L for different values of t/L (0.01-0.30), while w/L is kept constant of 0.1. Similarly, as A/L increases, ν initially drop except the specimen with t/L =0.01, reaches a minimum value and then keep almost constant. Furthermore, the macroscopic Poisson's ratio increases as the normalized thickness of the beam increases. These mechanical responses are intrinsically controlled by the bending stiffness of the beams, $E_S I = 1/12wt^3$, where E_S is the Young's modulus of the material and I is the moment of inertia. In Figure 4.9 (c), we report the evolution of ν as a function of nominal strain for different values of A/L (0.1-0.8), while t/L and w/L are both kept constant of 0.1. Interestingly, the transition strain for the Poisson's ratio from negative to zero is proportional to the wave amplitude ratio. This is because large macroscopic stretching is needed to make the vertical beams with larger wave amplitude ratio straight. Moreover, the wave amplitude direction in our lattice materials is out-of-plane, which indicates that we can design lattice structures to achieve tunable Poisson's ratio at extreme large stretching strains. Furthermore, we find that the responses of the system are affected by the wavelength number, *n*. In the previous lattice materials, the curved beam can be described as: $z = A\sin(n\pi x / L)$ with $n = 1$. It is noted that the auxetic behavior cannot be observed for $n = 2$ and 3, as seen in Figure 4.9 (d). Finally, these results suggest ability reliable and versatile route to tailor the geometric features of lattice material with curved beams to achieve tunable mechanical properties especially negative Poisson's ratio for specific mechanical applications.

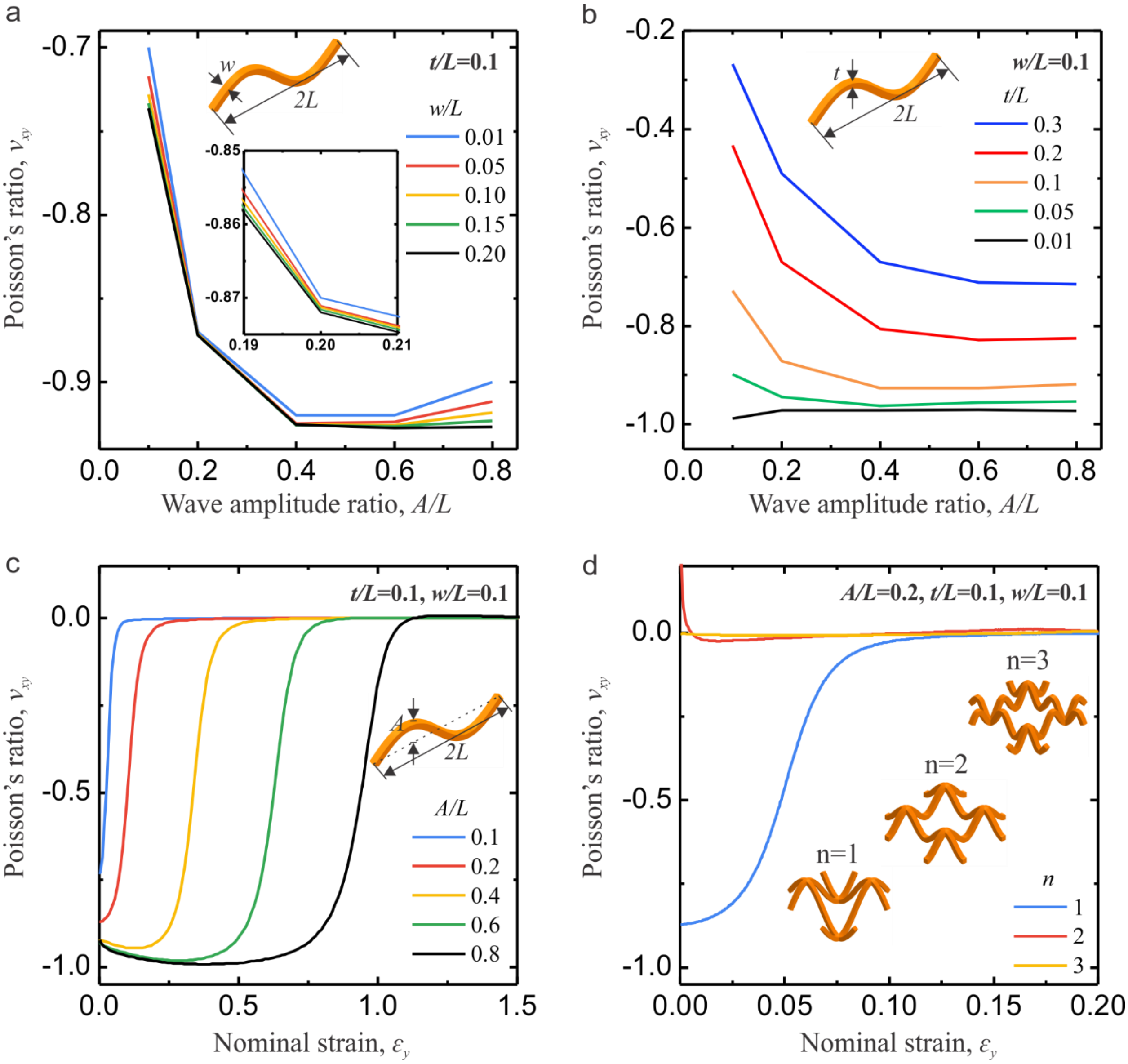

Figure 4.9 Effect of *A/L*, *w/L*, *t/L*, and n on the macroscopic Poisson's ratio of the 3D planar metamaterials, v_{yx}. Evolution of v_{yx} as a function of *A/L*. It is shown in (a) for five different values of *w/L* (assuming *t/L* = 0.1), in (b) for five different values of *t/L* (assuming *w/L* = 0.1). Evolution of v_{yx} as a function of nominal strain is shown in (c) for five different values of *A/L* (assuming *t/L* = 0.1 and *w/L* = 0.1), and in (d) for three different values of *n* (assuming *A/L* = 0.2, *t/L* = 0.1 and *w/L* = 0.1).

4.6 Design concept extension from 1D to 3D lattice metamaterials

Compared with conventional 2D lattice auxetics, the proposed 3D architected lattice system exhibits an auxetic behavior over a large range of applied strain. Theoretically, there is no limitation for the applied stretch strain, since there is enough space to incorporate the curved ligaments in the out-of-plane direction. Moreover, the proposed architected lattice system is highly structural efficient in terms of its lightweight design, as compared with dimpled plastic sheets [47] and origami based auxetics [27,83].

Indeed, the design concept of replacing the straight beam with a curved beam could be applied to form 1D, 2D, or 3D metamaterials (Figure 4.10). Figure 4.10 (a) present the 1D corrugated laminates exhibiting the geometrically non-linear stiffness response which is crucial for applications with large deformation [108]. Figure 4.10 (b) shows the 2D lattice metamaterials. Our previous report [99] indicates that this systematic lattice metamaterial exhibit extreme Poisson's ratio variations between -0.7 and 0.5 under large tensile deformations and remarkable broadband vibration-mitigation capability of the lattice metamaterials. Figure 4.10 (c) presents the 3D planar metamaterials which have been studied in this paper. Comparing with 2D lattice metamaterials, our 3D planar metamaterials could perform larger tensile deformation because of the structure extension in the 3rd dimension. Moreover, we can use the structures of 3D planar metamaterials as a template to design a 3D lattice metamaterials, as shown in Figure 4.10 (d). This 3D cubic lattice structure consists of 2D chiral-like structures in the lateral surface and 3D planar metamaterials structures in the middle. Therefore, they exhibit tunable negative Poisson's ratio not only under uniaxial compression but also uniaxial tension in *x*, *y* and *z* directions, as shown in Figure 4.10 (e). Furthermore, this material design strategy could be extended to 3D periodic lattice metamaterials, thus opening up the possibility of designing and analyzing novel materials with auxetic behavior.

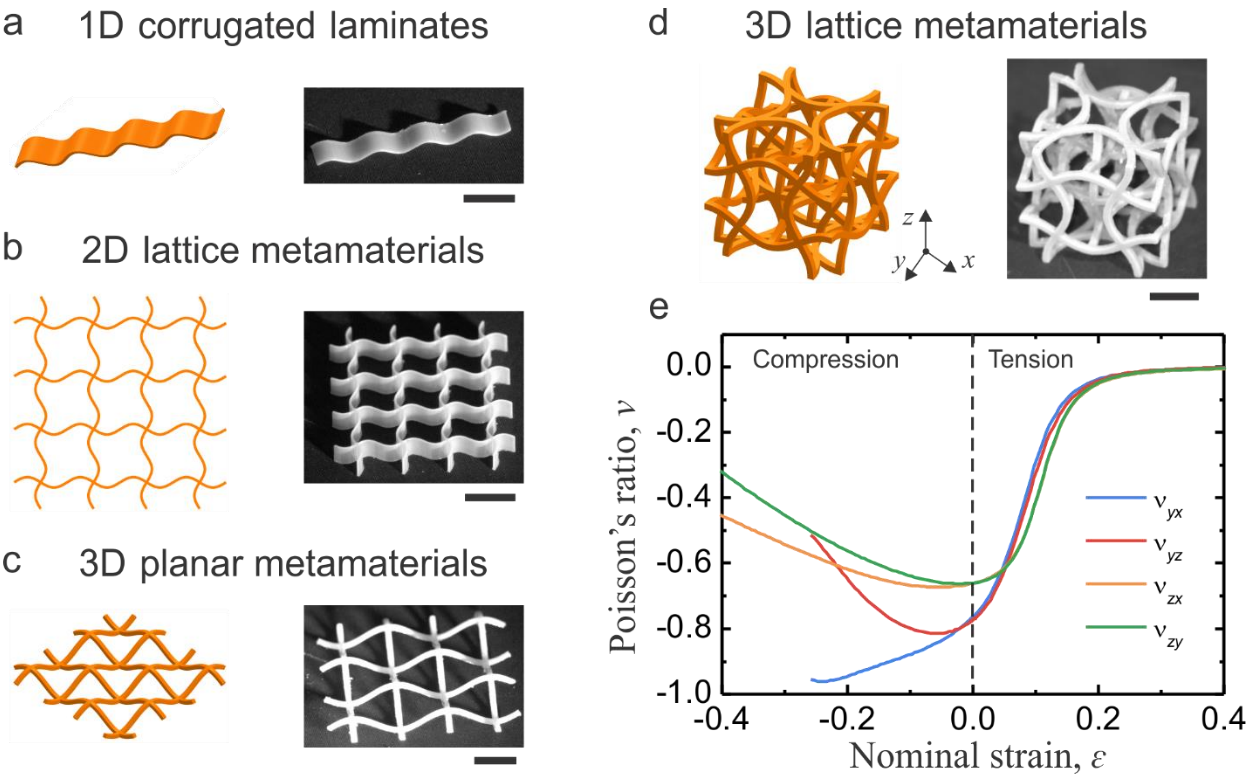

Figure 4.10 The system of lattice metamaterials with curved beams. (a) 1D corrugated beam; (b) 2D lattice metamaterial; (c) 3D planar metamaterial; (d) 3D lattice metamaterial. (e) The Poisson's ratio as a function of nominal strain for the 3D lattice metamaterials under uniaxial compression and tension by FEM analysis. Because of the symmetry of the structures in *x* and *y* directions, we only show the results of loading in *y* and *z* directions. Scale bar: 1 cm.

4.7 Conclusion

In summary, we have demonstrated a fundamental new approach to generate 3D planar metamaterials with negative Poisson's ratio by replacing the straight beams with curved beams in the out-of-plane direction. Through a combination of numerical analysis and experiments, we have shown that the Poisson's ratio of the system can be tuned and altered by designing the geometry of the curved beam structures. In particular, we present a theoretical study of nonlinear mechanical behavior in a class of lattice metamaterial with curved beams (sinusoidal shapes). This model can predict precisely the nonlinear stress-strain curve and Poisson ratio, as well as the deformed configurations under uniaxial stretching. Importantly, this material design strategy can be applied from 1D, 2D to 3D metamaterials, providing insights into the development of classes of architected metamaterials with potential applications including energy absorption, tunable acoustics, vibration control, responsive devices, soft robotics, and stretchable electronics.

Chapter 5. The design of sandwich composites with cellular cores

5.1 Introduction

Sandwich composite structures are widely used in aerospace, naval, sporting and automotive applications due to their high stiffness/weight ratio, high strength/weight ratio, and energy absorption capacity [109]. Typical sandwich structures consist of two thin, stiff and strong face sheets separated by a lightweight core that is usually made of polymeric foam, honeycomb or corrugated core etc. The core material keeps the face sheets in their relative positions in the sandwich with little increase in weight, to increase bending and buckling resistance [61,110], as well as shear stiffness and energy absorption ability [111]. The mechanical behavior of a sandwich composite depends on the material used for construction, geometry of face sheets and especially the core topology design. Among all sandwich core materials, foams core has been firstly studied [112] while they exhibit poor scaling due to their bending-dominated architecture [113]. Compared with the random porous structures of foams, various ordered cellular architectures with improved mechanical properties are applied to sandwich core configurations. The most widely studied and used one is conventional honeycomb cellular core [114-117]. Many analytical, numerical, and experimental investigations have suggested that sandwich structures with conventional honeycomb cellular core are stiff, strong, light and absorb much energy when crushed especially in out-of-plane direction [61,118-121]. Another attractive sandwich core is lattice truss materials [122-124]. Recent researchers have proposed that the textile truss cores are superior to regular honeycomb because of their superior buckling resistance at low relative density [125-129], and these open-celled counterparts would not trap moisture and possess multifunctional capabilities [122].

More recently, auxetic structures have received considerable attention because they exhibit unusual properties of becoming thicker when stretched; that is, they have negative Poisson's ratios. Due to the auxetic effects, auxetic cellular materials have many engineering advantages, such as increased indentation resistance [130], shear resistance [131], plane strain fracture toughness [34,132,133], and energy absorption [134-137]. Furthermore, auxetic structures exhibit synclastic bending [33,138-141], and have better acoustic properties compared to their conventional counterparts [142]. Based on the classical continuum theory, the auxeticity of materials can enhance certain mechanical properties, such as less deflection during bending [134] and increased shear modulus [131], making the structures ideal for use as sandwich core topology. Among various auxetic materials and structures discovered, re-entrant honeycomb has been investigated frequently by many researchers. The analytical studies on the re-entrant honeycomb have been reported on their mechanical properties under small deformation [61,143-147] and large deformation [148,149]. Moreover, it has been theoretically shown that the re-entrant honeycomb has enhanced shear properties compared to conventional materials [150,151]. Hou *et al.* [49,152] have studied the bending and failure of sandwich structures with auxetic gradient honeycomb cores. Imbalzano *et al*. [153,154] have numerically studied the performance of impact resistance for the sandwich panels with auxetic lattice cores. Yang *et al.* [155] have designed a sandwich structure with a 3D re-entrant auxetic core fabricated using electron beam melting and selective laser sintering and bending behavior on these materials has been studied. However, systematical studies on bending behavior of sandwich structures with auxetic core topology in comparison with non-auxetic core topology have not been largely explored. Conventionally, auxetic structures have been fabricated through multiple steps where the control of the specific geometry is quite difficult. Recently 3D printing, also known as additive manufacturing, has been developed rapidly, which enables the fabrication of auxetic cellular materials with precise and complex cellular geometries directly from the CAD models [156].

5.2 Design and fabrication of sandwich composites

5.2.1 Structural design

The geometric features of the proposed sandwich core design of truss, conventional honeycomb, and re-entrant honeycomb are discussed here. Figure 5.1 illustrates the schematic of three lattice microstructures. The relative density for each configuration can be calculated as

For truss
$$\frac{\rho^*}{\rho_S} = \frac{t}{L\sin\theta\cos\theta} \ , \tag{5.1}$$

For conventional and re-entrant honeycombs

$$\frac{\rho^*}{\rho_S} = \frac{t/L(H/L+2)}{2\cos\theta(H/L+\sin\theta)} \ . \tag{5.2}$$

Here the relative densities as 0.2, 0.3 and 0.4 are considered. Therefore, the thickness of cell walls can be calculated from the Equations (5.1) and (5.2), respectively. Three types of cellular structures are fixed to have the same dimension of the unit cell, as 9 mm × 9 mm. Details of the parameters for each design are listed in Table 5.1. Under small deformation, the in-plane Poisson's ratio can be evaluated [61] as

For truss
$$v_{12} = \cot\theta \, , \tag{5.3}$$

For conventional and re-entrant honeycombs

$$v_{12} = \frac{\cos^2\theta}{(H/L+\sin\theta)\sin\theta} \, . \tag{5.4}$$

For re-entrant honeycomb, θ is negative, then the Poisson's ratio of the cell becomes negative in values. Therefore, according the Equations (5.3) and (5.4), the Poisson's ratio of truss, conventional honeycomb, and re-entrant honeycomb in current design are evaluated as 1, 1.732 and -1.732, respectively. Here, the re-entrant honeycombs are orthotropic and they also have a Poisson's ratio, ν_{21}. However, we specifically focus on the Poisson's ratios, ν_{12}, in this work due to the compressive deformation induced by bending of the sandwich composites and the tensile deformation all in the direction 1.

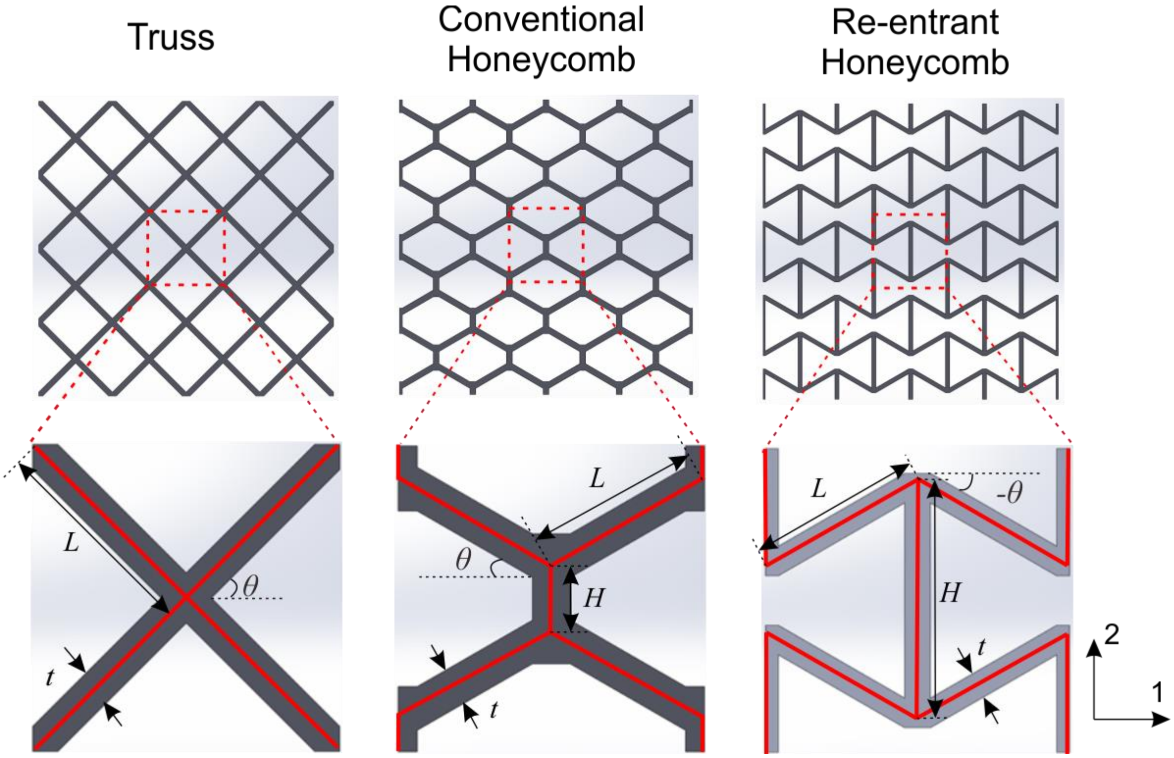

Figure 5.1 Design of unit cell of the truss, conventional honeycomb, and re-entrant honeycomb structure. Here, L is the length of the inclined cell walls of truss structures; t is the thickness of the cell walls; and θ is the angle between the inclined cell walls. The shapes of regular and re-entrant honeycomb structures are described as the length of the vertical cell walls, H; the length of the

inclined cell walls, L; the thickness of the cell walls, t, and the angle between the vertical and inclined cell walls, θ.

Table 5.1 Design parameters of truss, conventional honeycomb, and re-entrant honeycomb (Unit: mm).

	Truss			Conventional Honeycomb				Re-entrant Honeycomb			
ρ_C^* / ρ_S	L	t	θ	L	H	t	θ	L	H	t	θ
0.2	6.37	0.67	45°	5.2	1.9	0.71	30°	5.2	7.1	0.50	-30°
0.3	6.37	1.04	45°	5.2	1.9	1.11	30°	5.2	7.1	0.76	-30°
0.4	6.37	1.44	45°	5.2	1.9	1.56	30°	5.2	7.1	1.04	-30°

The sandwich beams are designed to have overall dimensions of 108 mm × 21 mm × 10 mm and be composed by 12 × 2 unit cells. Two thin layers are also added to the top and bottom of the core structures to improve the connection alignment with the sandwich face sheets. Figure 5.2 (a) shows a sandwich beam for bend test. The geometric parameters are listed in Table 5.2.

Table 5.2 Design geometric parameters of sandwich composite structures for bending test (Unit: mm).

Core			Sandwich panel					
VeroWhite			VeroWhite		W-CFRP		U-CFRP	
a	b	c	t_f	d	t_f	d	t_f	d
108	10	19	1	20	2.3	21.3	1.5	20.5

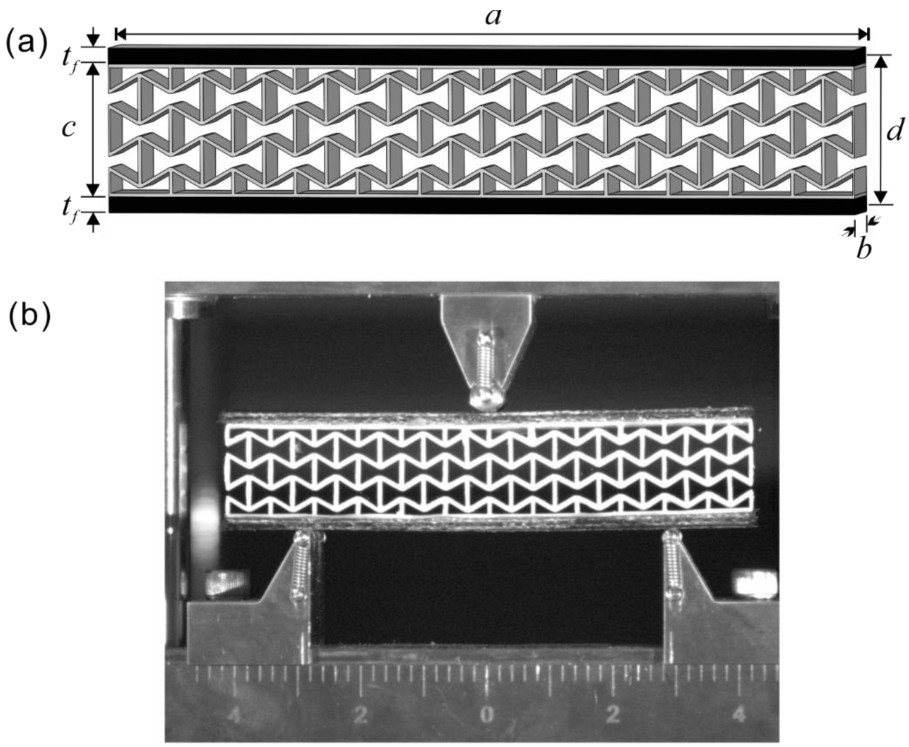

Figure 5.2 Three-point bending test set-up and the sandwich samples. (a) Sandwich structures for bending test. The subscript ‘ f ’ refers to the face sheets. Here, a is the length of the beam; b is the width; c is the core thickness; t_f is the face sheet thickness; d is the distance between centroids of faces. (b) Set-up of the three-point bending test.

5.2.2 Sample preparation

The proposed sandwich core materials are fabricated using a 3D printer (Objet Connex260, Stratasys) and VeroWhite (VW, an acrylic-based photopolymer) is taken as the constitutive material for the core structures. Considering the anisotropic nature of 3D printing technology due to layer-by-layer fabrication process, the layer orientation is found to influence the mechanical properties of the material; therefore, all the specimens are printed along the same orientation. The as-fabricated specimens are kept at room temperature for 7 days to allow for the saturation of the curing.

Three types of sandwich specimens with VeroWhite, woven carbon fiber reinforced polymer and unidirectional carbon fiber reinforced polymer as the face sheets are made respectively. U-CFRP is directly ordered from Graphtek LLC. W-CFRP is fabricated in our lab, which is a 16 layers of carbon fiber ordered in $(0°/90°)4^{sym}$, reinforced in Vinylester matrix. The fabrication process includes the cold-bonded of CFRP in vacuum. The material properties of VW, W-CFRP and U-CFRP are obtained by uniaxial tensile testing of each material following the ASTM D638 standard, as shown in Table 5.3. After all the core material and face sheets are completely manufactured, two face sheets are adhered to one core structure together by epoxy adhesive (E-00NS). All specimens are kept by attachment for one day to make sure they are bonded adhesively then dried for 7 days to allow coherent between the core and skins. After that, the surfaces of the sandwich skins are cleaned to avoid the effect of remaining glue on the bending test.

Table 5.3 Material properties.

	VeroWhite	W-CFRP	U-CFRP
Young’s modulus (GPa)	1.6	26	94 (longitudinal)
Yield Strength (MPa)	66	390	1400 (longitudinal)

5.2.3 Mechanical testing

The compression test and three-point bending test are performed using a MTS mechanical tester (C43 frame) with a 10 kN load cell. The quasi-static compression is carried out at a constant strain rate of 0.005 s^{-1}. Three-point bending test is carried out at a loading rate of 0.008 mm/s and the span length is 72 mm (Figure 5.2 (b)). Images of the specimens at various loading conditions are taken at a rate of 1 FPS (VicSnap, Correlated Solution).

5.2.4 Numerical simulation

The finite element analysis is conducted using commercial software ABAQUS (Dassault Systemes Simulia Corp., Providence, RI). Plane stress condition is assumed during the simulations. The models are meshed with 6-node triangular elements and 6 elements are generated along the width of the cell walls after a convergence test. The true stress-strain relation of VeroWhite observed from uniaxial tension is directly exported to ABAQUS and implemented as the constitutive equation for the core material. W-CFRP and U-CFRP are modeled as elastic-perfectly plastic materials. In addition, geometric nonlinearity is considered to represent the large deformation of the structure.

5.3 Poisson's ratio of core design

Figure 5.3 shows the mechanical response of re-entrant honeycomb, conventional honeycomb, and truss cellular specimens under uniaxial compression, respectively. The nominal stress-strain curves indicate these structures exhibit linear stress-strain relations up to 8% macroscopic strain. The Poisson's ratio for each specimen is determined in this linear-elastic deformation region. Figure 5.3 (c-e) shows the images of re-entrant honeycomb, conventional honeycomb and truss specimens under compression at $\varepsilon = 0$, -0.04, and -0.08, respectively. It is seen that the lateral boundaries of the re-entrant honeycomb sample shrink continuously under compression, indicating a negative Poisson's ratio of this material. While the conventional honeycomb and truss specimens exhibit lateral expansion during the uniaxial compression, which shows a positive Poisson's ratio. To quantify the deformation in the specimens during the experiments, an image processing software (ImageJ) is used to determine the position of intersection points in the specimens. Because the deformation near the four edges of the specimen is affected by boundary conditions, we focus on the behavior of unit cells in the central region of the specimens. The relations between the average horizontal strain and the avarage vertical strain of the unit cells are plotted in Fig. 5.3 (b). The local values of Poisson's ratio can be calculated by estimating the slope of the horizontal strain and vertical strain curves. Over the linear elastic deformation region, the experimental determined Poisson’s ratio is approximately a constant at $v_{12} = 1.070$ for truss, $v_{12} = 1.730$ for conventional honeycomb and $v_{12} = -1.732$ for re-entrant honeycomb, respectively, which shows an excellent agreement with the analytical estimates 1.000, 1.732 and -1.732, respectively. Here, for the purpose of ensuring a fair comparison, we design that the conventional honeycomb and the re-entrant honeycomb have the same absolute value of Poisson’s ratio, v_{12}.

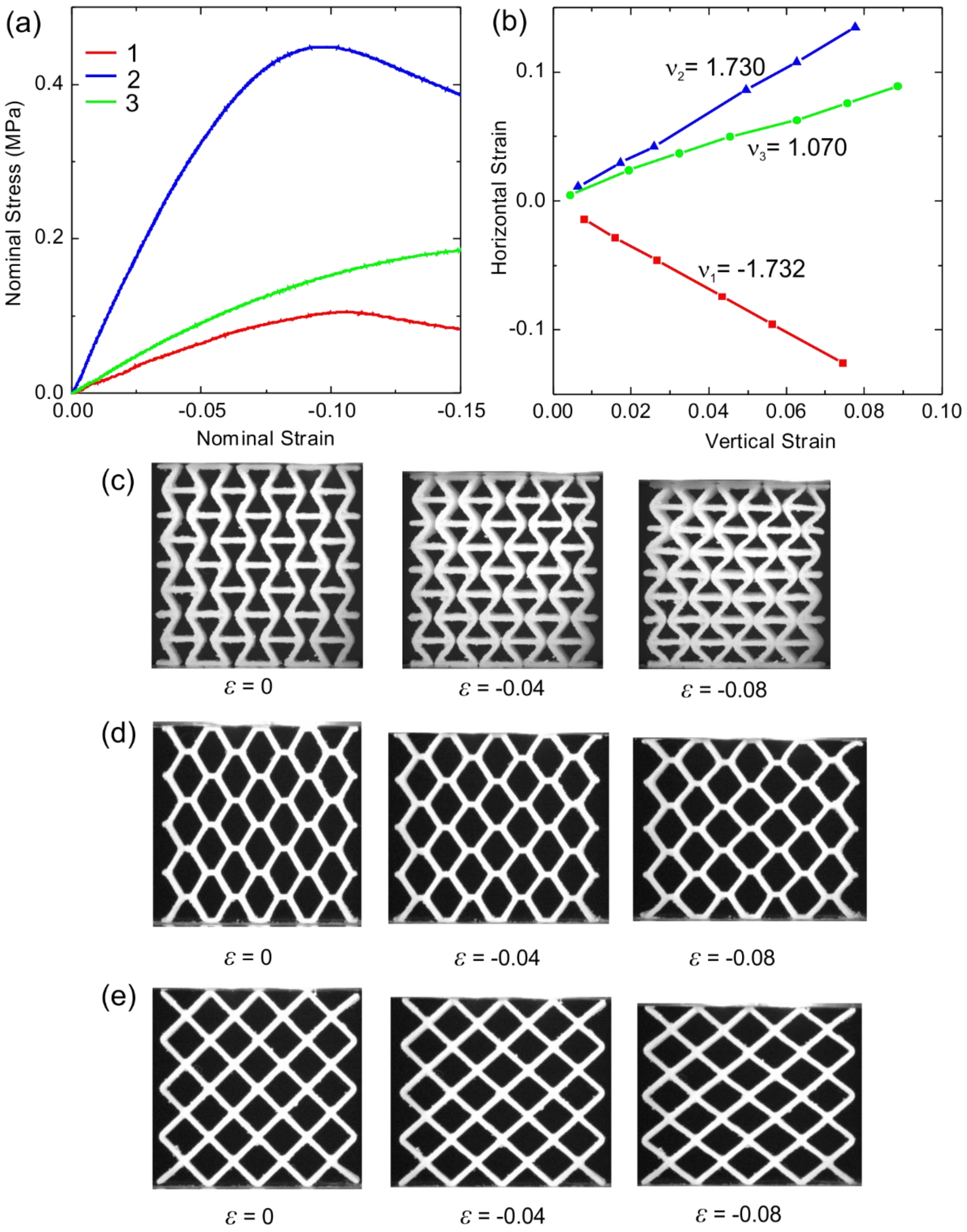

Figure 5.3 Three cellular core materials under uniaxial compression test (the volume fraction is 20%). Re-entrant honeycomb (Specimen 1), conventional honeycomb (Specimen 2), and truss (Specimen 3), respectively. (a) Nominal stress-strain curves; (b) The horizontal strain as a function of the vertical

strain, where Poisson's ratio is calculated; (c-e) each specimen under compression at strains of $\varepsilon = 0$, $\varepsilon = -0.04$, and $\varepsilon = -0.08$.

5.4 Static 3point bending behavior of sandwich composites

Having demonstrated that the re-entrant honeycomb lattice material exhibit auxetic behavior and conventional honeycomb and truss lattice material exhibit non-auxetic behavior under uniaxial compression, we now systematically investigate the bending behavior of the sandwich composite specimens with different cores and face sheets.

5.4.1 Effect of face sheets

Figure 5.4 (a) shows the load-deflection relations of the sandwich composite specimens with different face sheets: VW, W-CFRP, and U-CFRP. Here the core of sandwich specimens is a re-entrant honeycomb with a relative density of 0.2. It is clear that the face sheet material will affect the bending behavior significantly. As expected, the load-deflection relation of the sandwich specimen with VW face sheets shows the lowest force level because VW is softer and weaker than a CFRP. While for the sandwich specimen with W-CFRP face sheets, load significantly increases to the yield point ~190 N at 4 mm and maintains a plateau up to 20 mm before a complete failure. For the sandwich specimen with U-CFRP face sheets, the load-deflection curve exhibits the highest force level to a maximum of 500 N and two enhanced load stages are observed. Therefore, compared to W-CFRP, U-CFRP will significantly enhance the energy absorption behavior of the sandwich composite structures. These different mechanical responses are intrinsically controlled by the stiffness and strength of the face sheets, which is shown in Table 3. Another phenomenon could be noticed that for specimens with U-CFRP face sheets, the load-deflection curve indicates negative bending stiffness behavior due to the snap-through instabilities of the re-entrant core under loading and the details will be discussed later. The images of three sandwich specimens at a deflection of 15 mm are shown in Figure 5.4 (b). At the final stage of bending the sandwich specimen with VW face sheets shows less deformation in core ligaments while the sandwich specimen with U-CFRP face sheets exhibit the largest deformation in core ligaments. Therefore, the deformation mechanism of these sandwich composite structures with the same core material is strongly dominated by the mechanical properties of sandwich face sheets that are carrying loads by mainly tension/compression during sandwich beam bending.

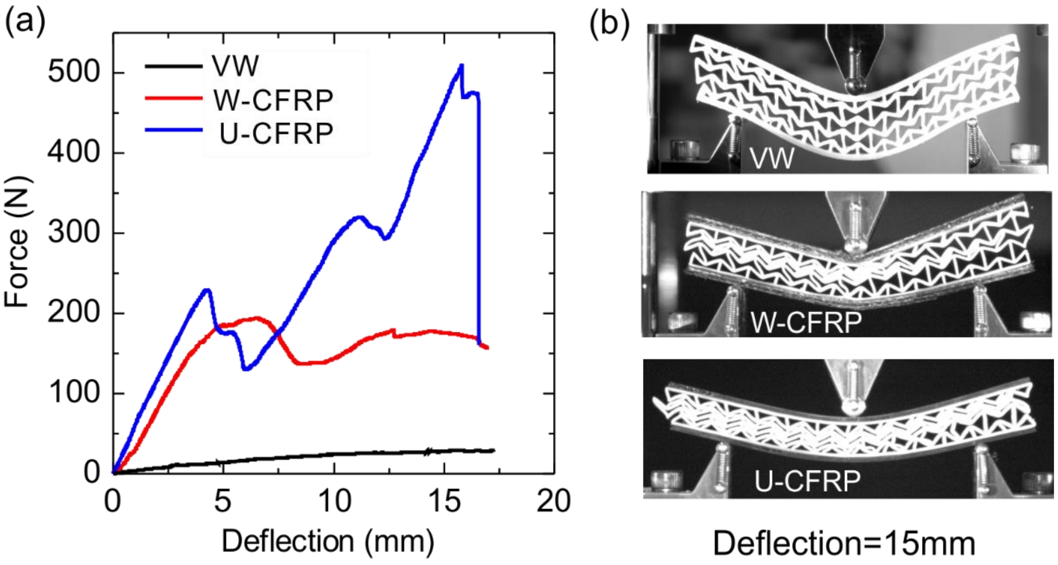

Figure 5.4 Bending characteristic of sandwich composite specimens with face sheets of different materials. The core is re-entrant honeycomb with an effective density of 0.2. (a) Load-deflection curves; (b) the images of deformed configuration of each sandwich specimen at a deflection of 15 mm.

5.4.2 Effect of core topology

The effect of the core topology on the bending behavior are examined experimentally and numerically. Here we use U-CFRP as the face sheets and the relative density of sandwich cores is 0.2 for each core topology. Figure 5.5 (a) shows that the specific core topology has a significant impact on the load-deflection curves. The truss core sandwich composite structure has the largest flexural stiffness and maximum loading forces, while the re-entrant honeycomb core sandwich composite structure has the lowest flexural stiffness and largest bending deflection. It can be easily understood as the re-entrant honeycomb has much lower Young's modulus and stress lever at the same deformation lever, as seen in Figure 5.3 (a), as compared to the other two core structures, leading to weaker mechanical response of the re-entrant honeycomb sandwich composite structure. Fig. 5(b) shows the images of three sandwich specimens at a deflection of 8mm. Core fractures occur in the truss and the conventional honeycomb sandwich composite structures, as also evident from the drops in the load-deflection curves, which indicates that these sandwich structures will fail locally. It is noticed that the shear of the core materials causes the failure of the truss and the conventional honeycomb sandwich composite structures. The shear resistance or shear strength of the core materials plays an important role during the bending of sandwich structures. Based on Gibson's model [61], we estimate the shear strength of the conventional honeycomb as : $\frac{(\tau_{pl}^{*})_{12}}{\sigma_{ys}} = \frac{1}{4}(\frac{t}{L})^{2}\frac{1}{H/L\cos\theta}$, which reduces to $0.10548*(\frac{t}{L})^{2}$. For the shear strength of the truss, we estimate the shear strength as: $\frac{(\tau_{pl}^{*})_{12}}{\sigma_{ys}} = \frac{1}{8}\frac{t}{L}$. Using our design parameters, the estimation of the effective shear resistance of these core materials, $\frac{(\tau_{pl}^{*})_{12}}{\sigma_{ys}}$, is listed in Table 5.4. We could notice that the truss structures exhibit higher shear strength than that of the conventional honeycomb, which is consistent with the experiment results. Moreover, using the scaling law $\frac{(\tau_{pl}^{*})_{12}}{\sigma_{ys}} = C*(\frac{\rho_{S}}{\rho_{C}^{*}})^{n}$, we could calculate that the scaling exponent equals to 2.267 for the conventional honeycomb and 1.103 for the truss structure, which indicates that the deformation mechanism is bending-dominated for the conventional honeycomb and stretching-dominated for the truss structure. Interestingly, no fractures are observed in the re-entrant honeycomb sandwich composite structure up to a large deflection (16 mm in this case). Instead, buckling of ligaments is seen in each layer. The buckling phenomenon does not result in the catastrophic failure but the periodic re-entrant honeycomb structures contain the buckling deformation and enable the sandwich composite structure to provide energy absorption to a larger deformation. Therefore, global failure mode controls the re-entrant honeycomb sandwich composite structures. Furthermore, the core deformation in truss and conventional honeycomb sandwich specimens are irreversible after unloading due to fractures of ligaments. On the contrary, at the same level of global deformation for the re-entrant honeycomb sandwich specimen with low density (20%), the deformation of core structures is mostly buckling of ligaments instead of fractures, which provides the possibility for these types of sandwich composite structures with strong potentials of reusable abilities. Moreover, the 3D-printed material for fabricating the core structures is a glassy polymer with shape memory effect. It is possible to use the temperature for the shape recovery after the plastic deformation, which may lower the repair costs. For the re-entrant honeycomb sandwich specimen with core density higher than 0.2, it exhibits fractures of ligaments instead of the buckling due to the low slenderness ratio of the ligaments.

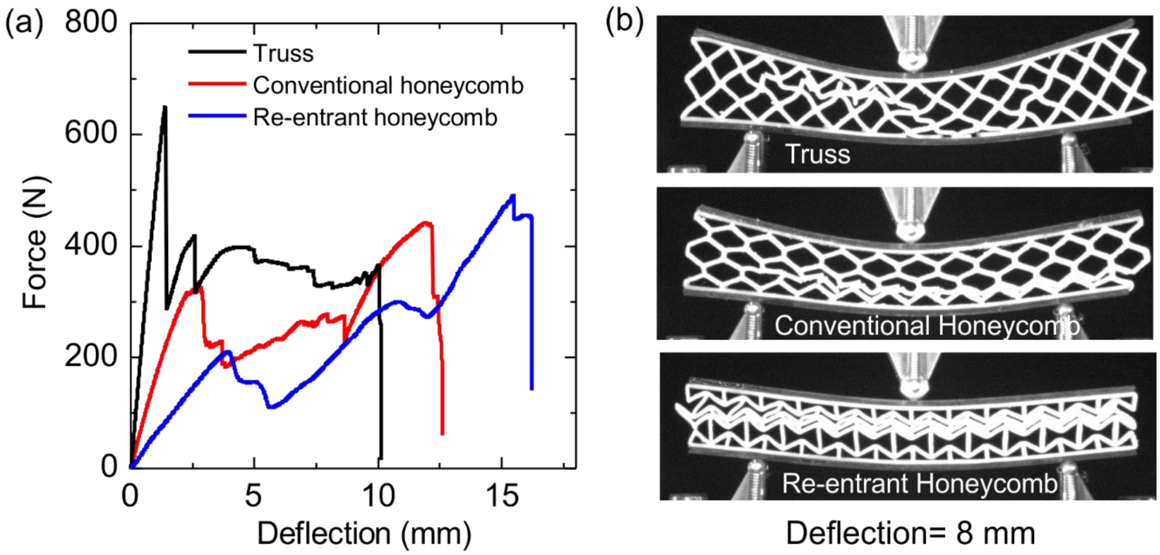

Figure 5.5 Bending characteristic of sandwich composite specimens with different core structures and U-CFRP face sheets. The effective density of core material is 0.2 for all specimens. (a) Load-deflection curves; (b) the images of deformed configuration of each sandwich specimen at a deflection of 8mm.

Table 5.4 The normalized shear strength of truss and conventional honeycomb with various relative densities.

Relative density	0.2	0.3	0.4
Truss	0.0131	0.0204	0.0282
Conventional honeycomb	0.00197	0.0048	0.0095

Figure 5.6 shows the comparison of the experiments and FEA prediction, indicating good agreement between the numerical and experimental results. Excellent agreement can be observed in the force displacement curves between the numerical and experimental results at displacement up to the yield of the sandwich specimens, as shown in Figure 5.6 (a). As larger displacement, the

experiments show failures of ligaments, leading to significant drops in the force displacement curves, which is not captured by the FEA simulation since no fracture criteria is taken into consideration in the simulations. Figure 5.6 (b) shows the deformed specimens in the experiments and Figure 5.6 (c) exhibits the corresponding specimens in the simulations. For re-entrant honeycomb sandwich composite structure, simulation confirms the buckling of vertical ligaments observed in the experimental test. Moreover, the simulated von Mises stresses show that re-entrant honeycomb sandwich composite structure exhibits relatively homogeneous stress distribution in both face sheets and core material. Especially the stress level in the ligaments is lower than those in the truss and conventional honeycomb cores. Therefore, local failure does not occur due to the less localized stress concentration. For conventional honeycomb and truss sandwich structures, it is apparent that the stress distribution is largely concentrated in the area near loading point and some certain struts where local failure would be expected. The results of the FEA simulation and the average experimental measurement calculated from Figure 5.6 (a) are listed in Table 5.5. Again, one can notice an excellent agreement on the flexural strength between the simulation and the experiment. The simulated flexural stiffness is slightly higher than the experimentally observed value, which is attributed to the base material constitutive behavior. Specifically, we use a stress-strain relation measured from uniaxial tension experiment of VW. However, during bending tests, the ligaments could be subjected to tension, compression, or bending. This complex stress state is not well captured in a simple elastic-plastic material model. Moreover, the fidelity of the 3D printed process will also affect the materials properties. Although Objet 260 has a stated resolution of ~16μm, the accuracy can still affect the volume fraction and distribution of printed materials. Anisotropy, porosity, and imperfections introduced during 3D printing also play a role. These specific aspects are not taken into consideration in our model. Compared to conventional honeycomb and truss core, the re-entrant honeycomb sandwich composites exhibit relative low flexural strength and stiffness, therefore, a larger bending deflection could be expected. These results suggest good ability to tailor the core topology to achieve different bending behaviors for certain mechanical applications.

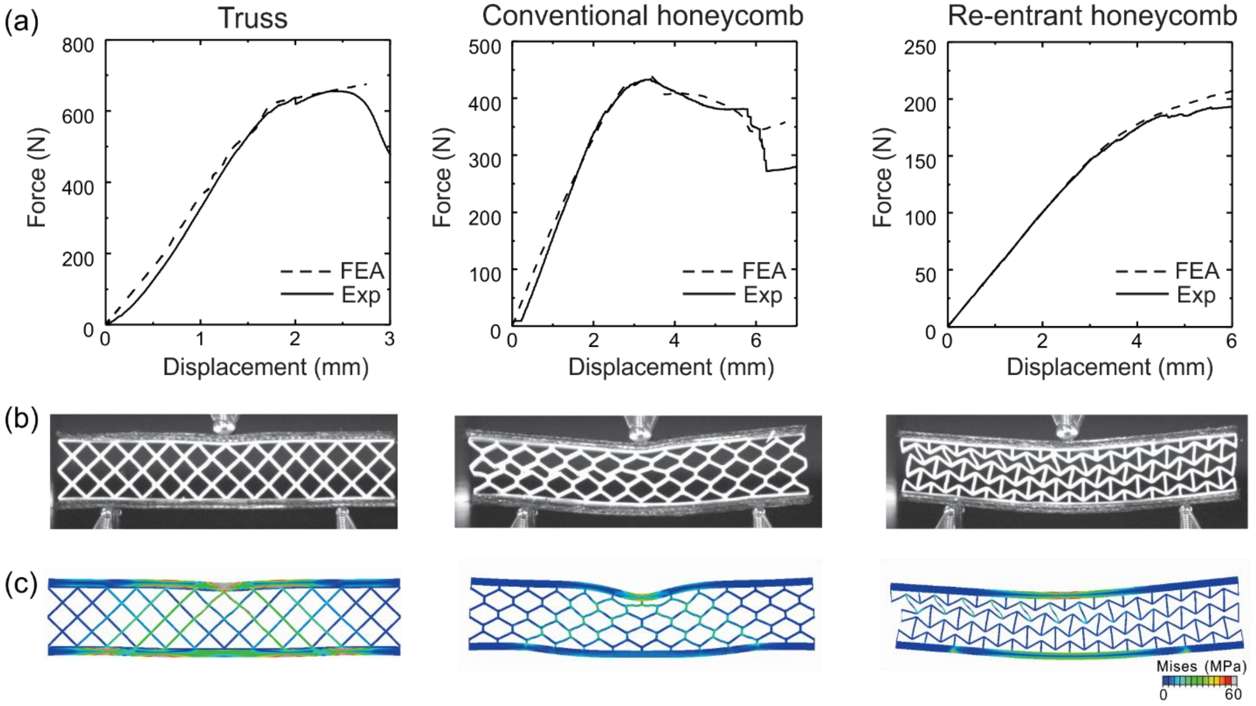

Figure 5.6 Comparison of the experiments and FEA predications for mechanical response of sandwich composites under bending deformation. (a) The force-displacement curves. (b) The experimentally deformed specimens and (c) the corresponding simulated FEA results of the three sandwich composite structures with truss composite at a deflection of 1.5mm, conventional honeycomb composite at a deflection of 2.5 mm, and re-entrant honeycomb composite at a deflection of 3.8 mm.

Table 5.5 Comparison of FEA and experimental results of the sandwich composite specimens with W-CFRP face sheets.

Core design	Measured Strength (MPa)	FEA simulated Strength (MPa)	Measured Modulus (GPa)	FEA simulated Modulus (GPa)
Re-entrant honeycomb	3.76	3.98	35.74	35.61
Conventional honeycomb	8.39	8.31	109.65	136.48
Truss	12.72	12.94	292.98	343.39

Figure 5.7 shows the load-deflection curves and the corresponding images of deformed re-entrant honeycomb sandwich specimens at different level of deflections. Interestingly, the deformation process of the sandwich beams with re-entrant honeycomb core exhibit a snap-through instability during three-point bending tests. Three re-entrant honeycomb sandwich specimens with core relative density of 0.2 are tested and show good repeatability (Figure 5.7 (a)). The load-deflection response is characterized by three peaks and drops; the first and second drops correspond to the sequential buckling of ligament layers and the third drop corresponds to the catastrophic failure of the whole structure, as shown in Figure 5.7 (b). During the bending, the vertical ligaments in the mid row of core structures will buckle first due to the core shear concentration during bending. The instability leads to a drop in the load-deflection curve, which makes the slope become negative, where negative incremental bending stiffness is observed. After the buckled vertical ligaments become in contact with the inclined ligaments in the middle row, the load increases again. The instability occurs through row-by-row, with simultaneously increasing the load level until the whole specimen is fully deflected. Furthermore, at larger deformation, the plasticity affects the behavior of instability for the re-entrant honeycomb sandwich structures [157]. The composite sandwich structure can absorb energy through bending plastic hinges which connect to two inclined ligaments and one vertical ligament. Because of the core shear, the vertical ligaments

first are buckled and then inclined to one side with the rotation of neighboring plastic hinges leading to the resistance of these plastic hinges to the external force. With increasing bending deformation, the rotation of plastic hinges will induce the contact of vertical ligaments and the inclined ligaments, which will ensure the structure to continue to carry more load.

The relative density of re-entrant honeycomb core is found to significantly affect the snap-through instability. For the core with relative density above 0.3, the instability behavior vanishes. With the increase of the relative density, the slenderness ratio of ligaments will increase, which will make the core structure more brittle. Therefore, continuous loading will lead to the local catastrophic failure instead of buckling and the resulting load-deflection curves drop dramatically. Also, the material of face sheets will affect this phenomenon which could be seen in Figure 5.4. The stiffer and stronger face sheets will be more beneficial to the instability behaviors. For the sandwich beams with conventional honeycomb core and truss core, the instability phenomenon could not be observed during three-point bending tests. Recently, the snap-through instabilities have been employed for material design in bi-stable periodic structures under compression [158-160] and tension [161]. The nonlinear mechanical response of these new classes of architected materials will significantly enhance the energy absorption ability whether via low rate quasi-static loading or via impact tests. Our sandwich structures with re-entrant honeycomb cores also exhibit the snap-through instability especially during the bending deformation. Note that, due to this deformation mechanism, the specific energy absorption of current sandwich structures is not as large as several recently developed architectured materials, such as hollow microtruss structures [162], bicontinuous structures[163], buckyball [164] and honeytube structures [165], which are shown to exhibit significantly enhanced specific energy absorption. The combination of nonlinear deformation mechanism, the open-cell nature, as well as the tunability of the sandwich structures can provide better opportunities to integrate with new functionalities.

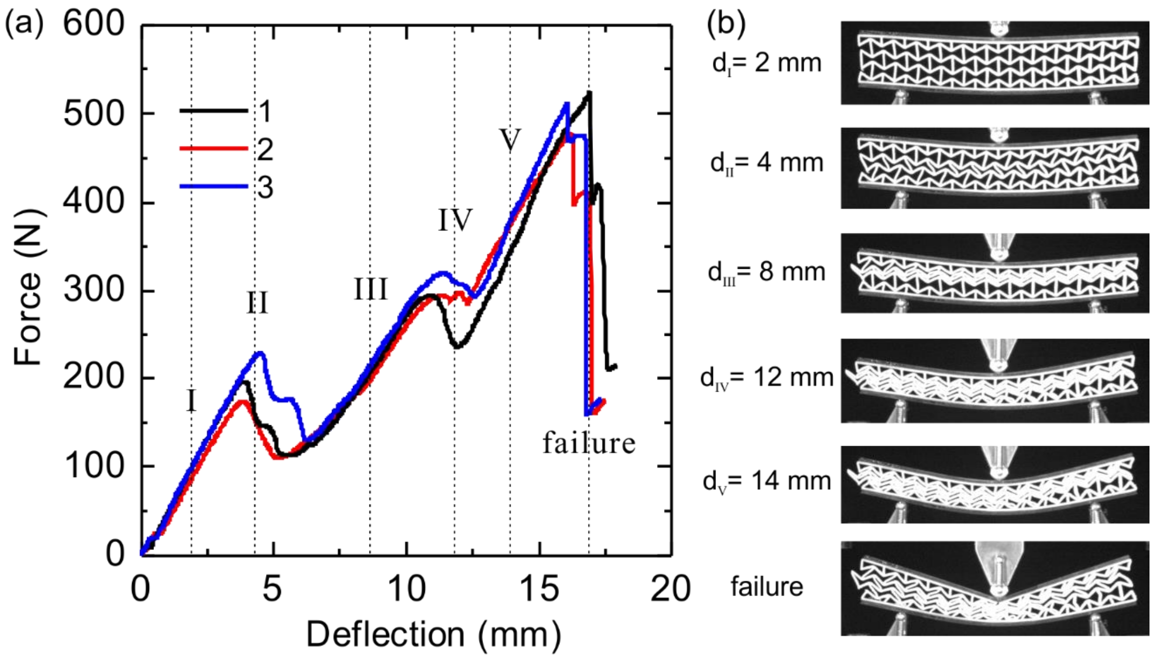

Figure 5.7 Bending characteristic of sandwich composite specimens with re-entrant honeycomb core design and U-CFRP face sheets. Three specimens are used showing repeatability. The relative density of core material for each specimen is 0.2. (a) Load-deflection curves; (b) the images of deformed configuration of sandwich specimen 3 at different deflections.

5.4.3 Effect of relative density

Figure 5.8 depicts the experimental results of the maximum force, maximum deflection, flexural stiffness, and maximum energy absorption (which we compute as the work before catastrophic failure occurs) of sandwich composite structures with three core designs and relative density from 0.2 to 0.4. With increasing the relative density, the maximum force and flexural stiffness will increase significantly and the maximum deflection will decrease. This is as expected since sandwich composite structures with higher relative density of cores will become stiffer, stronger but brittle. At any given relative density of cores, the truss and conventional honeycomb sandwich composite structures provide a larger maximum force and a larger flexural stiffness than the re-entrant honeycomb sandwich composites. The re-entrant honeycomb sandwich composite structures possess a larger deflection and slightly smaller energy absorption. For many energy absorption applications, it is required that the structure exhibit a response force just below the injury criterion and a limited densification deflection [109]. Comparing the bending properties of three composite structures, we find that the re-entrant sandwich composites exhibit significant advantages over the truss or conventional honeycomb sandwich composites. The re-entrant honeycomb sandwich has the same level of energy absorption ability but with smaller response forces and much larger densification deflections compared to the truss and conventional honeycomb sandwiches. For example, for the sandwich composites with W-CFRP face sheets and relative density of 0.4, at the force level of 400N, the re-entrant sandwich composites absorb about 100% energy (about 6J) the same as the other two sandwich composites. While at the same energy absorption level, the conventional honeycomb and truss sandwich composite structures have a response force level around 800 N and 1300 N, respectively, which is significantly higher than those in the re-entrant honeycomb sandwich composite structure. Moreover, the failure mechanism of re-entrant honeycomb sandwich is global dominant, which provides less local deformation and failure. While the non-auxetic sandwiches' deformation are irreversible after failure because of the local fractures of cores. Therefore, the re-entrant honeycomb sandwich composites are better potential candidates for energy absorption applications. Meanwhile the truss sandwich composites and conventional honeycomb sandwich composites are ideal candidates for the applications where high specific stiffness and strength are required. These results suggest we could combine numerical calculation and 3D printing technique to tailor the microstructures of sandwich composites to achieve different bending properties for certain mechanical applications.

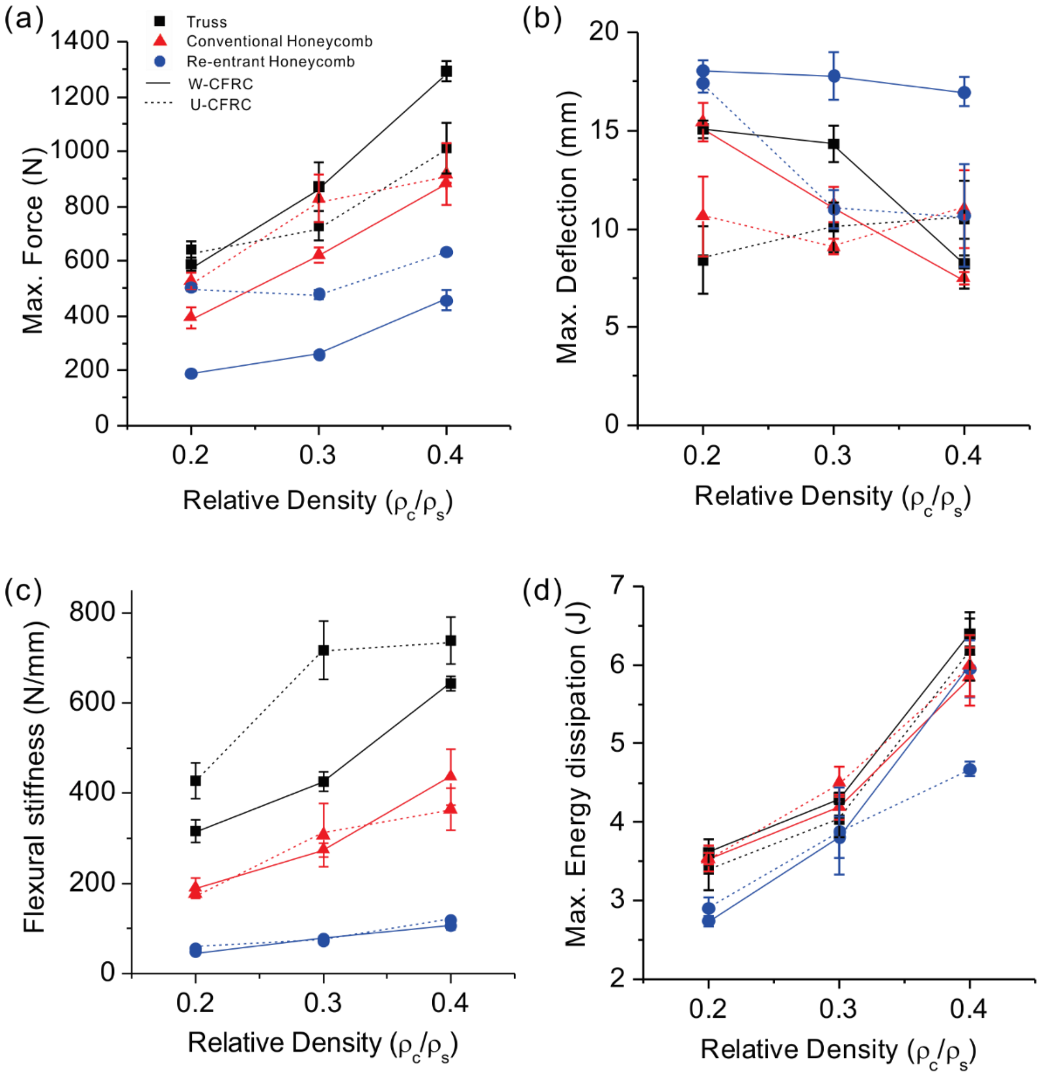

Figure 5.8 Bending properties of the sandwich structures. (a-d) Maximum force, maximum deflection, flexural stiffness and maximum energy dissipation.

We have shown that the flexural stiffness and flexural strength increase as the relative density of core material increases for the sandwich beams. Generally, for the cellular materials, such as metal foams and lattice structures, the relation between the effective elastic modulus *E* and the relative density ρ_C^* / ρ_S can be described by a power law $E = C\,(\rho_C^* / \rho_S)^n$ [61,166,167]. Therefore, these scaling laws could be used to describe the relation between the flexural stiffness and flexural strength and the relative density of cores for the sandwich composite structures. The flexural stiffness of sandwich composite structures [61,111] is calculated from the *equivalent flexural* rigidity, $(EI)_{eq}$, and the *equivalent shear rigidity*, $(AG)_{eq}$, of the beam. Found from the parallel axis theorem, the equivalent flexural rigidity of the rectangular beam, as shown in Fig. 2(a), gives

$$(EI)_{eq} = \frac{E_f bt^3}{6} + \frac{E_c bc^3}{12} + \frac{E_f btd^2}{2}\,. \tag{5.5}$$

These three terms describe the bending stiffness of the faces, the bending stiffness of the faces and of the core about the centroid, and the bending stiffness of the faces about the centroid of the beam itself, respectively. In optimal sandwich design, the first two terms are small compared to the third term. As an approximation,

$$(EI)_{eq} = \frac{E_f btd^2}{2}\,. \tag{5.6}$$

The equivalent shear rigidity is

$$(AG)_{eq} = \frac{bd^2 G_C^*}{c}\,. \tag{5.7}$$

Here the shear modulus of the core, G_C^*, can be described as a function of solid polymer modulus, E_S, and the relative density of the core structure, ρ_C^* / ρ_S, via

$$G_C^* = C_1 E_s \left(\frac{\rho_C^*}{\rho_S}\right)^n \tag{5.8}$$

where C_1 and n can be obtained by fits to experimental data.

When the load, P, is applied, the deflection δ of the sandwich beam is the sum of the bending and shear components:

$$\delta = \delta_b + \delta_s = \frac{Pl^3}{48(EI)_{eq}} + \frac{Pl}{4(AG)_{eq}} . \tag{5.9}$$

Using Eqns. (6-9), the flexural stiffness of the sandwich beam is

$$\frac{P}{\delta} = \frac{4bd^2}{\frac{l^3}{6tE_f} + \frac{cl}{C_1 E_S}(\frac{\rho_S}{\rho_C^*})^n} . \tag{5.10}$$

Furthermore, the failure modes of a sandwich beam include face yielding, face wrinkling, core failure, failure of the adhesive bond and core indentation. However, we notice the dominant failure mechanism of our sandwich specimens is the core shear. In this study, the face thickness to span ratio, *t/l*, are 0.014 for U-CFRP and 0.032 for W-CFRP. Our experimental results indicate that the face sheets do not fail, instead the core shears. If decreasing the thickness of the face sheets, the failure mode may transform from core shear to face yield, which will affect the deformation mode of the composite sandwich structures. In this way, the fractures of core materials will not happen and the total energy absorption of the re-entrant honeycomb will more rely on the strength of the face sheets. Moreover, the snap-through instability may disappear and the advantage of re-entrant honeycomb sandwich compared with the truss and conventional honeycomb sandwiches may not exist. On the other hand, while increasing the thickness of the face sheets, the strength and stiffness will increase which will keep the failure mode as core shear. In this case, the deformation mode and the capability of energy absorption of the re-entrant honeycomb sandwich structures will be well maintained. Moreover, the shear stresses in the composite material change rapidly between the core and the skin, the adhesive layer also takes some degree of shear force. For our sandwich composites, the adhesive bond between the two layers is strong so that no delamination or de-bonding is observed. The failure load [61], which is the maximum force during the three-point bending test, can be described as a function of the yield stress of solid polymer, σ_{ys} and the relative density of the core structure, ρ^* / ρ_S, via

$$P_{\max} = 2C_2 bc\sigma_{ys}(\frac{\rho_C^*}{\rho_S})^m \tag{5.11}$$

where C_2 and m can be obtained by fits to experimental data.

For sandwich composite beams with truss, conventional honeycomb, and re-entrant honeycomb cores, these parameters are given in Table 5.6. The scaling exponent n equal to 1 indicates stretch-dominated deformation behavior of the ligaments whereas an exponent of 2 typically indicates bending-dominated deformation. For the flexural stiffness, the power indexes n for the re-entrant honeycomb sandwich and the truss sandwich are around 1, so that the bending deformation for these two types of sandwich structures are almost stretch-dominated. In contrast, the power indexes n for the conventional honeycomb sandwich structures are around 2, indicating the contribution from the bending of the interconnected ligaments. Furthermore, for the flexural strength, the power indexes m are 1.98 and 1.80 for the conventional honeycomb sandwich and 1.13 and 1.08 for the truss sandwich. Compared with the scaling law of shear strength for the honeycomb and truss structures in Table 5.4, the power index from the model is 2.267 for honeycomb and 1.103 for truss, respectively, which shows a good agreement with experiment results. Moreover, the power indexes m for the re-entrant honeycomb sandwich are 1.23 and 1.46 which are larger than the n

fitted from flexural stiffness. This is because the snap-through instability behavior appears in the sandwich structures with low relative density cores. For the conventional honeycomb and the truss honeycomb sandwich structures, the power indexes of the flexural stiffness and flexural strength are almost identical for each structure which means the flexural stiffness and flexural strength are mostly determined by the deformation mechanism resulting from the topology of sandwich cores.

Table 5.6 The relations of the flexure stiffness and strength to the relative density of core designs for the sandwich composite structures.

Sandwich structures		Flexural stiffness		Flexural strength	
Core	Face sheets	C_1	n	C_2	m
Re-entrant Honeycomb	W-CFRP	0.0126	1.17	0.0547	1.23
	U-CFRP	0.0128	1.08	0.1019	1.46
Conventional Honeycomb	W-CFRP	0.1209	2.00	0.1076	1.98
	U-CFRP	0.1526	1.93	0.1443	1.80
Truss	W-CFRP	0.0609	1.00	0.1491	1.13
	U-CFRP	0.0672	0.92	0.2231	1.08

5.4.4 Discussion

In practical applications, the sandwich composites are increasingly considered to be used in aircrafts, marine structures, portable structures, special vehicles, and some sport equipment. For example, there is a wide range of naval structures being developed using fiber reinforced polymer composites, including patrol boats built completely of composites, super structures, decks, and masts in frigates and destroyer and even internal equipment and fittings[168]. These sandwich composites are usually exposed to severe static and dynamic loads which are related to the penetrating/impact loading. Therefore, we investigate the mechanical behaviors under three-point bending test instead of four-point bending test with consideration of penetration resistance. Recently, 3D porous architectures composed of a continuous surface including the triply periodic minimal surfaces [169-171] exhibit enhanced strength and stiffness at relative low density and they can also serve as potential core materials for sandwich composites with better mechanical performance. Interestingly, additional fillers, such as sand, polymer foam, liquid, and silicon rubber [172-175] in the cellular structures can decrease the stress concentration and enhance the stiffness, strength and energy absorption of the cellular structures in the sandwich structures. Future work will explore more geometrical and topological structures to combine the deformation of co-continuous phases to achieve higher mechanical performance.

5.5 Conclusions

We have manufactured a novel class of sandwich composite structures with 3D-printed core materials and CFRP face sheets. Truss, conventional honeycomb, and re-entrant honeycomb are designed as the core material topologies. Under uniaxial compression, the truss and conventional honeycomb structures provide a non-auxetic behavior while the re-entrant honeycomb structure provides an auxetic behavior as expected. The evaluated Poisson's ratio for each structure consists well with the theoretical prediction. Three-point bending tests are conducted and the flexural stiffness, flexural strength, and energy absorption are evaluated on these sandwich composite structures. Our experimental and numerical results show a very good agreement in terms of the deformation pattern, flexural stiffness, and flexural strength. Under bending, the re-entrant honeycomb sandwich structures show an interesting global failure mode because of the relatively homogeneous stress distribution. Moreover, the re-entrant honeycomb sandwich structures exhibit sequential snap-through instabilities which significantly increases the energy absorption capacity. In contrast, the truss and conventional honeycomb sandwich structures show catastrophic failure earlier due to the localized stress concentration. The findings presented here provide new insights into the development of sandwich composite structures with unique mechanical properties for a wide range of mechanical and structural applications.

Chapter 6. Enhanced mechanical performances of auxetic composites

6.1 Introduction

Materials exhibiting a negative Poisson's ratio, also called auxetic materials [134], are a new type of mechanical metamaterials which will contract (expand) transversally when they are axially compressed (stretched). Since the 1980s, auxetic behavior has been reported in many two-dimensional (2D) and three-dimensional (3D) structures of natural systems, including cubic metals [176], zeolites [40,177], natural layered ceramics [41], silicon dioxides [178], single-layer graphene [43,44], and 2D protein crystals [179]. Since the auxetic behavior potentially equips materials with improved properties, including shear modulus [75], indentation resistance [180], fracture toughness [34,132,181], and energy absorption ability [67,134,137,182-184], there are significant interests in the development of negative Poisson's ratio materials because of their potential applications, such as textile [185-188], automotive [189], military [190,191], biomedical [192,193], and aerospace engineering [194]. Research in this area began in earnest from the computational works of Wojciechowski [195] as well as the development of 3D polymeric foams with isotropic auxetic behavior by Lakes [75]. Subsequently, several geometries and mechanisms have been proposed to achieve a negative Poisson's ratio and a significant body of man-made auxetic materials and structures has been fabricated and synthesized from the macroscopic down to molecular levels. Among them, there are in planar foams [196], honeycombs with inverted cells [76,77,197], 2D and 3D chiral lattices [51,78,156,198-200], rigid rotating hexamers or squares [80-82,201], origami/kirigami based metamaterials, [27,48,49,84-86] and hierarchical metamaterials with fractal cuts [50,87,202]. Recently, theoretical models indicate the possibility to achieve auxeticity in some colloidal crystals [203]. A detailed analysis of the deformation mechanisms of 2D and 3D auxetics can be found in Ref [204]. Due to the bending or rotation deformation nature of the ligaments/elements in these auxetic materials, however, they usually have relatively low stiffness, limiting their applications where lightweight, high stiffness, strength, and energy absorption are simultaneously desired.

Composite materials with rationally designed structures and compositions could overcome this limitation. In a two-phase composite, each constituent phase can contributes its own properties in a quite independent manner to the overall performance of the composites synergistically. For example, composite materials where auxetic lattice structures are used as the reinforcements and the nearly incompressible soft material is employed as a matrix have great potential in achieving a design to combine these prominent mechanical properties. Conceptually, by harnessing the negative Poisson’s ratio effect of the auxetic reinforcement, the soft matrix will be in a state of biaxial or triaxial compression, resulting in a synergistic improvement in the mechanical response. Indeed, composites materials with auxetic reinforcements have been designed and fabricated in the past few decades. The auxetic fibers embedded in the composite as the reinforcement would expand when stretched and prevent the occurring of fiber pullout, therefore, the load required to cause structural failure will significantly increase [205-207]. In addition, composites using 3D auxetic textile structures as the reinforcement have been fabricated and exhibited strong auxetic behavior [208]; however, relatively poor mechanical properties are observed as compared with non-auxetic composites [209]. Composites with elliptic inclusions exhibit auxetic effect with relative lower Young’s modulus compared with the non-auxetic composites as evidenced by the finite element analysis [210]. It should be pointed out that these undesired mechanical properties of composite materials with auxetic reinforcements are partially due to the limitation of conventional manufacturing techniques. In this regard, additive manufacturing techniques have shown unparalleled advantages, as they enable us to fabricate complex topologies with fine features quickly, cheaply, and at a large scale, and offer a multitude of materials with varying mechanical properties [14,211]. For example, auxetic structures fabricated using selective laser sintering and filled with strain rate sensitive material exhibit slightly increased energy absorption ability during impact tests [212]. Despite considerable efforts have been devoted to designing and synthesizing composites with auxetic reinforcements, the quantitative understanding of the interplay between the auxetic behavior and the other mechanical properties such as stiffness, strength, and toughness is still elusive. For example, systematic studies on mechanical properties of the composites with auxetic reinforcements in comparison with non-auxetic reinforcements have not been largely explored [182,206,213]. Furthermore, the effect of negative Poisson's ratio on the mechanical properties such as stiffness, strength, and energy absorption of the auxetic composites is still not clear.

In this work, we design a group of composite materials consisting of two types of auxetic reinforcements and a nearly incompressible soft elastomer as the filled matrix. The coupled geometry and material design concept is realized by an advanced 3D printing technique, which enables the fabrication of bimaterial composites with various geometries and material selections. Uniaxial compression tests are conducted to investigate the mechanical properties of these composite materials with auxetic reinforcements. Finite element simulations are performed to provide additional insights into the underlying mechanisms responsible for the observed unusual mechanical performance. Moreover, parametric analyses are conducted to quantitatively understand the effects of Poisson's ratio and volume fraction of the auxetic reinforcements on the mechanical properties of the auxetic reinforced composites.

6.2 Design and fabrication of auxetic composites

6.2.1 Design of auxetic lattice reinforced composites

The model system of the auxetic reinforced composites studied here is based on microstructures which combine the lattice structures and their inverse domains. Here two types of auxetic lattice structures are considered including a re-entrant honeycomb and a chiral truss, as shown in Figure 1(a). For the purpose of comparisons, two types of regular lattice structures exhibiting a non-negative Poisson's ratio are also designed (Figure 6.1 (a)). By filling the inverse domains of each lattice structure with another material as the matrix, we can design the lattice structure reinforced composites. The symmetry and volume distribution in these structures can be precisely controlled by tailoring the thickness of ligaments in each lattice structure. Figure 6.1 (b) displays the proposed re-entrant honeycomb reinforced composites, chiral truss reinforced composites, regular honeycomb reinforced composites, and truss reinforced composites, where the volume fractions of the reinforcing phase are all set to 20%. In our designs, the phase of lattice structures is set as the reinforced domain, which is fabricated with a glassy polymer (VeroWhite), and the inversed phase is set as the matrix domain, which is fabricated with a rubber-like material (TangoPlus).

6.2.2 Sample fabrication

The specimens were fabricated using an Objet Connex260 multi-material 3D printer (Stratasys, Ltd), which allows simultaneous printing of two different materials. The specimens for compression tests consist of 4 × 4 unit cells, resulting in prototype dimensions of 40 mm × 40 mm, which are shown in Figure 6.1 (c). Focusing on the 2D in-plane mechanical behavior of these structures, we, therefore, design the thickness of the specimens as 20 mm to avoid the out-of-plane deformation. The minimum geometric size of the lattice reinforcement in the composites is around 200 μm, which is at least one order of magnitude greater than the minimum resolution (16 μm) provided by the 3D printer. Considering the anisotropic nature of the 3D printing, all the specimens were printed along the same orientation to avoid the influence of the layer orientation on the mechanical properties of the material. The as-fabricated specimens were kept at room temperature for 7 days to allow for the saturation of the curing.

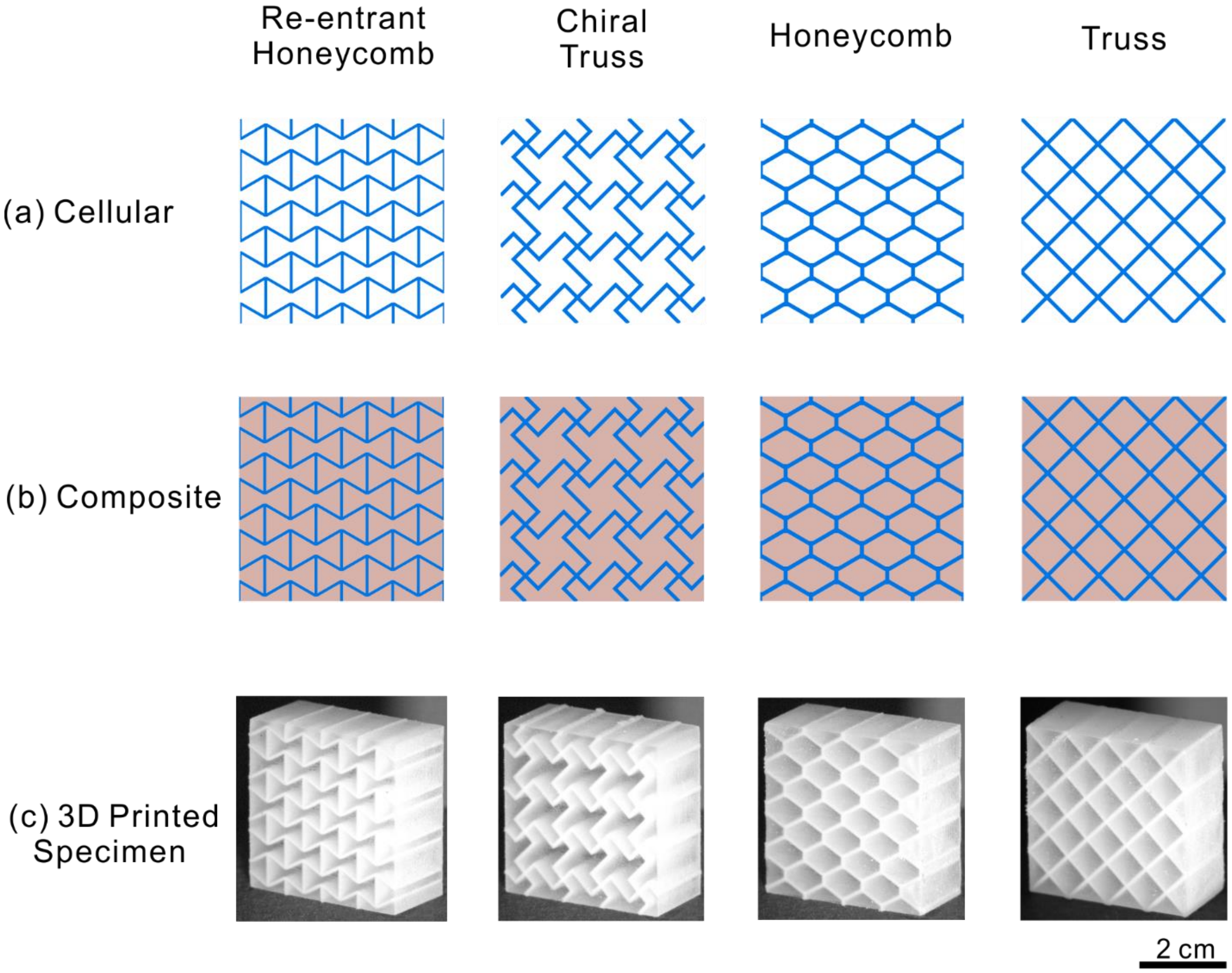

Figure 6.1 Schematics of lattice structures, lattice reinforced composite structures and 3D-printed lattice reinforced composite specimens. Schematics of (a) lattice structures, (b) lattice reinforced composite structures and (c) 3D-printed lattice reinforced composite specimens consisting of 4 × 4 unit cells with re-entrant honeycomb, chiral truss, honeycomb, and truss structures.

6.2.3 Mechanical testing

To capture the mechanical response of the 3D printed constituent materials (VeroWhite and TangoPlus), the uniaxial compression tests of cylinder samples were performed based on ASTM D695 standard. The uniaxial compression tests for cylinder samples and the cubic composite samples were performed using a MTS mechanical tester (C43) with a 10 kN load cell. All the experiments were conducted in a quasi-static regime with a constant strain rate of 0.001 s^{-1}. The load-displacement curves measured from the uniaxial compression tests were then transferred into nominal stress-strain behaviors based on the measured dimensions of the specimens. Young's modulus was calculated from the initial linear region of the nominal stress-strain curves. The energy absorption was computed as the work under the nominal stress-strain curve before 25% uniaxial compressive strain for each composite sample. Images of the specimens at various loading conditions were taken at a rate of 1 FPS (Vic Snap, Correlated Solution). The deformation and displacement contours of the samples were tracked by using DIC (Vic-2D, Correlated Solution). The image processing software (ImageJ 1.49 q) was used to determine the displacement of the center area of the specimens in order to calculate the Poisson's ratio at each level of applied compression.

6.2.4 Finite element analysis

The numerical simulations related to the mechanical response of the lattice reinforced composites under uniaxial compression were conducted using the commercial FE package ABAQUS/Standard (Simulia, Providence, RI). Models with 4 × 4 unit cells are used in all of the simulations. All models are generated by plane strain elements CPE4R and meshed after a convergence test. In addition, geometric and material nonlinearities are taken into consideration to enable the large deformation of the structure. Due to the layer by layer manufacture process of 3D printing, the mechanical properties of the printed samples strongly depend on the printing directions [214]. While in our numerical simulations, an isotropic material model is adopted. The constituent phases are taken to be a glassy polymer and an elastomer material. The stress-strain behavior of the glassy polymer is captured using an elastic-viscoplastic model which is exported from the true stress-strain relation of VeroWhite as shown in Figure 6.2. The elastomeric stress-strain behavior of TangoPlus is modeled as a hyperelastic material based on the Arruda-Boyce hyperelastic model [215] with an initial shear modulus of 0.213 MPa and locking stretch of 1.90. To simulate the experimental conditions in the numerical analysis, a uniaxial displacement loading is applied on the top surface, while the bottom is fixed along the vertical direction.

6.3 Compression behavior of auxetic composites

3D printed constitutive materials are first mechanically tested under uniaxial compression by following the ASTM D695 standard. Figure 6.2 shows the compressive stress-strain responses of the two constitutive materials and the mechanical properties extracted from these stress-strain curves are presented in Table 6.1. For the 3D printing material VeroWhite, the stress-strain behavior exhibits initial linear elasticity, yielding, post-yield, strain softening, and subsequent strain hardening at larger strains (see Figure 6.2 (a)). While for 3D printing material TangoPlus, the stress-strain curve is J-shape indicating a hyperelastic behavior. These measured mechanical responses and extracted data will be implemented in the commercial finite element software.

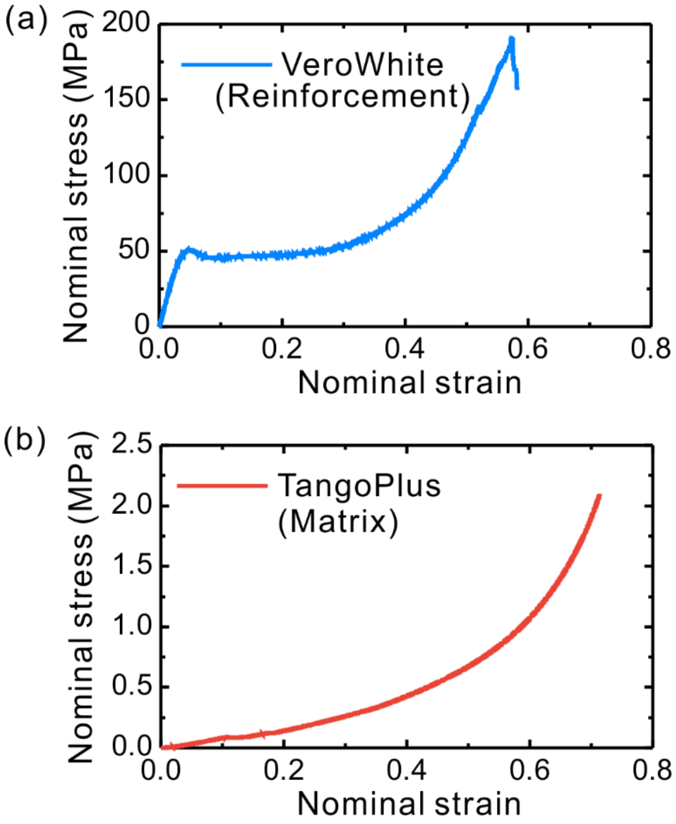

Figure 6.2 The stress-strain response of 3D printed constituent materials. The stress-strain response of the (a) VeroWhite (reinforcement phase) and (b) TangoPlus (matrix phase) materials used in this study.

Table 6.1 Mechanical properties of the 3D-printed constitutive materials.

Material	Young's Modulus (MPa)	Compressive Yield Strength (MPa)	Ultimate compressive strength (MPa)	Toughness (J/m^3)	Energy absorption (strain=0.25) (J/m^3)
VeroWhite	1513	50.5	187.5	42.3	11.0
TangoPlus	0.77	-	~2.1	0.38	0.02

6.3.1 Mechanical response of auxetic lattice reinforced composites

We first examine the compressive behavior of the auxetic lattice reinforced composites from an experimental standpoint. Four types of architected lattice reinforced composites with re-entrant honeycomb, chiral lattice, regular honeycomb, truss lattice topology are fabricated using 3D printing (Figure 6.3 (a)). Here, we use the same volume fraction of reinforcement phase of 20%. The stress-strain curves show good repeatability for each composite as can be seen in Figure 6.3 (b). The re-entrant honeycomb reinforced composites demonstrate clear superiority over the other three composites. A sudden drop in the stress-strain response of the re-entrant honeycomb reinforced composites is observed after the stress reaches its maximum. This is because of the instability of the re-entrant honeycomb structures during compressive deformation which will locally maximize the stress, resulting in a catastrophic failure. While the curves of the chiral lattice, regular honeycomb, and truss honeycomb reinforced composites exhibit smooth curved transition up to a strain of 0.3, which is due to the stability of the structures. Figure 6.3 (c) quantitatively shows that the Young's modulus of the re-entrant honeycomb reinforced composites are four times larger than that of the chiral truss and regular honeycomb reinforced composites, and five times larger than that of the truss reinforced composites. Moreover, the energy absorption at a strain of 25% of the re-entrant honeycomb reinforced composites is three times larger than that of other three types of composites. Because re-entrant honeycomb lattice [216] and chiral lattice [78] are two typical auxetic structures with negative Poisson's ratio effect (see in Figure 6.4 (e)), these results clearly show the advantage of employing auxetic lattice geometries especially re-entrant honeycomb structure in enhancing the mechanical properties of lattice reinforced composites.

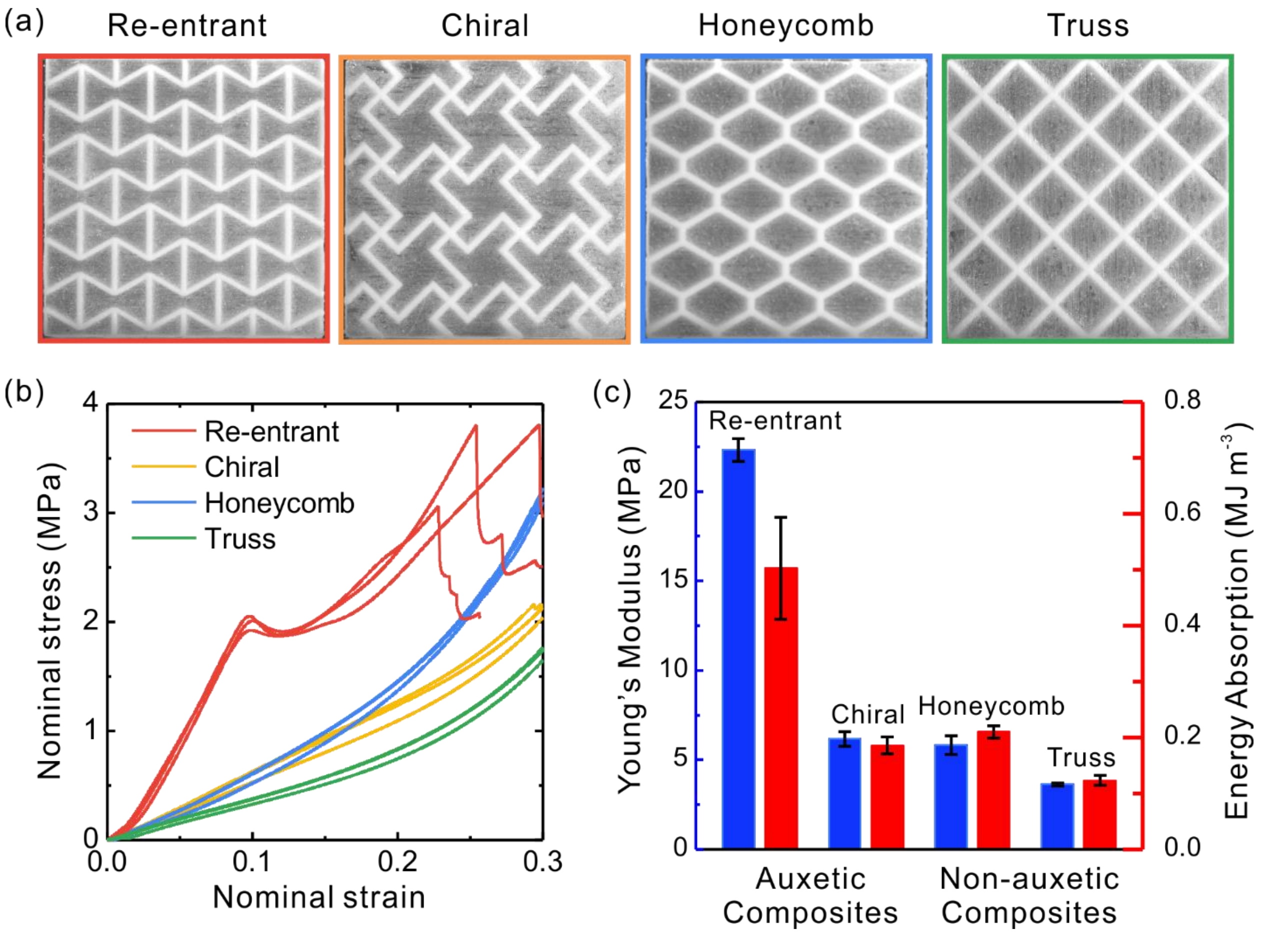

Figure 6.3 Mechanical response of the 3D-printed lattice reinforced composites during uniaxial compression tests. (a) The 3D-printed composites with a re-entrant honeycomb reinforced, chiral truss reinforced, regular honeycomb reinforced, and truss reinforced designs. (b) Nominal stress and strain curves for various designs. For each design, three specimens are tested to validate the repeatability. (c) Calculated Young's modulus from the initial linear region of the nominal stress-strain curves and computed energy absorption as the work under the nominal stress-strain curve before 25% uniaxial compressive strain for each composite sample.

Figure 6.4 shows a series of images that exhibit the deformation behavior of these four lattice reinforced composites at different strain levels. It is clear that at a small compressive strain (<0.05), the re-entrant honeycomb reinforced composites exhibit a lateral shrinkage in average, which indicates that the auxetic lattice reinforced composite still has auxetic behavior at small deformation, as shown in Figure 6.4 (a). However, the instability of re-entrant honeycomb reinforced composite can be observed starting from the strain of 0.1, resulting in a peak stress in the stress-strain curve as seen in Figure 6.3 (b). Moreover, the instability of the structures under continuous compressive loading causes a local stress concentration, leading to the failure of the re-entrant honeycomb reinforced composite at a strain of around 0.3. Although the chiral lattice is also an auxetic structure, the chiral lattice reinforced composites do not exhibit obvious auxetic behavior at small deformation, as shown in Figure 6.4 (b). This is because the matrix elastomer as the inverse phase inhibits the rotation of the chiral reinforcement phase, resulting in a reduced lateral shrinkage. In contrast to the auxetic lattice reinforced composites, both the regular honeycomb and the truss reinforced composites exhibit a clear lateral expansion during the deformation in Figure 6.4 (c)-(d). Figure 6.4 (e) shows the experimental and numerical study of the Poisson's ratios for all four lattice reinforced composites and their corresponding cellular counterparts under uniaxial compression tests. To quantify the deformation taking place in the composites during the experiments, we calculate the deformation change by identifying four points in the center avoiding the deformation near the four edges of the specimen under the influence of boundary conditions, see in Figure 6.4 (f). Here, the rectangular frames represent the original edges of the specimens before the compressive deformation. One can notice the lateral shrinkage of the re-entrant honeycomb reinforced composites, slightly lateral shrinkage combined with the rotation of the chiral lattice reinforced composites and the lateral expansion of the honey comb and truss reinforced composites at a macroscopic compressive strain of 0.05. Experimental and numerical results related to the Poisson's ratios are in excellent agreement for the four types of composites. Note that, for non-auxetic structures (truss and regular honeycomb), the Poisson's ratios of the composites and the corresponding cellular counterparts are almost identical, indicating no change in terms of deformation mechanism. However, for the chiral lattice, the Poisson’s ratios of the composite are negative and much larger than that of the cellular counterpart. This is because the matrix phase obstructs the rotation of the chiral lattice, which decreases the auxetic behavior of structures. Moreover, for re-entrant honeycomb, the Poisson’s ratio of the composite is slightly larger than that of the cellular counterpart, indicating that the matrix phase has minor effects on the shrinkage of re-entrant honeycomb lattice. Therefore, the re-entrant honeycomb reinforced composites also have as strong auxetic behavior as the re-entrant honeycomb cellular counterpart. This auxetic behavior of the composites contributes the enhancement of mechanical properties of the auxetic lattice reinforced composites.

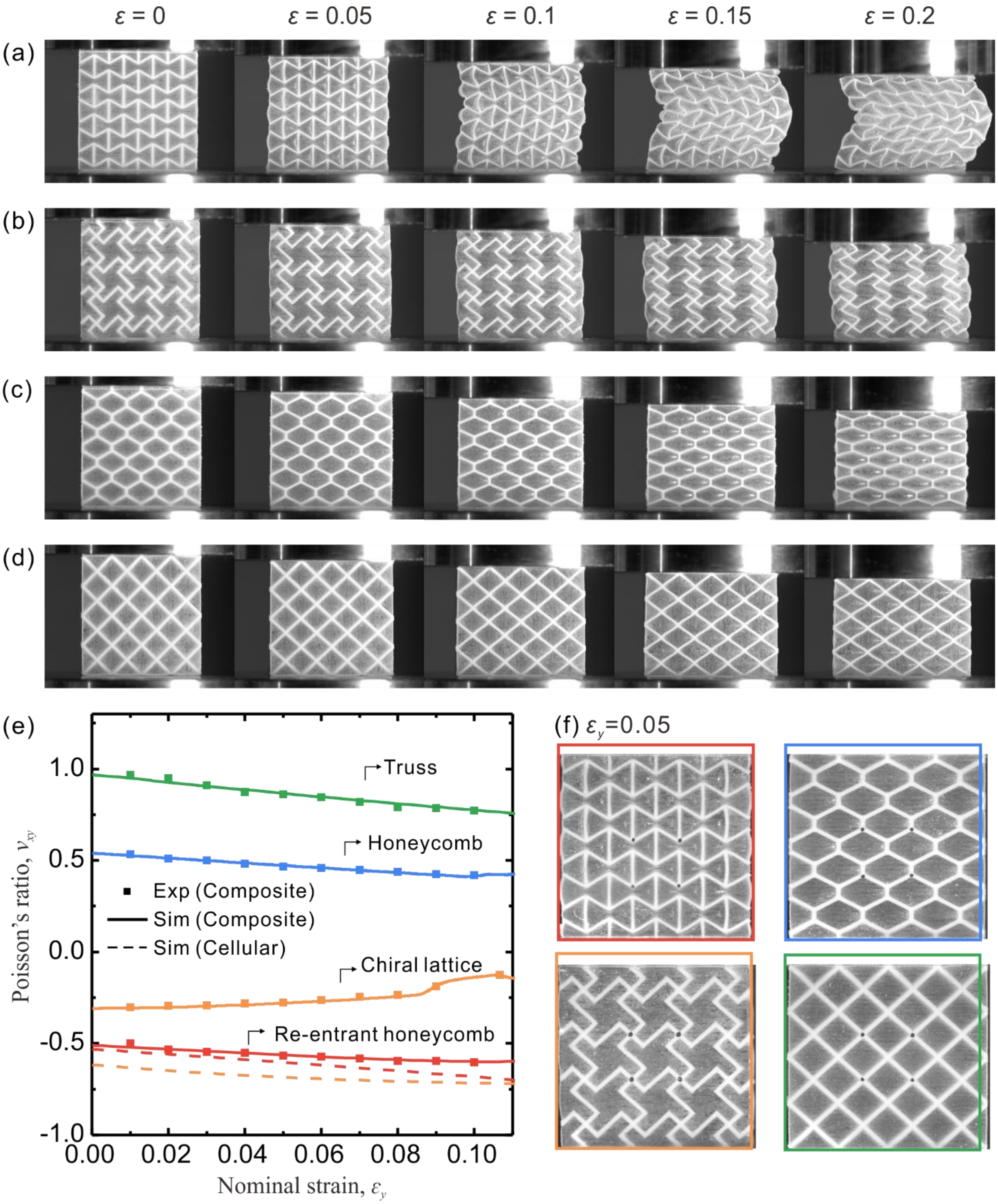

Figure 6.4 Experimental images of deformation and the calculated Poisson's ratios for each composite design. Experimental images of (a) re-entrant honeycomb reinforced composites, (b) chiral truss

reinforced composites, (c) regular honeycomb reinforced composites, and (d) truss reinforced composites at different levels of macroscopic strain: 0, 0.05, 0.1, 0.15 and 0.2 during uniaxial compression tests. (e) Experimental and numerical results of the Poisson’s ratios for lattice reinforced composites and the corresponding cellular counterparts under uniaxial compression tests. (f) Experimental images at a macroscopic strain of 0.05 for each composite. The rectangular represent the original edges of the specimens before the compressive deformation.

To further understand the compressive behavior of these lattice reinforced composites and explain the superior mechanical properties of re-entrant honeycomb reinforced composites, we use Digital Image Correlation (DIC) (VIC-2D, Correlated Solutions) to analyze the experimental displacement contours. The images in Figure 6.5 exhibit the horizontal displacement contours of four lattice reinforced composites at a vertical compressive strain of 0.05. We notice that the re-entrant honeycomb reinforcement phase exhibit shrinkage in the horizontal direction which increases the load transfer between the glassy polymer and the elastomer in Figure 6.5 (a). The chiral lattice reinforced composite has the asymmetry displacement contours on the surface, as shown in Figure 6.5 (b), due to the rotation mechanism when deformed. Compared with auxetic reinforced composites, the regular honeycomb, and the truss reinforced composite exhibit clear homogeneous horizontal expansion both in reinforcement phase and matrix phase, as shown in Figure 6.5 (c)-(d). It is clear that in non-auxetic reinforced composites the elastomer matrix phase is only compressed in the vertical direction. By contrast, the elastomer matrix phase of the auxetic reinforced composites, especially the re-entrant honeycomb reinforced composite, is squeezed in both vertical and horizontal directions, indicating a state of biaxial compression. Therefore, the auxetic reinforced composite exhibit significantly enhanced mechanical properties during uniaxial compressive deformation.

(a) Re-entrant Composite (b) Chiral Composite

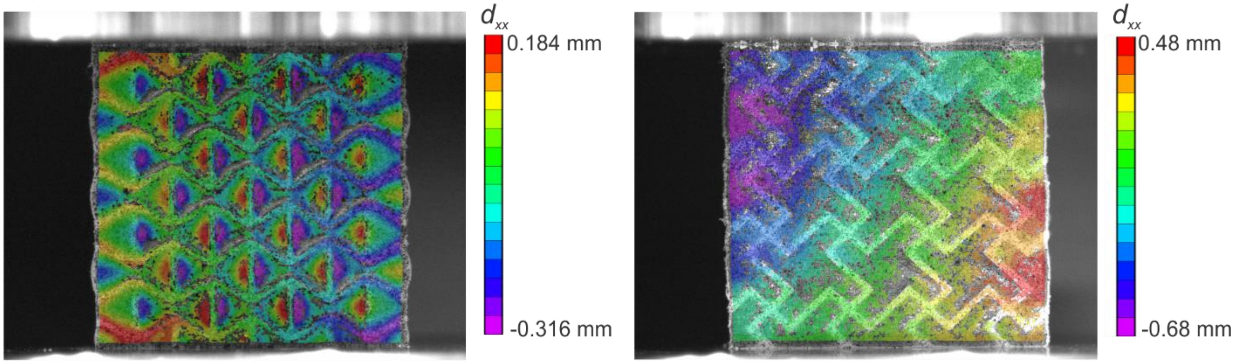

(c) Honeycomb Composite (d) Truss Composite

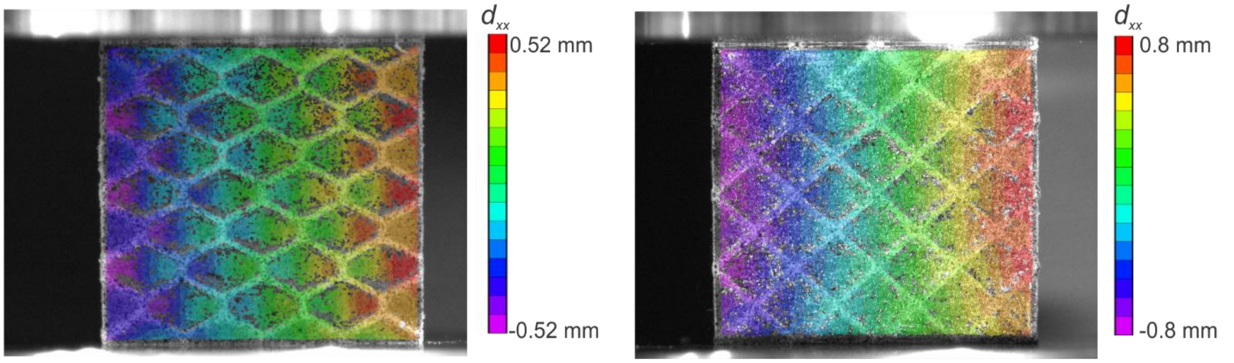

Figure 6.5 Experimental displacement contours for each composite design. Experimental displacement contours of (a) the re-entrant honeycomb reinforced composites, (b) the chiral truss reinforced composites, (c) the regular honeycomb reinforced composites, and (d) the truss reinforced composites using digital image correlation at a macroscopic strain of 0.05 during uniaxial compression tests.

6.3.2 Comparisons between auxetic lattice and auxetic lattice reinforced composites

It is known that typical cellular microstructures are used to achieve a negative Poisson's ratio, so that as expected the stiffness if not that high [193,217] And based on different deformation mechanisms, existing auxetic cellular solids can be roughly classified into two categories: symmetric units with re-entrant angles, and asymmetric units that rotate when deformed. The deformation mechanism for them is mostly rotation induced bending-dominated. However, some cellular structures such as honeycomb, octet, Kagome, etc., have stretching dominated deformation mechanism, therefore, exhibiting higher effective stiffness. We have shown that by exploiting the negative Poisson's ratio lattices into the composite design, improved mechanical properties such as stiffness, toughness can be achieved. To further show the superiority of the auxetic lattice reinforced composites, we compare the mechanical properties of lattice reinforced composites and their lattice cellular counterparts under uniaxial compression tests (Figure 6.6). The stress-strain curves combined with the deformation images of the composites and their counterpart cellular structures at the compressive strain of 0.25 are also shown in Figure 6.6 (a)-(d). For the re-entrant honeycomb and chiral cellular, the local instability occurs layer by layer with increasing strain, which makes the stress level keep on a plateau. For the regular honeycomb and truss cellular, buckling of some local ligaments also makes the stress level on a plateau. By contrast, these composites exhibit a strain hardening effect under the uniaxial compression. This is because the elastomeric matrix phase provides the additional support of this structures, which increases the stress level. Moreover, combining the lattice phase of glassy polymer with the matrix phase of rubber-like polymer enables the deformation mechanism from the local deformation to the global mechanism. This is because the matrix phase spreads the plastic deformation and decreases both the stress concentration and the local deformation. Therefore, the mutual constraints between two phases of the composites change the local instability to a global instability (auxetic lattice) or local buckling to a global non-catastrophic dissipative event (non-auxetic lattice). The calculated Young's modulus and energy absorption are presented for each composite and its cellular counterpart in Figure 6.6 (e)-(h). As expected, the typical auxetic cellular structures including re-entrant honeycomb and chiral lattice both exhibit lower stiffness and lower energy absorption comparing to regular honeycomb and truss, as seen in Figure 6.6 (e) and (g). Because the negative

Poisson's ratio of the auxetic cellular structure is obtained through bending and/or rotation inside the microstructure, this also reduces their stiffness as compared to the case of non-auxetic cellular structure with stretching-dominated ligaments. Interestingly, when we use the auxetic lattice structure as a reinforcement phase in a composite, the auxetic behavior will enforce both the stiffness and energy absorption of the composites. For re-entrant honeycomb reinforced composites, the enhancements of stiffness and energy absorption are 9 and 18 times larger than that of the re-entrant honeycomb cellular structures, respectively. However, little enhancement of stiffness is observed in the non-auxetic reinforced composites comparing to their cellular counterparts (see Figure 6.6 (f)).

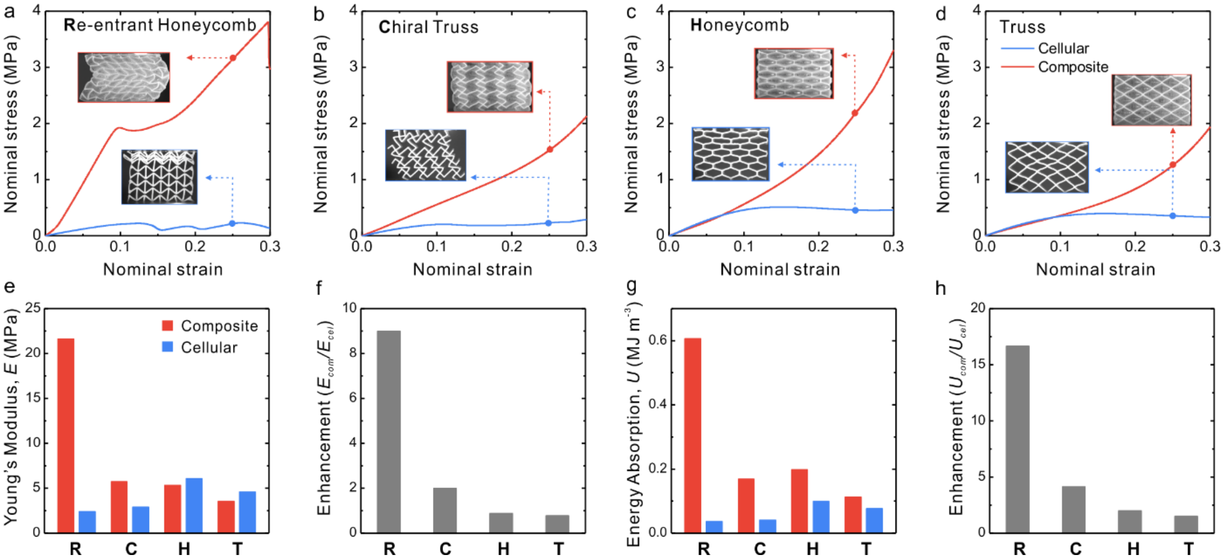

Figure 6.6 The comparison of mechanical properties for the lattice reinforced composites and the lattice counterpart structures are shown. The uniaxial compressive stress-strain curves for (a) the re-entrant honeycomb, (b) the chiral truss, (c) the regular honeycomb and (d) the truss lattices for reinforced composites and the corresponding cellular structures, respectively. For each structure, the deformation images of the composite and its counterpart cellular at the compressive strain of 0.25 are shown. (e) Calculated Young's modulus and (g) the estimated energy absorption for each

specimen. The relative enhancement of (f) Young's modulus and (h) energy absorption of the reinforced composites to their cellular lattice counterparts.

To further understand this, finite element simulations are performed on the four types of lattice reinforced composites and the corresponding lattice cellular structures, as shown in Figure 6.7. It is clearly noticed that the elastomer phase in the auxetic reinforced composites contributes more significantly to the stress response (and hence enhance the stiffness) than that of the non-auxetic reinforced composites (Figure 6.7 (a)). The stress level in the elastomer phase in the non-auxetic reinforced composites is much lower, indicating the little contribution of the matrix phase in the load resistance. However, in auxetic reinforced composites, elastomer phase can suppress the bending and rotation of the glassy polymer ligaments, making them more difficult to deform. Furthermore, when comparing the stress contour of lattice structures in the composites and the cellular, we clearly find the difference between the auxetic structures and the non-auxetic structures (see Figure 6.7 (b) and 6.7 (c)). In auxetic composites, the ligaments exhibit larger stress comparing with those in auxetic cellular, indicating the contribution of them to resist compression loading. In non-auxetic composites, the ligaments show almost the same stress level as those in their counterpart cellular, indicating the deformation mechanism for non-auxetic lattice is almost the same both in the composites and cellular. Therefore, the mutual constraints between two phases of the auxetic lattice reinforced composites enable enhanced stress contours by additional support of the matrix phase and the enhanced resistance of the lattice phase. These results suggest the possibility to tailor the auxetic lattices as reinforcement phase in a composite to achieve enhanced mechanical properties.

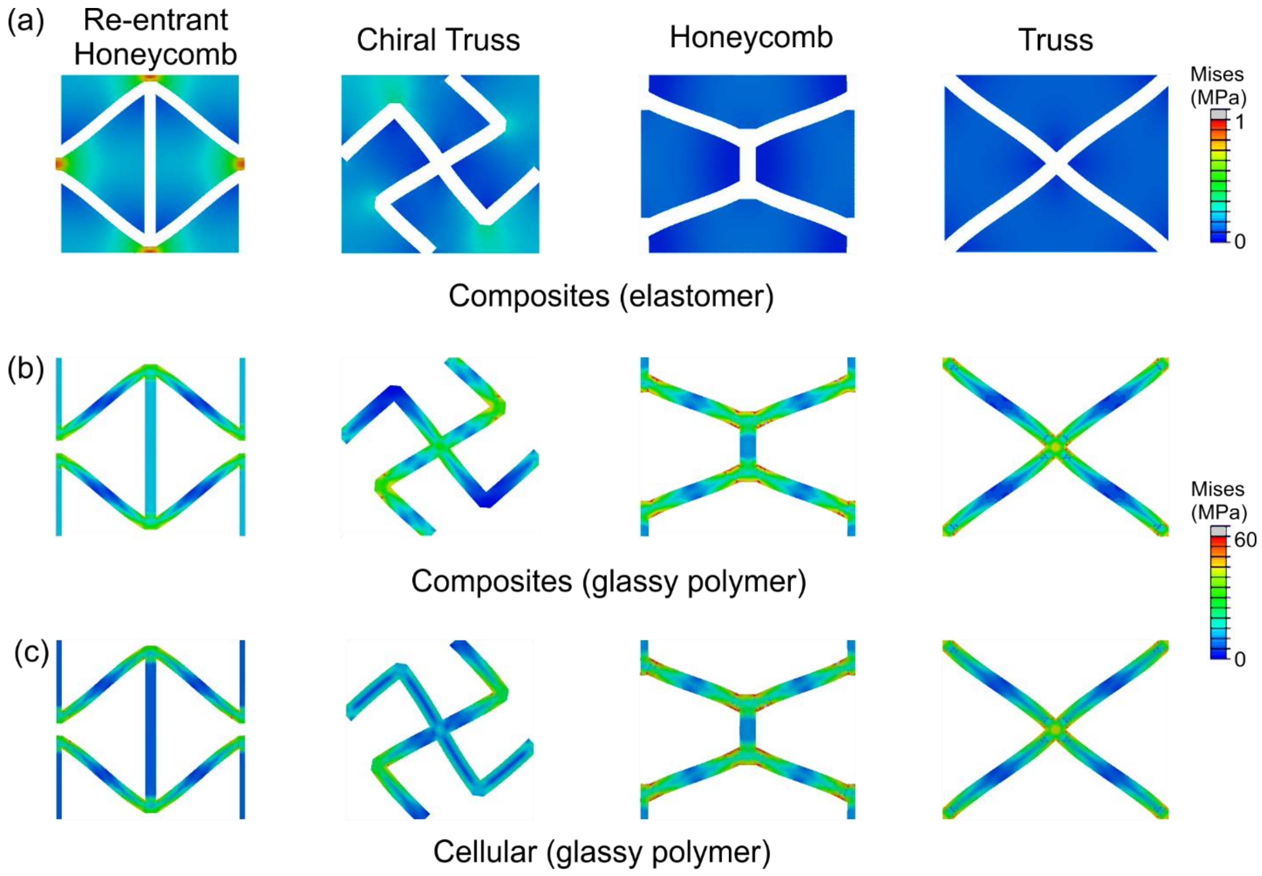

Figure 6.7 The von Mises stress distribution in the lattice reinforced composites and the corresponding cellular structures at a nominal compressive strain of 0.05. (a) The von Mises stress distribution in elastomer phase and (b) the reinforcing phase of glassy polymer in reinforced composites. (c) The von Mises stress distribution in the cellular counterparts of a glassy polymer.

6.3.3 Effect of negative Poisson's ratio

We have demonstrated that the auxetic lattice reinforced composites exhibit enhanced mechanical properties such as stiffness and energy absorption capability compared with non-auxetic lattice reinforced composites. These improved mechanical properties are attributed to the rational structural design of lattice reinforcement combined with the material selections for the reinforcement and matrix phases. In particular, the negative Poisson's ratio in the auxetic reinforcements is crucial to the unusual combination of mechanical performance. To quantitatively understand the effect of Poisson's ratio on the other mechanical properties such as the stiffness and toughness of the lattice reinforced composites, we experimentally explore the response upon compressive tests of the composites reinforced by honeycombs with different Poisson's ratios achieved by varying lattice structure designs. Here we use the same unit cell size as $h = l = 10$ mm, as shown in Figure 6.8 (a). By assuming the value of Poisson's ratio of each cellular structure as ν_{yx}, we calculate that $\theta = \arctan(\nu_{yx} l / h)$, $H = (h - l \tan\theta) / 2$ and $L = l / 2\cos\theta$, based on Gibson's model [61,216]. Here, the volume fraction of honeycomb reinforcement phase is 20% for each design for a fair comparison. The results reported in Figure 6.8 (b) indicate that the enhanced mechanical properties are achieved in the presence of the honeycomb designs with the negative Poisson's ratios. Figure 6.8 (c) shows the corresponding design of honeycomb reinforced composites with Poisson's ratio from -0.9 to 1. Note that when the Poisson's ratio of the composites is zero or positive, the nominal stress-strain curves show a rubber-like hyperelastic behavior; when the Poisson's ratio of the composites is negative, a peak force is observed in the nominal stress-strain curves because the instability occurs in the composites with negative Poisson's ratios. Moreover, the calculated Young's modulus for each composite shows that the honeycomb reinforced composites with lower Poisson's ratios exhibit higher Young's modulus, as shown in Figure 6.8 (d). For example, the Young's modulus of the composite with a Poisson's ratio of -0.9 is 10 times larger than that of the composite with a Poisson's ratio of 1. Furthermore, the energy absorption at a strain of 0.25 for each composite shows that the honeycomb reinforced composites with negative Poisson's ratios have better energy absorption than the honeycomb reinforced composites with positive Poisson's ratios (Figure 6.8 (e)). Differently, the composite with a Poisson's ratio of -0.2 exhibits the largest energy absorption capability. This is because the composites with Poisson's ratios smaller than -0.2 have instabilities in earlier strain region and it results in smaller peak stress, leading to lower energy absorption capability. Finally, it is clear that the composites with auxetic reinforcement phase exhibit enhanced mechanical properties comparing to the composites with non-auxetic reinforcement phase. These results offer a complete picture of the effect of Poisson’s ratio on the mechanical response of the lattice reinforced composites.

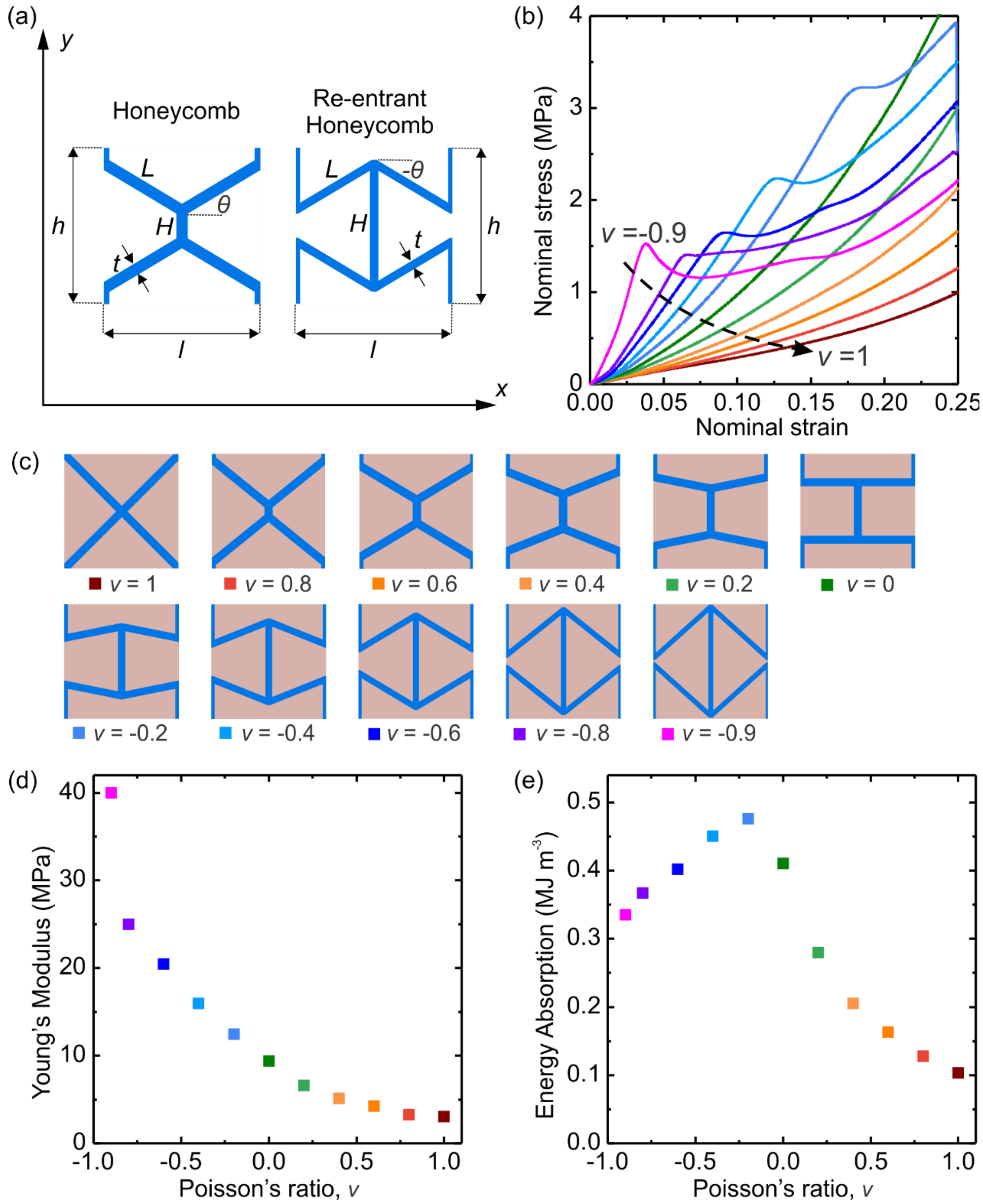

Figure 6.8 Effect of Poisson's ratio on the mechanical properties of various honeycomb reinforced composites during the uniaxial compression test. (a) The unit cell geometry and the coordinate system used for regular honeycomb and re-entrant honeycomb. Here, *h* and *l* are the unit cell lengths; *H* is the length of the vertical cell wall and *L* is the length of the inclined cell wall; *t* is the thickness

of the cell walls; θ is the angle and for re-entrant honeycomb, the value is negative. (b) The nominal stress-strain curves. (c) The geometry design for honeycomb reinforced composites with different Poisson's ratio of the reinforcement honeycombs. (d) Calculated Young's modulus and (e) the estimated energy absorption as a function of the Poisson's ratio of the reinforcement honeycombs.

6.3.4 Effect of volume fraction

While the results reported in Figs. 6.3-6.8 are all for composites with the volume fraction of the reinforcement phase as 20%, further tunability can be achieved by altering the volume fraction of the reinforcement phase. Figure 6.9 presents the experimental results on the stress-strain response of the four lattice reinforced composites at five different volume fractions from 10% to 50%. The stress-strain curves show an increase in the overall mechanical properties as the volume fraction increases. The results indicate that the auxetic reinforced composites, including the re-entrant honeycomb and the chiral lattice reinforced composites, show clear higher stress level over the non-auxetic reinforced composites from low to high volume fraction of the reinforcement phase. Moreover, when the volume fraction of the reinforcement phase is increased, all the stress-strain curves have a transition from a rubber-like hyperelastic behavior to a highly nonlinear behavior followed by brittle fracture of the reinforced composites. This is because the slenderness ratio of ligaments increases with the increase of the volume fraction of the reinforcement phase, making the reinforcement lattices more brittle. Therefore, continuous loading leads to the local catastrophic failure, resulting in a dramatic drop in the stress-strain curves.

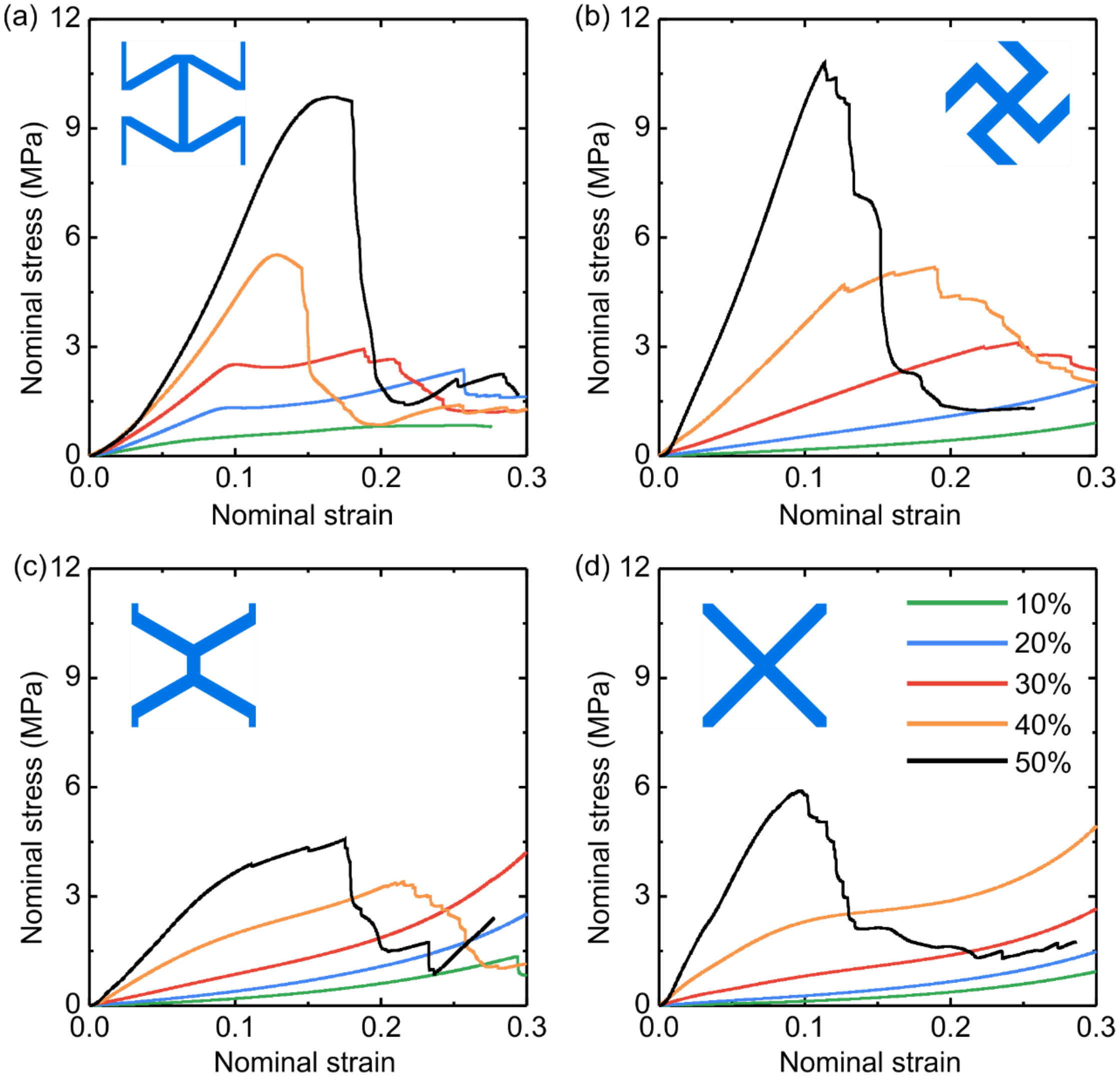

Figure 6.9 The stress-strain responses of four types of composites at different volume fractions of the reinforcing phase. (a) Re-entrant honeycomb reinforced composites, (b) chiral truss reinforced composites, (c) regular honeycomb reinforced composites, and (d) truss reinforced composites.

The Young's modulus and energy absorption at a strain of 0.25 calculated from the stress-strain responses are plotted versus the volume fraction of the reinforcement phase in Figure 6.10. The re-entrant honeycomb reinforced composite has the highest Young's modulus and energy absorption capability comparing to the other three composites, especially at low volume fraction (below 40%) of the reinforcement phase. The chiral lattice reinforced composite is the second best performing composites in general for overall mechanical properties. The non-auxetic lattice reinforced composites exhibit relative weak mechanical properties comparing to auxetic lattice reinforced composites. Generally, the Young's modulus of the cellular materials, such as metal foams and lattice structures, can be described by a scaling law between the mechanical property and the relative density [61,218]. Since the mechanical property of lattice reinforced composites is dominated by the reinforcement phase, we use a scaling law to describe the response of these composites in this study. For the Young's modulus, E_c of the composite can be described as a function of the modulus of material for reinforcement phase, E_r and the volume fraction of the reinforcement phase, V_r / V_c, via $E_c = C_1 E_r (V_r / V_c)^n$ where C_1 and n can be obtained by fitting the experimental data. Similar relation for energy absorption, U_c is $U_c = C_2 U_r (V_r / V_c)^m$ where U_r is the energy absorption of the bulk material of the reinforcement phase at the same strain level, presented in Table 6.1; C_2 and m can be obtained by fitting the experimental data. The parameters C_1, C_2, n and m are listed in Table 6.2. The scaling exponent close to 1 indicates a stretch-dominated deformation behavior whereas an exponent of 2 typically indicates bending-dominated deformation. It is also established that structures governed by a stretching-dominated deformation offer higher stiffness and strength per unit weight than those governed by bending-dominated deformation. In our lattice reinforced composites, the scaling exponent for re-entrant honeycomb reinforced composites are found to be $n = 1.369$ and $m = 1.174$. While for the other composites, the scaling exponents are larger or close to 2. These results indicate that the re-entrant honeycomb reinforced composites are close to stretch-dominated deformation in overall while the other composites are close to bending-dominated during uniaxial compressive loading. Moreover, this trend can be noticed in the local analyses of the composites (Figure 6.7). We can notice that in honeycomb and truss composites, the matrix has neglectable effects on the deformation mechanism of lattice structures. We believe that the deformation mechanisms of non-auxetic composites and cellular are more bending-dominated. However, in re-entrant and chiral truss composites, the matrix provides additional support and suppresses the bending and rotation of the ligaments of lattice structures, making them more difficult to deform, changing the deformation mechanism to more stretching-dominated. As a result, the deformation mechanism significantly affects the mechanical response of the lattice reinforced composites. This nearly linear scaling relation of the re-entrant honeycomb reinforced composites indicates that we can design light weight yet stronger composites. These results suggest great potentials to tailor the geometric features of the lattice reinforced composites to achieve tunable mechanical properties.

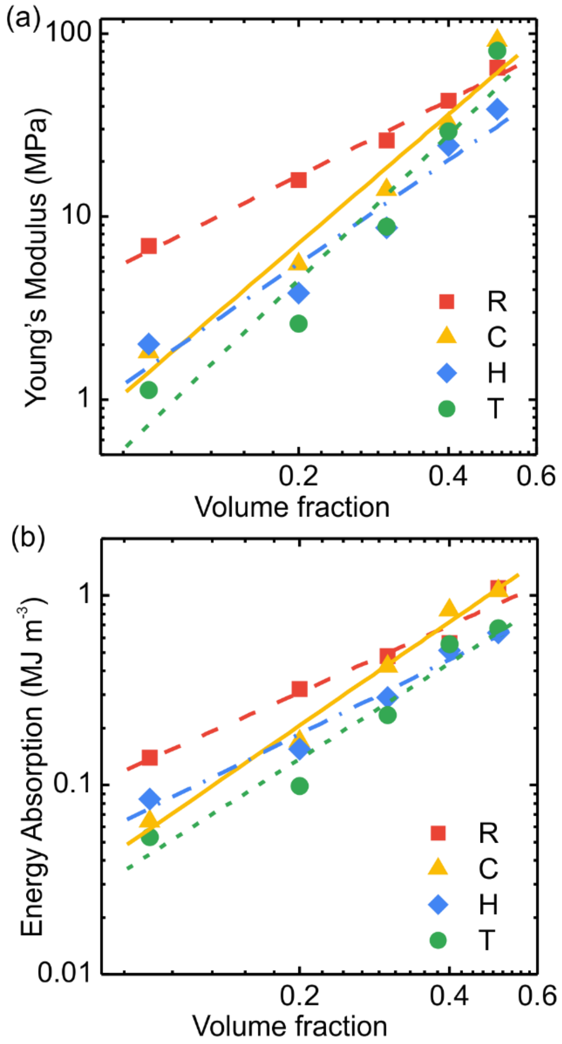

Figure 6.10 Comparison of mechanical properties of the lattice reinforced composites as a function of the volume fraction of reinforcement phase: (a) Young's modulus, (b) energy absorption.

Table 6.2 The relations of the Young's modulus and energy absorption at a strain of 0.25 to the volume fraction of the reinforcement phase for the lattice reinforced composites.

Lattice reinforced composites	Young's modulus		Energy absorption	
	C_1	n	C_2	m
Re-entrant composite	0.100	1.369	0.186	1.174

Chiral composite	0.204	2.340	0.349	1.817
Honeycomb composite	0.075	1.877	0.138	1.303
Truss composite	0.206	2.630	0.186	1.676

6.3.5 Discussion

In the previous sections, we focus on the 2D lattice structures and demonstrate that 2D auxetic lattice reinforced composites exhibit enhanced mechanical properties. Recently, 3D auxetic systems consisting of networks of buckliball [13], chiral-like structures [100], orthotropic laminated open-cell frameworks [219], and lattice metamaterials with curved beams [99,102,220] have been designed. Indeed, most of these 3D auxetic structures are porous thus are very suitable to serve as reinforcements in composites. Conceptually, under uniaxial compression, the soft matrix will be in a state of triaxial compression, thereby leveraging the overall mechanical performance of the composites [174,221,222].

In this study, we focus on demonstrating the effect of geometric features of auxetic reinforcements on the mechanical behaviors of the designed composites, however, the selection of materials for each phase of composites is still an important issue. Due to the limitation of our 3D printer, we use the glassy polymer as the reinforcement phase and a rubber-like material as the matrix. Recently, additive manufacturing enables the fabrication of not only polymeric but also metallic and ceramic materials with intricate cellular architectures [14]. Cellular materials, such as lattice structures, can easily be fabricated by metal powder bed fusion [223,224]. Although given the high melting point of ceramics, a few 3D printing systems could print ceramics either by selective curing of a photosensitive resin that contains ceramic particles, by binder jetting or by selective fusion of a powder bed with a laser [225,226]. Moreover, post-pyrolysis of 3D printed polymer precursors can fabricate carbon [64,227] or ceramic materials [228] with architected structures. Therefore, as new methods are emerging and maturing, fabrication of more and more complex cellular architectures especially auxetic structures will be enabled. Such development will facilitate fabricating auxetic reinforced composites with various materials as the reinforcement phase for a wide range of applications and further creating multifunctional materials.

Finally, the dynamic response of the auxetic reinforced composites will be of great interest despite we have studied the quasi-static compressive behaviors here. For example, improved impact resistance has been recently observed in 3D-printed bioinspired composites with hierarchical conch shell structures using the same material systems as ours [229]. Indeed, the dynamic effects including the micro-inertial effect, shock wave effect and strain rate effect of the materials have very significantly influences to the mechanical behaviors of the 3D-printed composites. Especially for the glassy polymer VeroWhite, its yield strength significantly increases as strain rate increases. In the future work, the dynamic behaviors of the auxetic reinforced composites under different levels of strain rates will be systematically investigated.

6.4 Conclusion

In summary, we have investigated the macroscopic mechanical responses of the auxetic lattice reinforced composites through a combination of 3D printing, experiments, and numerical analyses. We have shown that auxetic lattice reinforced composites have enhanced mechanical performance, achieving a unique combination of stiffness and energy absorption, compared with the non-auxetic lattice reinforced composites. In particular, by harnessing the negative Poisson’s ratio effect in the lattice reinforcements, we find that the mutual constraints between the auxetic reinforcement and matrix enable enhanced mechanical properties by gaining additional support from the matrix phase. We further quantify the effect of Poisson’s ratio on the other mechanical properties of various honeycomb reinforced composites, indicating that the degree of auxetic behavior could be used to tune the stiffness and energy absorption of the lattice reinforced composites. Finally, we use scaling law to evaluate the effect of volume fraction of the reinforcement phase in the composites, showing that the re-entrant honeycomb reinforced composite exhibit nearly linear scaling. These results provide guidelines for engineering and developing a new class of auxetic reinforced composites with enhanced mechanical performance for a wide range of applications and further creating multifunctional materials.

Chapter 7. The fracture behavior of Interpenetration Phase Composites

7.1 Introduction

Structural systems in the defense, aerospace, automotive, energy, and semiconductor industries are often under complex loading conditions, such as multi-axial loading, vibration, shock, and, high-velocity impact. This triggers the demands for the development of innovative structural materials, possessing a compelling combination of mechanical robustness, lightweight, affordability, and versatility. Composite materials consisting of multiple compositions can have improved overall performance due to the synergistical contribution of each composition in the composites. Among these composites, interpenetrating phase composite (IPC, also known as co-continuous composite), in which each constituent phase forms a completely interconnected three-dimensional (3D) network, has attracted a lot of research interests. [230-233] Indeed, the interpenetrating microstructures are widely spread in biological structural materials, such as sea urchin skeleton, [234] human bone, [235] microvascular networks, [236] and botanical systems. [237] These natural IPCs exhibit rich multifunctionalities including thermal, mechanical, and other transport properties. Intrinsically, these prominent properties are controlled by their inherent architectures. Each constituent phase completely interpenetrates through the composite microstructure in all three dimensions and contributes the maximum of its most desirable properties to the overall properties of the composite, thereby endowing the composite with a more attractive combination of properties and functionalities.

To understand the multifunctionalities observed in the natural IPCs systems, considerable efforts have been recently devoted to developing analytical models and computational frameworks to evaluate the effective thermal and mechanical performance of synthesized IPCs. For example, analytical methods based mainly on Voigt and Reuss models can accurately predict the effective thermal and mechanical properties of the IPC. [237-240] Numerical methods such as finite element modeling have been extensively employed to capture the elastic, thermal, dynamic, and fracture properties of IPCs. [22,64,175,221,241-247] It should be pointed out that most of these IPCs are fabricated using conventional methods, such as squeeze casting process and pressureless melt infiltration, [248,249] where each phase is randomly distributed. Though the volume fraction can be precisely controlled, the inherent architecture is still ill-defined. For example, the dimensions of the ligaments have a nonuniform feature and each composition is randomly dispersed, which poses a great challenge to fabricate IPCs with fewer defects and accurately predict their effective properties.

Recently, studies show that materials with well-defined architectures could be exploited to explore new properties and novel functionalities. [14,160,250-255] Along with this, advanced additive manufacturing techniques, such as 3D printing, have gained much attention due to its capability of creating complex topologies with fine features composed of a multitude of materials with varying mechanical properties quickly, cheaply, and at a large scale. [211,255-262] For example, improved impact resistance has been observed in 3D printed bioinspired composites with hierarchical conch shell structures, indicating a crack-arresting mechanism embedded in the natural architecture. [263] As reported in our previous work, the 3D periodic IPCs based on the triply periodic minimal surfaces (TPMS) of glassy polymer/rubbery polymer materials at micrometer resolutions can be readily fabricated through 3D printing. [241] A combination of high stiffness, strength, energy absorption, and damage tolerance have been achieved in the 3D printed IPCs with different lattice symmetries. More recently, more TPMS topologies are used to design IPCs and their compressive properties and electrical conductivities [264] are experimentally tested [261,262,265] and numerically analyzed [266,267]. However, a quantitative understanding of the fracture behavior of architected IPCs is still lacking and especially the measurement of the fracture toughness of such complex materials is less well defined.

In this paper, we investigate the fracture toughness of a group of 3D printed IPCs with different lattice symmetries. Three-point bending tests are performed on the singled edge notch bend (SENB) samples to quantify the fracture properties. The results are compared with conventional composites with particle reinforced, fiber reinforced, and laminates topologies. Furthermore, we demonstrate that the fracture toughness of the proposed IPCs can be tuned through controlling the stiffness contrast of the compositions and printing directions.

7.2 Design and fabrication of Interpenetration Phase Composites

The specimens are fabricated using an Objet Connex260 multi-material 3D printer (Stratasys) which allows the simultaneous printing of two different materials. The specimens for compression tests consist of 4 × 4 × 4 unit cells, resulting in prototype dimensions of 10 mm × 10 mm × 10 mm. The specimens for the fracture toughness measurement are shown in Figure 7.1 (d), which consist of 54 × 12 × 6 unit cells resulting in a dimension of 135 mm × 30 mm × 15 mm. The unit cell dimensions of the specimens for compression tests and 3-point bending tests are both 2.5 mm × 2.5 mm × 2.5 mm. The dogbone specimens for glassy polymer (material *A*, *B4, B5*) and the dogbone specimens for rubber-like polymer (material *B1*, *B2*, *B3* and *B*) are fabricated according to the ASTM D638 and the ASTM 412, respectively. The minimum geometric size of inner structures in the crystalline composites is around 200 μm, which is at least one order of magnitude greater than the minimum resolution (16 μm) provided by the 3D printer. Considering the anisotropic nature of 3D printing, the layer orientation is found to influence the mechanical properties of the material; therefore, all the specimens are printed along the same orientation. The as-fabricated specimens are kept at room temperature for 7 days to allow for the saturation of the curing.

The model system of IPCs studied here is based on microstructures which combine the rod-connected lattices and their inverse counterparts. Here three lattice symmetries are considered including simple-cubic (SC), body-centered-cubic (BCC), and face-centered-cubic (FCC) lattices. Figure 7.1 (a-c) displays the proposed 3D periodic SC, BCC, and FCC IPCs where the volume fraction of each phase is set to 50%. In our design, the phase of rod-connected lattices is set as the hard domain and the inversed phase is set as the soft domain. Compared to previous IPCs with triply periodic minimal surfaces, [241] these IPCs with rod-connected counterparts are easier for design with simple geometric parameters and unit cells. The symmetry and volume distribution in these structures can be precisely controlled by tailoring the radius of rod ligaments. The relations between the volume fraction of rod-connected lattices' domain, $\overline{\rho}$ and the radius/periodicity ratio, *r/l* are given by:

$$\overline{\rho} = 3\pi(\frac{r}{l})^2 - C_1(\frac{r}{l})^3 \text{ for SC,} \tag{7.1}$$

$$\overline{\rho} = 4\sqrt{3}\pi(\frac{r}{l})^2 - C_2(\frac{r}{l})^3 \text{ for BCC,} \tag{7.2}$$

$$\overline{\rho} = 12\sqrt{2}\pi(\frac{r}{l})^2 - C_3(\frac{r}{l})^3 \text{ for FCC,} \tag{7.3}$$

where the radius of the rod ligaments is r and the length of the unit cell is l. The cubic correction coefficients $C_1 = 11.318$, $C_2 = 39.201$ and $C_3 = 154.518$ have been identified from fitting Eqs. (7.1)- (7.3) to CAD calculations. [268]

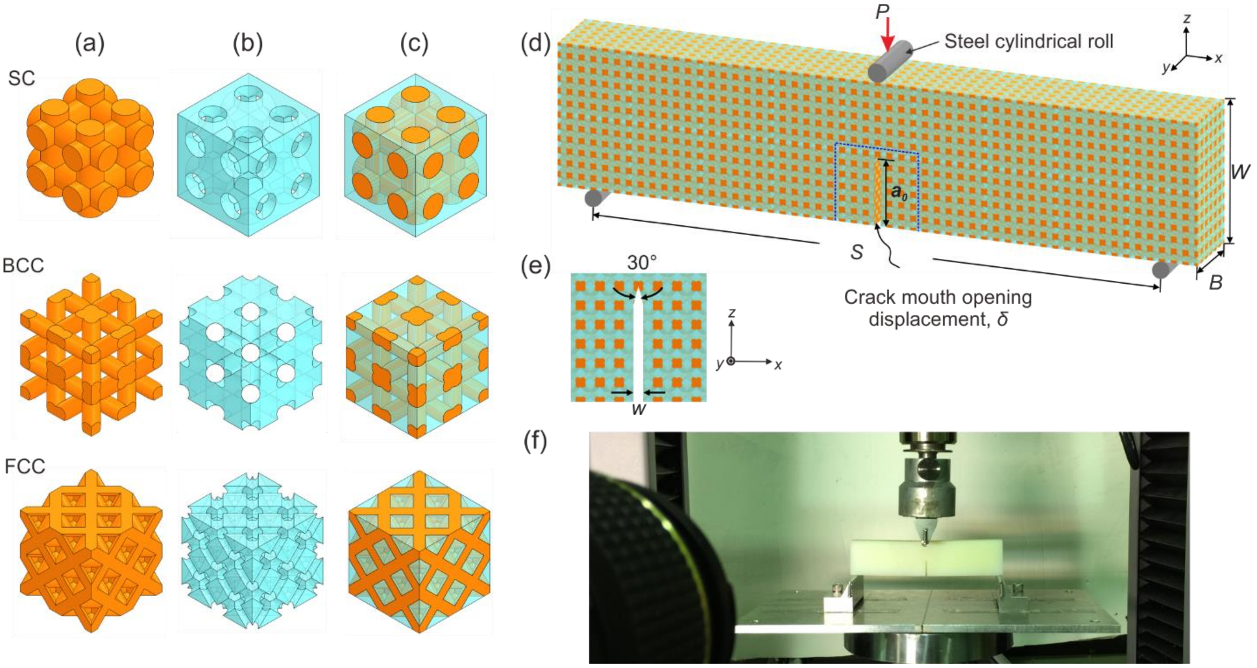

Figure 7.1 Schematics of 3D IPCs with different lattice symmetries. (a) 3D periodic interpenetrating phase composites (IPCs) consisting of 2×2×2 representative volume elements with simple cubic, body-centered-cubic l, and face-centered-cubic lattice symmetries. (b) The corresponding phase of rod-connected counterpart in each IPC . (c) The corresponding inverse phase in each IPC. Experimental setup for the 3-point bending test. (d) Single edge notched bend (SENB) specimen and test configuration. The dimensions of the specimen are defined as the width *W*, the length *L* and the thickness *B*. The load *P* is applied in the mid of specimens and the span length is *S*. The initial length of the notch is defined as a_0. (e) The crack starter notch, where the width of the notch is defined as *w* and the angle of the initial crack tip is 30°. (f) The experiment setup of 3-point bending test of SENB specimen.

In addition to the IPCs, the particle-reinforced composites (PCs), the fiber-reinforced composites (FCs) and the laminal-reinforced composites (LCs) are also designed and fabricated with the same amount of compositions to compare the fracture toughness.

The specimens for uniaxial compression and three-point bending tests are fabricated using a multi-material 3D printer (Objet Connex260, Stratasys) and multiple photocurable prepolymers are used to form the hard and soft components (See Experimental section for more details). In this work, VeroWhitePlus, a glassy polymer, is used for the hard domains (labeled "*A*") and TangoPlus, which is highly rubbery, is used for the soft domains (labeled "*B*"). The stiffness contrast between these two phases can be tailored by mixing VeroWhitePlus and TangoPlus via a digital material mode in the printer. The mixed materials are used for the hard component (labeled as "*B*1", "*B*2", "*B*3", "B4" and "*B*5").

7.3 Experiment section

In order to evaluate the mechanical properties of the constitutive materials, the uniaxial tensile tests are performed using the same MTS mechanical tester with a 10 kN load cell. All the experiments are conducted in a quasi-static regime with a constant strain rate of 0.001 s^{-1}. Each tensile test is repeated for three replicates. The tensile specimens are tested under displacement controlled until failure. Using the data from uniaxial tension tests, the stiffness of each constituent materials under tension can be calculated. The uniaxial compression tests for IPC cubic specimens are performed using a MTS mechanical tester (C43 frame) with a 10 kN load cell. All the experiments are conducted in a quasi-static regime with a constant strain rate of 0.001 s^{-1}. The load-displacement curves measured from the uniaxial compression tests are then transferred into nominal stress-strain behaviors based on the measured dimensions of the specimens. Young's modulus E_{XX} and yield stress σ_{XX} for each specimen are calculated from the nominal stress-strain curves. For each data point, three specimens have been tested and the average value is reported. Images of the specimens at various loading conditions are taken at a rate of 1 FPS (VicSnap, Correlated Solution). For fracture toughness measurement, three-point bending tests are performed with the same mechanical tester at a constant displacement rate of 0.5 mm/min. Images of the specimens at various loading conditions are taken at a rate of 0.08 FPS. The *J*-approach was employed to capture inelastic contributions to the fracture resistance using the elastic compliance method in ASTM E1820. Compliance measurements from the unloading curves were made at intervals Δv = 0.25, 1 and 1 mm for the SC, BCC and FCC IPC samples, respectively. Calculation of the current crack length used the compliance along the loading line, and the *J*-approach was calculated using the measured applied load and crack mouth opening displacement, δ. The fracture toughness, $K_{J(i)}$, is related to the *J*-approach by $K_{J(i)} = (J_{(i)}E')^{1/2}$, where ν is the plain strain Young's modulus, $E' = E_S / (1-\nu^2)$ and ν is the Poisson's ratio. Since the samples were composites and not homogeneous solid materials, this study used the measured compressive moduli along the span length, E_{XX}, which are tabulated in Table 7.1

The *J*-integral approach outlined in ASTM E1820, 2013 is employed to evaluate the fracture toughness. At a point corresponding to *v* and *P* on the specimen force versus displacement record, the *J*-integral is calculated at the onset of every unloading cycle (given by the index *i*) performed in the loading regime. The value of *J* at an instant (*i*) in the loading regime is then given by the summation of an elastic component, J_{el}, and a plastic component, J_{pl}, as follows:

$$J_{(i)} = J_{el(i)} + J_{pl(i)} \tag{7.4}$$

The elastic component J_{el} follows from

$$J_{el(i)} = K_{(i)}^2 / E_{XX} \tag{7.5}$$

where the E_{XX} is the measured value of Young's modulus in the *X* direction. The value of $K_{(i)}$ at each unloading event is given as

$$K_{(i)} = \left[\frac{P_i S}{BW^{3/2}} \right] f(a_i / W) \tag{7.6}$$

where the geometrical parameters *S*, *B*, and *W* are defined in Figure 7.1 (d). The calibration factor $f(a_i / W)$ is given by

$$f(a_i / W) = 3\left(\frac{a_i}{W}\right)^{1/2} \frac{[1.99 - \left(\frac{a_i}{W}\right)\left(1 - \frac{a_i}{W}\right)(2.15 - 3.93\frac{a_i}{W} + 2.7\left(\frac{a_i}{W}\right)^2]}{2(1 + 2\frac{a_i}{W})(1 - \frac{a_i}{W})^{3/2}} \tag{7.7}$$

where $a_{(i)}$ is the current crack length. This crack length is estimated using the relation

$$a_{(i)} = W(0.999748 - 3.9504u + 2.9821u^2 - 3.21408u^3 + 51.51564u^4 - 113.031u^5) \tag{7.8}$$

where the factor *u* is related to the compliance via

$$u = 1/[(\frac{BWE_{XX}C_{\delta(i)}}{S/4})^{1/2} + 1] \tag{7.9}$$

where $C_{\delta(i)} = (\frac{d\delta}{dP})_{(i)}$ is the compliance estimated from the crack mouth opening displacement at the onset of unloading.

The plastic component of *J* is estimated using the deformation *J* definition via

$$J_{pl(i)} = \left[J_{pl(i-1)} + \left(\frac{\eta_{pl}}{b_{(i-1)}}\right)\left(\frac{A_{pl(i)} - A_{pl(i-1)}}{B}\right)\right]\left[1 - \gamma_{pl}(\frac{a_{(i)} - a_{(i-1)}}{b_{(i-1)}}\right] \tag{7.10}$$

where $\eta_{pl} = 1.9$, $\gamma_{pl} = 0.9$ based on the Eq. A1.8 in ASTM E1820, $b_{(i-1)}$ is the length of the uncracked ligament at the previous unloading event via $b_{(i-1)} = B - a_{(i-1)}$. $A_{pl(i)}$ is the area under the plastic load versus load-line displacement measurement. We estimate $A_{pl(i)}$ using

$$A_{pl(i)} = A_{pl(i-1)} + (P_{(i)} + P_{(i-1)})(v_{pl(i)} - v_{pl(i-1)}) / 2 \tag{7.11}$$

where $v_{pl(i)} = v_{(i)} - \left(P_{(i)} C_{v(i)}\right)$ is the plastic part of the load-line displacement and $C_{v(i)} = \left(\frac{dv}{dP}\right)_{(i)}$ is the experimental compliance corresponding to the current crack length, $a_{(i)}$.

The fracture toughness at the unloading instant (i), $K_{J(i)}$, is then calculated from the *J*-integral using the relation $K_{J(i)} = (J_{(i)} E_{XX})^{1/2}$.

7.4 Compression behavior of Interpenetration Phase Composites

Indeed, the IPC structures have been previously studied numerically for their compressive mechanical properties. [269] The meshfree radial point interpolation method and unit cell-based finite element (FE) models are used to evaluate the elastic properties of 3D printed IPCs Here, we experimentally studied the compressive behavior including elastic, plastic deformation and failure mechanism. Figure 7.2 presents the comparison of mechanical response between IPCs and PCs under uniaxial compression. The stress-strain curves for IPCs exhibit initial linear elasticity, followed by yield and post-yield strain hardening (Figure 7.2 (a)). However, the stress-strain curves for PCs exhibit initial linear elasticity and maximum stress followed by failure (Figure 7.2 (b)). Noticeably, IPCs exhibit higher stress level compared to those of PCs. We could envision that in IPCs, more volume of hard material is utilized to contribute to the stress level of stress-strain curves. As shown in our previous work, [64,221,241] this is because the continuous interfaces are beneficial to the load transfer between the glassy polymer and the rubbery polymer. It is clearly noticed that the stress-strain relations of our IPCs consisting of glassy polymer and elastomer are different from the J-shape stress-strain relations of the IPCs with two elastomer. [246] While these soft crystals IPCs also revealed that the topological connectivity of dissimilar domains is of critical importance for tailoring the macroscopic mechanical properties and the mechanical anisotropy. Images of compressive deformation for FCC lattice IPC and FCC lattice of PC are shown in Figure 7.2 (c) and (d), respectively. Cracking is observed in the interior of glassy polymer domain rather than at an interface between the phases in FCC lattice IPCs. The co-continuity of the structure constrains the cracking and enables these composites to provide energy absorption to larger strains before catastrophic failure. By contrast, the catastrophic failure could be observed in the matrix phase of the FCC lattice PC. These structures exhibit failure at small strain with relatively low stress because of the discontinuous phase of glassy polymer which limits the load capacity and generates the stress concentration on the matrix phases.

Table 7.1 The measured in-plane Young's modulus, E_{XX} , in-plane compressive yield stress, σ_{XX}

Sample	Design	V.F. (A)	Material	E_{XX} (MPa)	σ_{XX} (MPa)
1	IPC-SC	50%	A/B	369.34	20.61
2	IPC-BCC	50%	A/B	137.09	10.03
3	IPC-FCC	50%	A/B	190.00	10.70
4	IPC-FCC	40%	A/B	65.88	4.04
5	IPC-FCC	30%	A/B	44.15	2.48
6	IPC-FCC	20%	A/B	19.23	0.98
7	IPC-FCC	50%	A/B1	305.27	N/A
8	IPC-FCC	50%	A/B2	349.90	N/A

9	IPC-FCC	50%	A/B3	430.22	N/A
10	IPC-FCC	50%	A/B4	567.14	N/A
11	IPC-FCC	50%	A/B5	644.64	N/A
12	PC-SC	50%	A/B	42.21	8.16
13	PC-BCC	50%	A/B	4.94	7.02
14	PC-FCC	50%	A/B	5.03	10.30
15	FC-0°	50%	A/B	78.22	2.80
16	FC-90°	50%	A/B	15.30	2.85
17	LC-0°	50%	A/B	14.55	5.95
18	LC-90°	50%	A/B	35.76	5.39

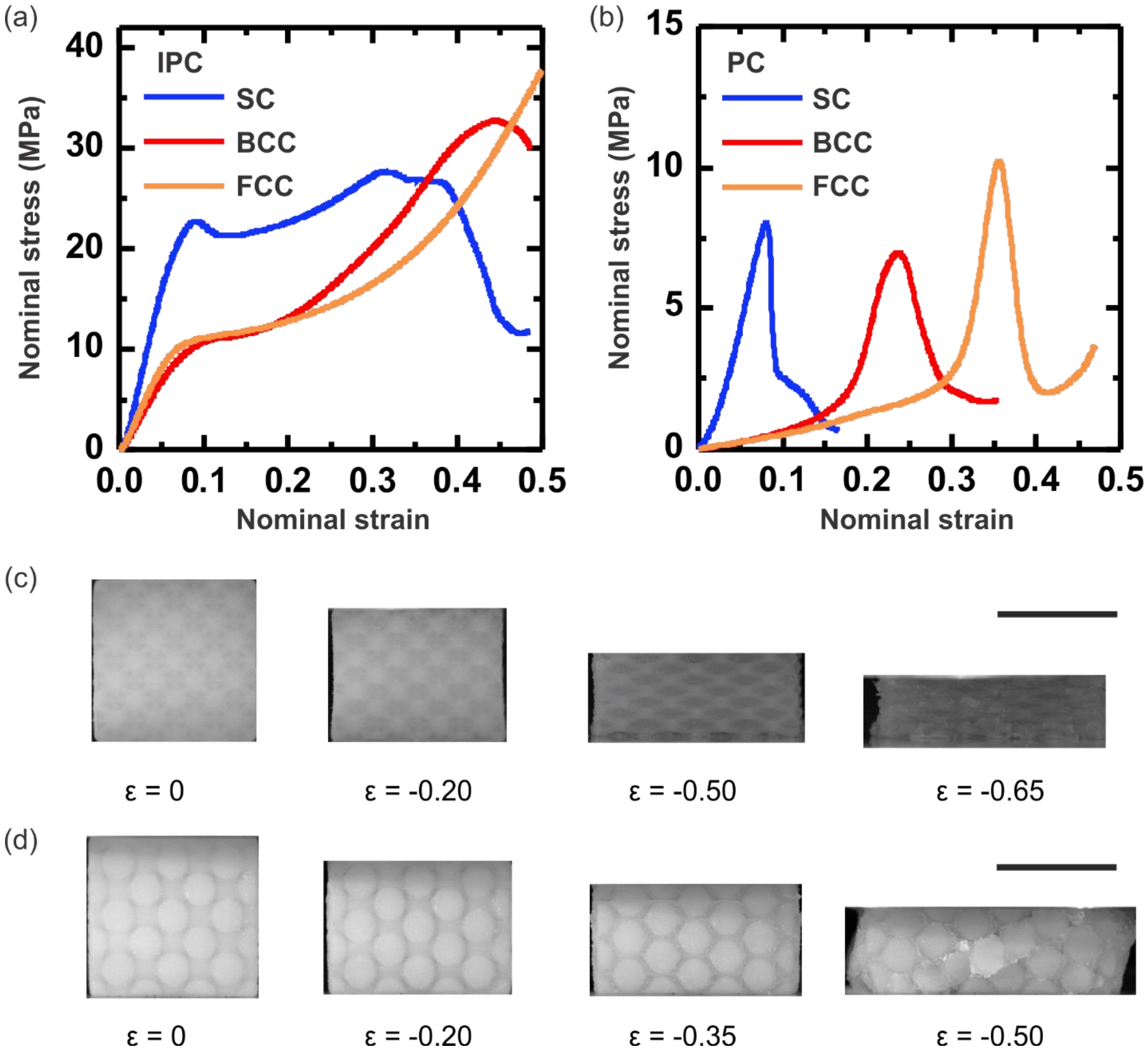

Figure 7.2 Mechanical response of 3D printed composites during uniaxial compression tests. (a) Nominal stress and strain curves for (a) IPCs with SC, BCC and FCC lattice structures and (b) PCs with SC, BCC, and FCC lattice symmetries under uniaxial compress tests. Experimental images of (c) IPC with FCC lattice symmetry and (d) PC with FCC lattice symmetry. Scale bar: 1 cm.

7.5 Fracture toughness measurements

7.5.1 Fracture behavior and mechanisms of IPCs

The fracture toughness is determined using a singled edge notch bend (SENB) sample following the procedure outlined in ASTM standard E1820 (ASTM E1820, 2013), as shown in Figure 7.1 (d)-(f). The overall dimensions of the samples defined by ASTM standard E1820 are 135 mm × 30 mm × 15 mm ($S \times L \times B$) unless specified elsewhere (Figure 7.1 (d)). It comprises of 45 representative volume elements (RVEs) repeated along the X direction and 12 RVEs repeated along the Y direction. The two outer steel rollers defined the span, S, which is adjusted to be four times the sample width, W, as specified in standard E1820. The third roller is located at the mid-span, opposite the sample notch. The combination of starter notch and fatigue precrack shall conform to the ASTM standard requirements shown in Figure 7.1 (e). A very sharp notch tip with the angle of 30° is designed to promote early crack initiation. Figure 7.1 (f) shows the overall experimental setup of three-point bending test of SENB specimen. The fracture toughness at the failure strain, K_J, could be evaluated from the load-displacement curves measured from the three-point bending tests using the J-integral approach outlined in ASTM E1820, 2013. More details can be found in the Experiment Section.

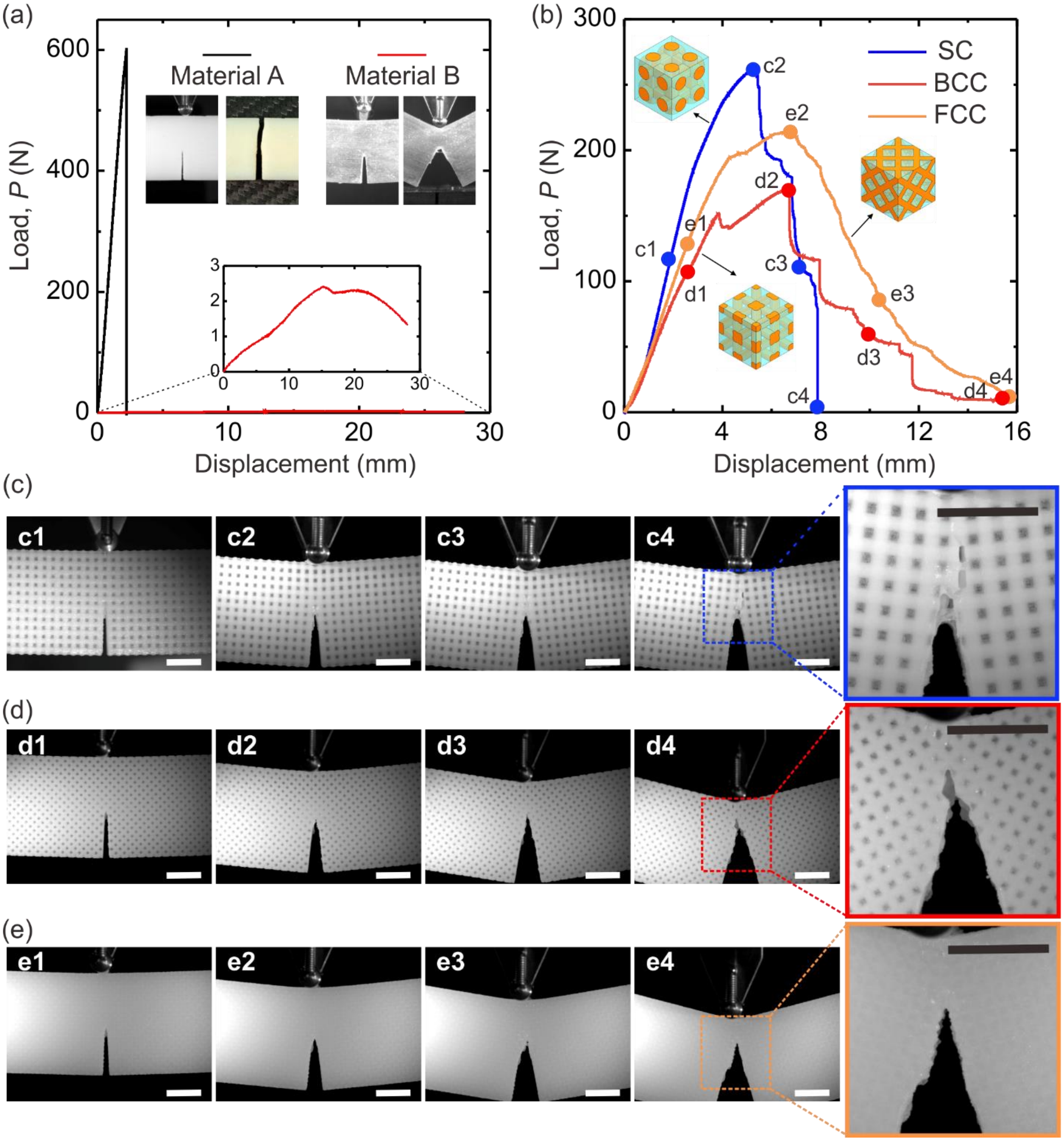

Figure 7.3 3-point bending tests of the SENB specimens. (a) Load-displacement curves of material *A* and material *B*. (b) Load-displacement curves of IPCs with SC, BCC and FCC lattice symmetries. (c)-(e) Images of test specimens at various loading displacements which are marked in the load-displacement curves. Scale bar: 1 cm.

Before systematically examining the fracture behaviors of proposed IPCs, we first investigate the fracture response of the two base materials used for printing the composite geometries, material *A* and material *B* (Figure 7.3 (a)). The load-displacement curves obtained from the three-point bending test of SENB samples clearly show significant distinction between the constitutive behavior of these two materials. From the compression tests we have performed on the 3D printed materials, the results show that the stiffness of material *A* is three orders of magnitude higher than the stiffness of material *B*, by a factor of ≈ 1350. Therefore, the more compliant base material *B* failed at an order of magnitude higher displacement than its less compliant counterpart *A*. Moreover, both samples fail in a brittle manner immediately upon crack propagation.

We now proceed to study the deformation and fracture mechanisms of the designed IPCs. Figure 7.3 (b) plots the load, *P*, as a function of load-line displacement, *v*, for three lattices, SC, BCC, and FCC IPCs. The load-displacement curves for IPCs exhibit initial linear elasticity, non-linear plasticity before the maximum load and the drops in load which are related to the failure of structures. Compared with the fracture behavior of each composition, the IPCs samples show a highly nonlinear behavior. The continuous soft material phase distributes stress and strain effectively throughout the sample, inducing an additional support to generate more plastic deformation instead of the brittleness of the hard material. Therefore, the extrinsic and intrinsic toughening mechanisms of 3D periodic IPCs from inhibiting damage mechanisms include stretching of the hard polymer that bridges the advancing crack and is also associated with plasticity. As a result, it is effective against the initiation and propagation of cracks. Figure 7.3 (c)-(e) presents the in-situ images of the deformed configuration of each IPC at different displacements. Before the first peak load, the large deformation of the material around the precrack tip is visible on the surface of each IPC. After the first peak load, the fracture propagation could be observed. The drops in load after the maximum peak are not continuous but have several steps. This is because the inherent architectures of IPCs play a significant role in preventing the propagation of cracks continuously. Based on the energy principles, the crack will choose the path of least resistance such as in the soft material. However, the structures of 3D periodic IPCs contain continuous hard and soft materials with multiple constrains which will inhibit the crack propagation in only one phase. Furthermore, FCC IPC exhibits smaller load dropping steps due to the more complexity of microstructures compared with SC and BCC IPCs. For the SC IPC, the images clearly portray that the crack path eccentrically is upon the initial crack tip. Similarly, in the BCC and FCC IPCs, evidently the fracture path is the zigzag shape and the lateral surfaces of the crack are very rough. This phenomenon can be explained based on the energy principle that the crack path will result in a trade-off between the minimum crack deflection angle and the path of least stiffness. Moreover, we also observe that the interfacial adhesion of the 3D printed constituent materials is so strong that the composites do not fail at the interfaces. The proposed IPCs exhibit impressive mechanical characteristics activated by the rationally designed interpenetrating architecture.

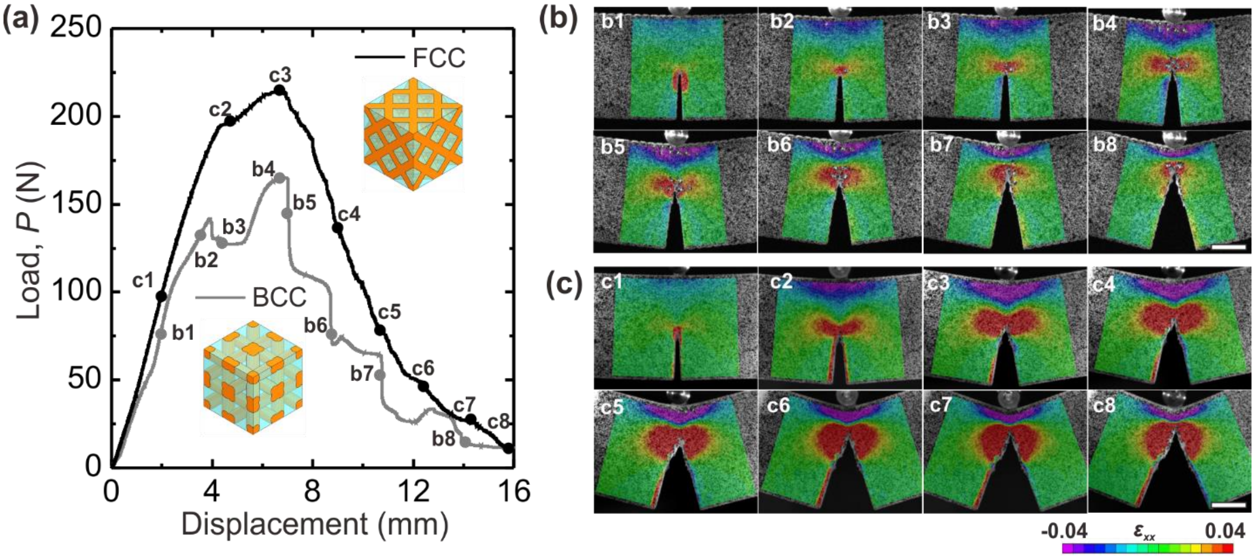

Figure 7.4 3-point bending tests of the SENB specimens of IPC-BCC and IPC-FCC. (a) load-displacement curve. Experimental strain contours of (b) IPC-BCC and (c) IPC-FCC using digital image correlation at various loading displacements which are marked in the load-displacement curves. Scale bars are both 1 cm.

To further understand the fracture behavior of the proposed IPCs, we use Digital Image Correlation (DIC) measurement system to quantitatively understand the deformation and crack propagation of these specimens. Figure 7.4 (a) shows the measured force-displacement relation of three-point bending test and the images in Figure 7.4 (b) and 7.4 (c) exhibit the horizontal strain contours related to the main deformation of the IPC-BCC and IPC-FCC respectively which also reflect the stress distributions during the whole loading process. We notice that in the elastic loading stage, the strain distributes mostly behind the crack tip (b1 and c1). Prior to tip failure, as shown in b2, c2, and c3, the strain concentrates ahead of the crack tip to inhibit damage mechanisms, such as cracking which will toughen the IPCs. After tip failure, we clearly observe that the fracture appears in several positions where the strain distributes around as shown in b3-b6. A similar phenomenon could be visualized in c4-c6. With crack propagating, the strain concentration delocalizes to different directions and form longer crack path as shown in b7-b8 and c7-c8, which will extend the load-displacement curves in Figure 7.4 (a). Therefore, these images clearly portray that the 3D printed IPCs exhibits impressive mechanical characteristics in terms of fracture propagation. The periodic IPC structures toughen the composites with improving the plasticity of the hard material. Moreover, the soft material delocalizes the stress concentration, enabling the crack propagates in a stable fashion through the system and allowing the sample to sustain increased deformation and significant loading throughout large portions of the fracture process. Furthermore, the periodic interpenetrating phases diverge and extend the crack path which will improve the fracture toughness of the IPCs.

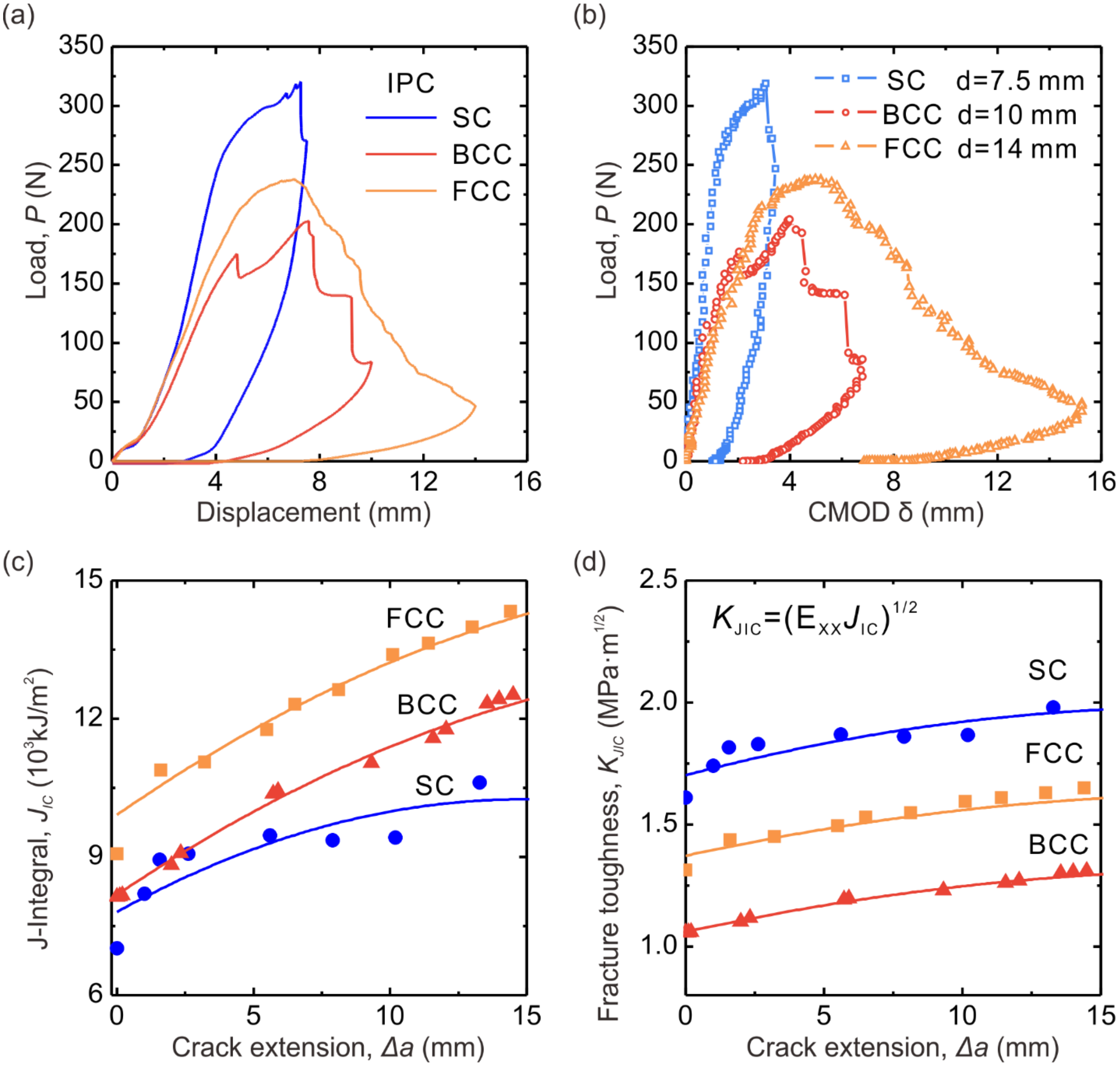

Figure 7.5 Representative responses of IPC SENB samples with SC, BCC and FCC lattice symmetries showing the load as a function of (a) the load line displacement, and (b) the crack mouth opening displacement, δ. The crack-growth (c) J-integral, JIC and (d) and fracture toughness, KJIC are plotted as a

function of crack extension, Δa, for IPC SENB samples, respectively. Lines through the data were added to aid the reader.

We have demonstrated that both intrinsic toughening mechanism (enlarging of plastic deformation of hard polymer) and extrinsic toughening mechanism (crack deflection and bridging controlled by hard polymer) are synergistically responsible for the enhanced fracture behavior of the proposed IPC composites. Typically, extrinsic toughness mechanism is effective in resisting crack propagation and is strongly dependent on the crack size. As a result, instead of a constant fracture toughness, the crack-propagation resistance curve (*R*-curve) exhibits a gradually increasing behavior as the crack advances. To further understand these two different mechanisms, we measured the materials *R*-curves for the proposed IPC composites. As shown in Figure 7.5, all of the IPCs composites with SC, BCC, and FCC lattice symmetries exhibit an increased *J*-integral as the cracks propagate. The absolute value of J-integral in FCC composite is the largest while the SC composite shows the lowest *J*-integral. Noticeably, when converting the J-integral into equivalent fracture toughness, SC composite exhibits the largest fracture toughness while FCC composite exhibit an intermediate absolute value. Yet, a gradually increasing toughness still persists in the all of these composites as the cracks propagate. These quantitative analyses indicate that extrinsic toughening mechanism induced by crack deflection and bridging of the hard polymer is dominant. Though it has been extensively demonstrated that natural structural materials such as hierarchical nacreous composites exhibit both intrinsic and extrinsic toughening mechanisms [270,271], similar toughening mechanism are achievable in rationally designed and 3D printed architected composites.

7.5.2 Comparison between fracture behavior of IPC, PC, FC, and LC

We have shown that the proposed IPCs exhibit impressive fracture behavior due to the inherent microstructures. To further support our finding, we now compare the fracture response of IPCs with several conventional composites, including particle-reinforced, fiber-reinforced, laminal-reinforced topologies. Here, we use the volume fraction of hard material 50% for each design for the purposes of fair comparison. For IPCs and PCs, we select three lattice topologies as SC, BCC, and FCC. For FCs and LCs, we select two topologies with fiber or laminal as 0° and 90°. The specific composite topology has a significant impact on the overall mechanical response of the SENB samples under three-point bending test. From the load-displacement curves (Figure 7.6 (a)), the conventional PCs, FCs and LCs exhibit relative poor mechanical behaviors compared with IPCs. This is because, in conventional composites, the matrix is soft material while the phase of the hard material is not continuous. During the fracture propagating, the crack will choose the path of least resistance which is the continuous compliant matrix. In Figure 7.6 (b), we observe that the crack propagates along the soft material in conventional composites, By contrast, the structures of 3D periodic IPCs contain continuous hard and soft materials with multiple constrains which will inhibit the crack propagation in only one phase. The fracture toughness, K_J at zero crack extension of each composite, is plotted in Figure 7.6 (b). As expected the IPCs achieve a higher fracture toughness than that of conventional PC, FC, LC composites. For example, the fracture toughness of FCC IPC is about 16 times that of FCC PC. Therefore, combining additive manufacturing methods such as 3D printing technique, we provide a new insight to design periodic IPCs with complex 3D structures to achieve enhanced fracture behaviors.

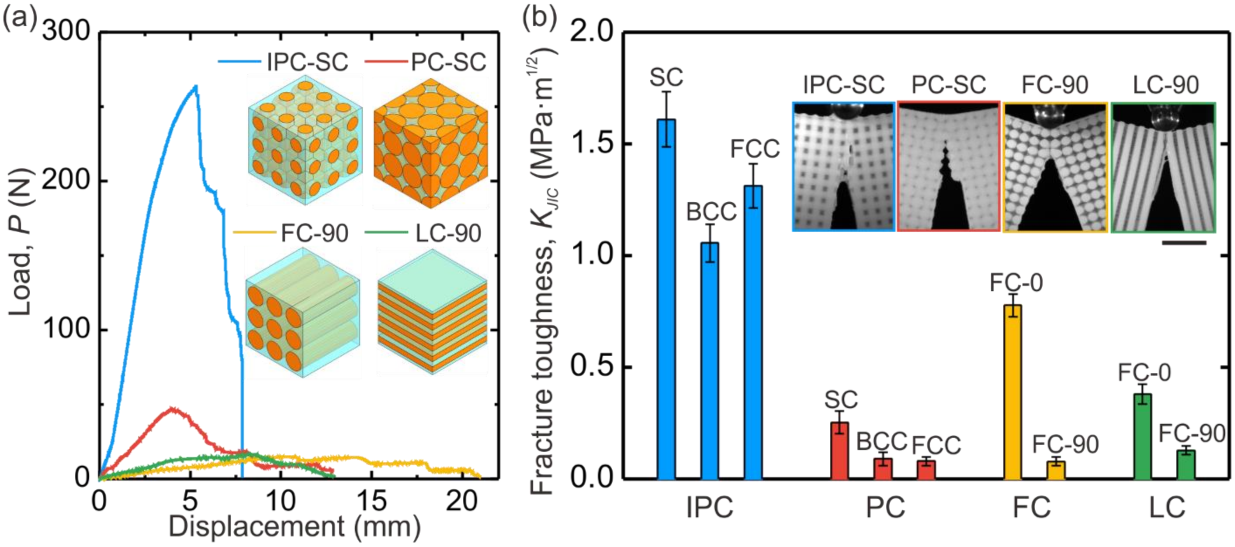

Figure 7.6 3-point bending tests of the SENB specimens of IPCs, PCs, FCs and LCs. (a) Load-displacement curves. (b) The calculated fracture toughness, K_J at zero crack extension of each IPC, PC, and LC. Images of specimens at failure strain showing the path of crack propagation for the SC IPC, SC PC, FC90, and LC90. Scale bar: 1 cm.

7.6 Tailored fracture toughness

7.6.1 Effect of material properties

3D printing technique not only enables the fabrication of complex structures in a timely and cheaply manner but also allows for manufacturing composites with various combination of compositions. It has been shown that the contrasts of the compositions have a significant impact on the mechanical response and fracture toughness. [272-274] Here we investigate the effect of stiffness ratio of two materials, E_B/E_A, on the evolution of fracture toughness. The material properties of the individual constituent materials are found by tensile testing of dogbone specimens comply with the ones prescribed by the ASTM D412 and ASTM D638 (See Experimental section for more details). Figure 7.7 (a) presents the stress-strain relations of six different constitutive materials. It is clearly noted that material *A*, *B*4, and *B*5 behave relative stiff and brittle like glassy polymers while material *B*, *B*1, *B*2, and *B*3 are complaint ductile which are rubber-like polymers. The calculated tension modulus varies from around 1 MPa to 1 GPa, result in the stiffness ratios from 0.001 to 1 as shown in Figure 7.7 (a). However, material *B*1-*B*5 are constructed from a mix of material *A* and *B* and the mixing ratios are preprogrammed in the 3D printer and cannot be changed in the current setup. Therefore, the limited selection of materials available in Objet printing system constrains the value of stiffness ratio could not reach from 0.02 to 0.8. In Figure 7.7 (b), we display the load-displacement response of SENB samples with a variety of constituent materials. The load-displacement curves indicate a wide variation of composite behavior as the constitutive behavior of the matrix (*B*) is tuned. It is clearly noticed that the composites transition in behavior from very stiff and brittle to a complaint ductile response. Moreover, the Ashby plots (Figure 7.7 (c)-(d)) showing the relationship between the fracture toughness at zero crack extension, K_{IJC}, the normalized toughness, T/T_A and the stiffness ratio, E_B/E_A, the normalized stiffness of composites E_{XX}/E_A, respectively. First, we note that the fracture toughness at zero crack extension increases with increasing the stiffness ratio. The reason for this is that here the initial fracture toughness based on ASTM E1820 is largely affected by the maximum loading force during bending tests of SENB specimens and the stiffness of the composites. Therefore, the composites with stiffer and stronger matrix materials have larger fracture toughness at zero crack extension. Nonetheless, the displayed Ashby plots exhibit different trends for the normalized toughness which is a performance of engineered composites during the whole crack propagation process before cartographical failure. We find that more compliant matrix phase is capable of creating tougher composites. This phenomenon is due to the fact that the weaker phase shifts the nature of load transfer in the composite to a more advantageous one. [272] Indeed, this mechanism has been observed in many biological materials. [275] These findings indicate that it is indeed possible to tune the interactions of the composite constituent phases through controlling the stiffness ratio to fundamentally alter the fracture mechanical properties of the composites.

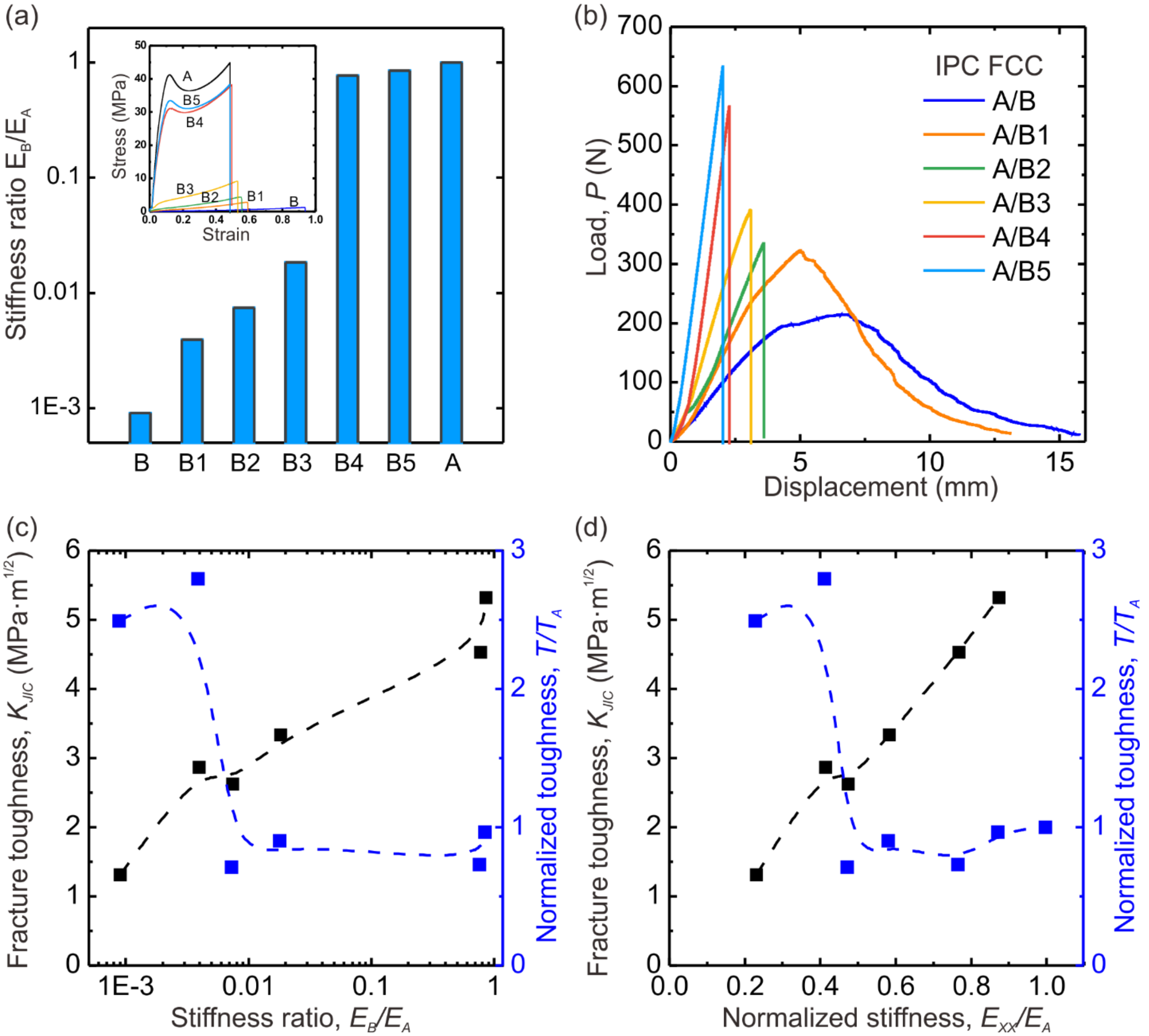

Figure 7.7 The effect of stiffness ratio, EB/EA, on the mechanical response of FCC IPCs. (a) The calculated stiffness ratio of 3D printed constitutive materials from tension tests. (b) Load-displacement curves of IPC FCC SENB specimens with a variety of constituent materials. (c) Ashby plot indicating the correlation between calculated initial fracture toughness, K_{JIC}, normalized toughness T/T_A and the stiffness ratio, E_B/E_A. (d) Ashby plot indicating the correlation between calculated initial fracture

toughness, K_{JIC}, normalized toughness T/T_A and the normalized stiffness ratio of each composite, E_{XX}/E_A. Here the volume fraction of material A is 50% for each composite.

7.6.2 Effect of volume fraction

It has been demonstrated the inherent architectures of IPC are of great importance to their fracture behavior. [244,248,249] Here we quantify the effect of volume fraction on the evolution of fracture toughness (Figure 7.8 (a)). With the increase of volume fraction of the hard material, FCC IPCs exhibit a higher fracture toughness. This is because the load is mainly carried by the glassy polymer phase so that the composites with a higher content of material A show higher stiffness and strength. For cellular materials, such as metal foams and lattice structure, the relation between the effective elastic properties such as the elastic modulus E and the relative density $\bar{\rho}$ can be described by a power law $E \sim \bar{\rho}^n$. [61] Here we use the scaling law to quantify the relation between the fracture toughness and the volume fraction of material A as $K_{JIC} = C\bar{\rho}^n$. For FCC IPCs, the scaling exponent n fitting from the experimental results equal to 1.32. This nearly linear scaling relation indicates that we can design lightweight yet toughen composites. These results suggest good ability to tailor the geometric features of architected IPCs to achieve tunable mechanical properties and fracture toughness for purposeful mechanical applications.

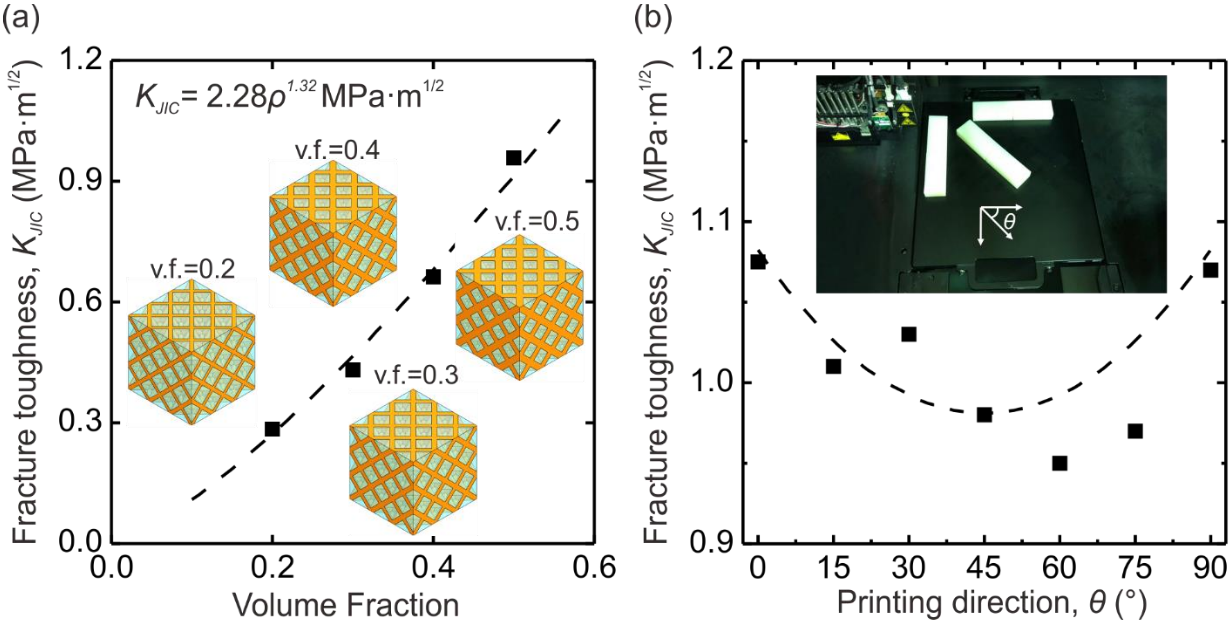

Figure 7.8 The effect of the volume fraction of material A on the mechanical response of FCC IPCs. (a) The calculated fracture toughness, K_J at zero crack extension of the FCC IPC with different volume fractions. The effect of the 3D printing direction on the mechanical response of FCC IPCs. (b) The calculated fracture toughness, K_J at zero crack extension of IPCs. The inset schematically illustrates the printing direction. The dashed line is the fitting curve.

7.6.3 Effect of 3D printing orientation

We investigate the effect of the 3D printing direction on the mechanical response and fracture toughness of SENB samples as shown in Figure 7.8 (b). It can be seen that the direction of 3D-printing clearly influenced the fracture toughness. Note that the fracture toughness for composites printed in 0° and 90° directions are almost the same, whereas the weakest direction is depicted in 45° directions. This is because 3D printing induces anisotropy. [276] The 3D printed photopolymers exhibit that the elastic behavior, yield behavior, and plastic deformation all depend on the printing direction. Moreover, the material strength is highly anisotropic, which is usually much weaker along the printing direction. Considering the anisotropy effect inherited from the layer-wise processing feature, all the 3D printed samples except these three samples are fabricated along 0° directions. This finding suggests that fracture properties of IPC can be tailored by controlling the printing directions, thereby offering opportunities to design tough composites subjected to prescribed loading directions.

7.7 Conclusion

Through integrative rational design, 3D printing, and mechanical testing, we have quantitatively demonstrated that architected IPCs show improved fracture toughness compared with other conventional composite structures. The toughening mechanism is due to the plastic deformation and stretching of the hard polymer that bridges the advancing crack, which is intrinsically controlled by the rationally designed interpenetrating architectures. A moderate increase in fracture resistance with crack growth was seen for IPCs. Though similar toughening mechanism has been reported in our previous work and other related works, the proposed IPCs with the rod-connected counterparts and their inverse domains can be designed and tailored readily compared with other IPCs. Moreover, with the advance of 3D printing, the architected IPCs proposed here exhibit tunable fracture toughness, which enables the proposed architected IPC to subject various loading conditions. Specifically, we found that the interaction between a stiff and soft phase in an IPC could be tuned to create material systems that would exhibit significant stiffness combined with superior toughness. We can envision that with the advance of additive manufacturing, it is possible to manufacture the proposed IPCs with different types of compositions at various length scales, enabling us to further explore other material properties and functionalities, such as transport, thermal, phononic, and photonic to name a few. The findings presented here open avenues to explore advanced architected composites with multifunctionalities and tailorable properties through integrating rational architecture design and the state-of-the-art manufacturing techniques.

Chapter 8. Conclusions

8.1 Main contributions

The research work presented from Chapter 2 to 7 are focused on designing, modeling, 3D printing, and mechanical testing of architected materials. The objective is to establish the relationships between the internal structure of a material and its mechanical properties and discovering existing and potential new materials, especially those with improved and even tailorable properties for potential mechanical applications. The key scientific contributions are summarized as follows:

(1) **Developed a new group of 2D and 3D stretchable lattice metamaterials with mechanically tunable negative Poisson's ratio.** Conventionally, the lattice materials are with straight ligaments which exhibit the positive or zero Poisson's ratio. However, in Chapter 3, we developed a new architected lattice material by replacing regular straight beams with sinusoidally shaped ones in plane direction. Improved stretchability is numerically and experimentally demonstrated due to the pre-curved shape. Interestingly, these proposed lattice metamaterials also exhibit a negative Poisson's ratio, indicating that the metamaterials will expand under uniaxial stretch. In Chapter 4, this design strategy can be applied in out-of-plane direction to achieve 3D planar even 3D lattice metamaterials. Because of the structure extended to the third dimension, these 3D planar lattice metamaterial can exhibit negative Poisson's ratio at any extremely large stretching deformation. Quite importantly, this significant Poisson's ratio can be tailored by tuning the parameters of ligaments and optimizing the lattice topologies. Intrinsically, these novel mechanical behaviors are attributed to the deformation pattern switching from bending-dominated to stretching-dominated behavior. These finding presented here provide new insights into development of architected metamaterials with unusual physical properties and potential

applications including energy absorption, tunable acoustics, vibration control, responsive devices, soft robotics, and stretchable electronics.

(2) Created a new class of sandwich composites with 3D printed tunable core topologies for bending behavior. In aerospace, naval, sporting and automotive industry, sandwich composite structures are widely used due to their high stiffness/weight ratio, high strength/weight ratio, and energy absorption capacity. The mechanical performance of a sandwich composite depends on the material used for construction, geometry of face sheets and especially the core topology design. Typical sandwich composite used conventional honeycomb cellular core or various truss core. In Chapter 5, we designed a new class of programmed sandwich composites contain CFRP face sheets and 3D printed core materials with truss, conventional honeycomb and re-entrant honeycomb topologies. We performed three-point bending tests to investigate the effect of face sheet materials, core topologies and core volume fraction on the bending behavior of these sandwich composites. We found that the sandwich composites with truss core materials provide highest flexural stiffness and strength that are desirable in structural components. Interesting, the sandwich composites with re-entrant honeycomb core exhibit a sequential snap-through instability which significantly enhances the energy absorption abilities. Our experimental and numerical results indicate that architected core structures can be utilized to tailor the bending properties as well as failure mechanisms. These findings offer new insights into the study of nonlinear mechanical response of sandwich structures, which can benefit a wide range of industries and applications.

(3) Applied auxetic structures to design a new system of stiffer, harder and tougher composites. Auxetic materials are a group of materials with negative Poisson's ratio. The proposed architected lattice metamaterials in Chapter 3, Chapter 4 and the re-entrant honeycomb core structures in Chapter 5 are all auxetic materials. It is noticed that most auxetic materials are cellular structures and most of them are bending or rotation dominated mechanism. Therefore, these auxetic materials or structures exhibit poorer stiffness or strength compared with conventional non-auxetic materials or structures which limited the application of auxetic materials and structures. Here, we designed a class of high-performance composites in which auxetic lattice structures are used as the reinforcements and the nearly incompressible soft material is employed as the matrix. We found that these proposed composites exhibit the auxetic behavior and enhanced stiffness, hardness and toughness compared with those composites with conventional lattice reinforcement. This improved mechanical performance is due to the negative Poisson's ratio effect of the auxetic reinforcements, which makes the matrix in a state of biaxial (2D) even triaxial (3D) compression and hence provides additional support. Moreover, we first experimentally investigated the enhanced indentation stiffness of auxetic composites due to the negative Poisson's ratio effect of the overall auxetic composites, which makes the composites denser at the site of the impact and therefore more resistant to indentation. Combining experimental tests and numerical simulation, we conclude that auxetic structures can lead to design stiffer, harder and tougher composite materials. These findings broaden the study field of auxetic materials and pave the way for developing a new class of auxetic composites for potential applications for energy absorption, impact resistant materials even multi-functional materials such as piezoelectric materials.

(4) Discovered the improved fracture toughness behavior in 3D co-continuous composites. In our previous research, 3D co-continuous composites have excellent mechanical properties, such as enhanced strength, stiffness, energy absorption, and crack resistance under compression testing. In Chapter 7, we first experimentally measured the fracture toughness of a class of co-continuous composite fabricated by 3D printing with rationally designed architectures which is 16 times that of conventionally structured composites. The toughening mechanisms arise from the plastic deformation and stretching of the hard phase that bridges the advancing crack, which is intrinsically controlled by the rationally designed interpenetrating architectures. The prominently enhanced fracture toughness in the architected IPCs can be tuned by tailoring the stiffness contrasts between the compositions, the volume fraction of each phase. The 3D co-continuous composites reported here will be particular useful in mechanically challenging environments where mechanical robustness and reliability are simultaneously pursued. The findings presented here open avenues to explore advanced architected composites with multifunctionalities and tailorable properties through integrating rational architecture design and the state-of-the-art manufacturing techniques.

8.2 Future works

Architected material design concept is a powerful tool to explore novel and unusual physical properties. The designed architected materials therefore have a wide range of promising applications, especially when design is combined with the modern manufacturing technologies like 3D printing. Some future works could be toward, but are not limited to, the following directions.

(1) **Soft active material for tunable mechanical properties:** I created a series of architected lattice materials with bi-material ligaments by harnessing the residual stress in the 3D printing process. Under environmental stimuli, such as temperature, these lattice materials deformed to the shapes with curved ligaments which are very similar to our previous designed pre-curved lattice metamaterials. And the actuated structures exhibit different mechanical properties with undeformed ones, such as NPR effect, wave propagation control, etc. Now the problem is that the heating actuated process is one way actuated and not unrecoverable. I hope in the future, it can

become a two-way actuated process. Moreover, with advanced additive manufacturing and new 3D printing materials, the environmental stimuli can be temperature, light, electric field, magnetic field, moisture, PH, etc. Therefore, I will continue working on these projects and combining the concept of 4D printing and the architected materials to create environmental stimuli mechanical metamaterials.

(2) **Reusable 3D printed materials:** Shape memory polymers (SMPs) are smart polymeric materials that have the ability to return from a deformed state to their initial shape induced by an external stimulus such as temperature. The objective of this project is using SMPs to design reusable 3D printed architected materials for structural applications. The first problem is how to design architectures to bear the maximum load by using the plastic deformation, not the failure. For example, the auxetic sandwich has less localized stress concentration resulting in no failures under bending deformation. By contrast, the hierarchical honeycomb exhibits extreme large deformation at some certain position which causes the breaks of ligaments. Therefore, the recovered auxetic sandwich keeps better structure integrity than hierarchical honeycombs which provides the potential for reuse. The second problem is how to heal the cracks occurred in the deformed SMPs**.** One example is the compression deformation and recovery of IPCs. At small deformation, the shape memory effect enables full recovery of mechanical property because of no local cracks. While at large deformation, the cracks appear in the SMPs. Although the elastomer phase provides great mechanical enhancement and additional recovery force to the composites, the cracks still exist and affect the mechanical properties for reuse. My preliminary experiments show that these cracks can be healed by using some healing agent which has strong bonding, low viscosity and long working time. The healing enables more recovery of mechanical property of these composites. For the future work in this project, I plan to combine various designed

architectures with new 3D printed materials with novel properties such as self-healing to create potentially reusable materials for mechanical applications.

(3) **Fracture behavior of 3D printed materials with novel architectures:** Composites play an important role as structural materials in a range of engineering fields due to their potential to combine the best mechanical properties of their constituents. Most of the previous research indicate that the bio-inspired composites from bone, nacre with “bricks-and-mortar” structures exhibit superior fracture mechanical properties. With multi-material 3D printing at micrometer resolution, more composites with complex structures can be fabricated to achieve enhanced mechanical properties. Compared with the usual nacre-like composites, I designed a class of interlocked bio-inspired composites which exhibit enhanced stiffness, strength, toughness and fracture toughness and this project is under working. Three-dimensional composites with co-continuous phases have shown great mechanical properties. Here, I have designed a class of 3D auxetic composites and also another series of co-continuous composites with triple periodic minimal surfaces interfaces. I plan to study the fracture behavior including the fracture toughness, fracture toughen mechanisms of these 3D printed composites by combined experimental investigation and numerical analyses.

(4) **Other future planes:**

1) Experimental investigation of the fundamental mechanics and physic of frigid temperature, UV radiation, and moisture on the mechanics of marine composites (CFRP) under static and dynamic loading conditions.
2) Lattice metamaterials with tunable negative thermal expansion.
3) Using 3D printing and SMPs to design environmental actuated fluid channels.

4) The mechanical properties of materials with aperiodic structures including the effects of defects, the topology optimized structures, functionally graded structures and random structures.
5) Architected materials with multi-functionalities focus on the thermoelectric materials, piezoelectric materials, shape memory alloy/polymer and programmable materials.

Bibliography

[1] J. Aizenberg, J. C. Weaver, M. S. Thanawala, V. C. Sundar, D. E. Morse, and P. Fratzl, Science **309**, 275 (2005).

[2] P. Vukusic and J. R. Sambles, Nature **424**, 852 (2003).

[3] K. Autumn, Y. A. Liang, S. T. Hsieh, W. Zesch, W. P. Chan, T. W. Kenny, R. Fearing, and R. J. Full, Nature **405**, 681 (2000).

[4] L. R. Meza, A. J. Zelhofer, N. Clarke, A. J. Mateos, D. M. Kochmann, and J. R. Greer, Proceedings of the National Academy of Sciences **112**, 11502 (2015).

[5] C. Coulais, E. Teomy, K. de Reus, Y. Shokef, and M. van Hecke, Nature **535**, 529 (2016).

[6] A. Sydney Gladman, E. A. Matsumoto, R. G. Nuzzo, L. Mahadevan, and J. A. Lewis, Nature Materials **15**, 413 (2016).

[7] K.-I. Jang *et al.*, Nature Communications **6**, 6566 (2015).

[8] M. Schaffner, J. A. Faber, L. Pianegonda, P. A. Rühs, F. Coulter, and A. R. Studart, Nature Communications **9**, 878 (2018).

[9] M. Koyama, Z. Zhang, M. Wang, D. Ponge, D. Raabe, K. Tsuzaki, H. Noguchi, and C. C. Tasan, Science **355**, 1055 (2017).

[10] H. Tao *et al.*, Advanced Materials **23**, 3197 (2011).

[11] T. Bückmann, N. Stenger, M. Kadic, J. Kaschke, A. Frölich, T. Kennerknecht, C. Eberl, M. Thiel, and M. Wegener, Advanced Materials **24**, 2710 (2012).

[12] J. H. Lee, J. P. Singer, and E. L. Thomas, Advanced materials **24**, 4782 (2012).

[13] S. Babaee, J. Shim, J. C. Weaver, E. R. Chen, N. Patel, and K. Bertoldi, Advanced Materials **25**, 5044 (2013).

[14] T. A. Schaedler and W. B. Carter, Annual Review of Materials Research **46**, 187 (2016).

[15] Q. Zhang, X. Xu, D. Lin, W. Chen, G. Xiong, Y. Yu, T. S. Fisher, and H. Li, Advanced Materials **28**, 2229 (2016).

[16] D. R. Smith, J. B. Pendry, and M. C. Wiltshire, Science **305**, 788 (2004).

[17] D. R. Smith and N. Kroll, Physical Review Letters **85**, 2933 (2000).

[18] J. Valentine, S. Zhang, T. Zentgraf, E. Ulin-Avila, D. A. Genov, G. Bartal, and X. Zhang, nature **455**, 376 (2008).

[19] N. Fang, D. Xi, J. Xu, M. Ambati, W. Srituravanich, C. Sun, and X. Zhang, Nature materials **5**, 452 (2006).

[20] H. Chen and C. Chan, Applied physics letters **91**, 183518 (2007).

[21] Z. Yang, H. Dai, N. Chan, G. Ma, and P. Sheng, Applied Physics Letters **96**, 041906 (2010).

[22] Y. Chen and L. Wang, Applied Physics Letters **105**, 191907 (2014).

[23] M. Kadic, T. Bückmann, N. Stenger, M. Thiel, and M. Wegener, Applied Physics Letters **100**, 191901 (2012).

[24] B. Florijn, C. Coulais, and M. van Hecke, Physical review letters **113**, 175503 (2014).

[25] X. Zheng *et al.*, Science **344**, 1373 (2014).

[26] X. Li and H. Gao, Nature materials **15**, 373 (2016).

[27] H. Yasuda and J. Yang, Physical review letters **114**, 185502 (2015).

[28] J. N. Grima, R. Caruana-Gauci, M. R. Dudek, K. W. Wojciechowski, and R. Gatt, Smart Materials and Structures **22**, 084016 (2013).

[29] K. Bertoldi, P. M. Reis, S. Willshaw, and T. Mullin, Advanced Materials **22**, 361 (2010).

[30] X. Ren, J. Shen, A. Ghaedizadeh, H. Tian, and Y. M. Xie, Smart Materials and Structures **25**, 065012 (2016).
[31] A. Ghaedizadeh, J. Shen, X. Ren, and Y. M. Xie, Materials **9**, 54 (2016).
[32] D. J. Rayneau-Kirkhope and M. A. Dias, Extreme Mechanics Letters (2016).
[33] K. E. Evans and A. Alderson, Advanced materials **12**, 617 (2000).
[34] W. Yang, Z.-M. Li, W. Shi, B.-H. Xie, and M.-B. Yang, Journal of materials science **39**, 3269 (2004).
[35] J. Grima, A. Alderson, and K. Evans, Physica status solidi (b) **242**, 561 (2005).
[36] R. Lakes, Science **235**, 1038 (1987).
[37] R. Lakes, Advanced Materials **5**, 293 (1993).
[38] R. H. Baughman, J. M. Shacklette, A. A. Zakhidov, and S. Stafström, Nature **392**, 362 (1998).
[39] J. Grima, R. Jackson, A. Alderson, and K. Evans, Advanced Materials **12**, 1912 (2000).
[40] J. N. Grima, R. Gatt, V. Zammit, J. J. Williams, K. E. Evans, A. Alderson, and R. I. Walton, Journal of Applied Physics **101**, 086102 (2007).
[41] F. Song, J. Zhou, X. Xu, Y. Xu, and Y. Bai, Physical review letters **100**, 245502 (2008).
[42] A. Yeganeh-Haeri, D. J. Weidner, and J. B. Parise, Science **257**, 650 (1992).
[43] J.-W. Jiang and H. S. Park, Nano letters **16**, 2657 (2016).
[44] J. N. Grima, S. Winczewski, L. Mizzi, M. C. Grech, R. Cauchi, R. Gatt, D. Attard, K. W. Wojciechowski, and J. Rybicki, Advanced Materials **27**, 1455 (2015).
[45] Y. Suzuki, G. Cardone, D. Restrepo, P. D. Zavattieri, T. S. Baker, and F. A. Tezcan, Nature **533**, 369 (2016).
[46] A. Slann, W. White, F. Scarpa, K. Boba, and I. Farrow, physica status solidi (b) **252**, 1533 (2015).
[47] F. Javid, E. Smith-Roberge, M. C. Innes, A. Shanian, J. C. Weaver, and K. Bertoldi, Scientific reports **5** (2015).
[48] C. Lv, D. Krishnaraju, G. Konjevod, H. Yu, and H. Jiang, Scientific reports **4** (2014).
[49] Y. Hou, R. Neville, F. Scarpa, C. Remillat, B. Gu, and M. Ruzzene, Composites Part B: Engineering **59**, 33 (2014).
[50] Y. Cho *et al.*, Proceedings of the National Academy of Sciences **111**, 17390 (2014).
[51] D. Prall and R. Lakes, International Journal of Mechanical Sciences **39**, 305 (1997).
[52] M. Bianchi, F. Scarpa, M. Banse, and C. Smith, Acta Materialia **59**, 686 (2011).
[53] L. Yang, D. Cormier, H. West, O. Harrysson, and K. Knowlson, Materials Science and Engineering: A **558**, 579 (2012).
[54] D. Li, L. Dong, and R. S. Lakes, physica status solidi (b) **250**, 1983 (2013).
[55] Y. Li, S. Luo, M. C. Yang, R. Liang, and C. Zeng, Adv Funct Mater (2016).
[56] T. Widlund, S. Yang, Y.-Y. Hsu, and N. Lu, International Journal of Solids and Structures **51**, 4026 (2014).
[57] Q. Ma, H. Cheng, K.-I. Jang, H. Luan, K.-C. Hwang, J. A. Rogers, Y. Huang, and Y. Zhang, Journal of the Mechanics and Physics of Solids **90**, 179 (2016).
[58] K.-I. Jang *et al.*, Nature communications **6** (2015).
[59] K.-I. Jang *et al.*, Nature communications **5** (2014).
[60] K. Boba, M. Bianchi, G. McCombe, R. Gatt, A. C. Griffin, R. M. Richardson, F. Scarpa, I. Hamerton, and J. N. Grima, ACS Applied Materials & Interfaces (2016).
[61] L. J. Gibson and M. F. Ashby, *Cellular solids: structure and properties* (Cambridge university press, 1999).

[62] T. A. Schaedler, A. J. Jacobsen, A. Torrents, A. E. Sorensen, J. Lian, J. R. Greer, L. Valdevit, and W. B. Carter, Science **334**, 962 (2011).
[63] L. R. Meza, S. Das, and J. R. Greer, Science **345**, 1322 (2014).
[64] J.-H. Lee, L. Wang, M. C. Boyce, and E. L. Thomas, Nano letters **12**, 4392 (2012).
[65] A. G. Evans, M. He, V. S. Deshpande, J. W. Hutchinson, A. J. Jacobsen, and W. B. Carter, International Journal of Impact Engineering **37**, 947 (2010).
[66] T. A. Schaedler, C. J. Ro, A. E. Sorensen, Z. Eckel, S. S. Yang, W. B. Carter, and A. J. Jacobsen, Advanced Engineering Materials **16**, 276 (2014).
[67] L. F. Wang and M. C. Boyce, Advanced Functional Materials **20**, 3025 (2010).
[68] M. Maldovan and E. L. Thomas, *Periodic materials and interference lithography: for photonics, phononics and mechanics* (John Wiley & Sons, 2009).
[69] G. M. Whitesides, Nature **442**, 368 (2006).
[70] C. S. Roper, R. C. Schubert, K. J. Maloney, D. Page, C. J. Ro, S. S. Yang, and A. J. Jacobsen, Advanced Materials **27**, 2479 (2015).
[71] K. J. Maloney, K. D. Fink, T. A. Schaedler, J. A. Kolodziejska, A. J. Jacobsen, and C. S. Roper, International Journal of Heat and Mass Transfer **55**, 2486 (2012).
[72] J. Grima, R. Jackson, A. Alderson, and K. E. Evans, Advanced Materials **12**, 1912 (2000).
[73] J. N. Grima, R. Gatt, V. Zammit, J. J. Williams, K. E. Evans, A. Alderson, and R. I. Walton, (AIP, 2007).
[74] Y. Suzuki, G. Cardone, D. Restrepo, P. D. Zavattieri, T. S. Baker, and F. A. Tezcan, Nature (2016).
[75] R. Lakes, Science **235**, 1038 (1987).
[76] L. J. Gibson, M. Ashby, G. Schajer, and C. Robertson, in *Proceedings of the Royal Society of London A: Mathematical, Physical and Engineering Sciences* (The Royal Society, 1982), pp. 25.
[77] A. Kolpakov, Prikl. Mat. Mekh **59**, 969 (1985).
[78] C. W. Smith, J. Grima, and K. Evans, Acta materialia **48**, 4349 (2000).
[79] Y. Jiang and Y. Li, Advanced Engineering Materials (2016).
[80] K. Wojciechowski, Physics Letters A **137**, 60 (1989).
[81] A. Pozniak and K. Wojciechowski, physica status solidi (b) **251**, 367 (2014).
[82] G. W. Milton, Journal of the Mechanics and Physics of Solids **61**, 1543 (2013).
[83] C. Lv, D. Krishnaraju, G. Konjevod, H. Yu, and H. Jiang, Scientific reports **4**, 5979 (2014).
[84] S. Shan, S. H. Kang, Z. Zhao, L. Fang, and K. Bertoldi, Extreme Mechanics Letters **4**, 96 (2015).
[85] Y. Tang and J. Yin, Extreme Mechanics Letters **12**, 77 (2017).
[86] G. Wu, Y. Cho, I. S. Choi, D. Ge, J. Li, H. N. Han, T. Lubensky, and S. Yang, Advanced Materials **27**, 2747 (2015).
[87] Y. Tang, G. Lin, L. Han, S. Qiu, S. Yang, and J. Yin, Advanced Materials **27**, 7181 (2015).
[88] Y. Prawoto, Computational Materials Science **58**, 140 (2012).
[89] U. D. Larsen, O. Signund, and S. Bouwsta, Journal of Microelectromechanical Systems **6**, 99 (1997).
[90] K. E. Evans, M. Nkansah, and I. Hutchinson, (1991).
[91] J. N. Grima, R. Gatt, A. Alderson, and K. Evans, Molecular Simulation **31**, 925 (2005).

[92] R. Brighenti, A. Spagnoli, M. Lanfranchi, and F. Soncini, Fatigue & Fracture of Engineering Materials & Structures (2016).
[93] N. Gaspar, X. Ren, C. W. Smith, J. Grima, and K. E. Evans, Acta Materialia **53**, 2439 (2005).
[94] J. N. Grima and K. E. Evans, Journal of materials science **41**, 3193 (2006).
[95] D. Attard and J. N. Grima, physica status solidi (b) **245**, 2395 (2008).
[96] J. Shim, C. Perdigou, E. R. Chen, K. Bertoldi, and P. M. Reis, Proceedings of the National Academy of Sciences **109**, 5978 (2012).
[97] L. Cabras and M. Brun, in *Proceedings of the Royal Society of London A: Mathematical, Physical and Engineering Sciences* (The Royal Society, 2014), p. 20140538.
[98] K. Boba, M. Bianchi, G. McCombe, R. Gatt, A. C. Griffin, R. M. Richardson, F. Scarpa, I. Hamerton, and J. N. Grima, ACS Applied Materials & Interfaces **8**, 20319 (2016).
[99] Y. Chen, T. Li, F. Scarpa, and L. Wang, Physical Review Applied **7**, 024012 (2017).
[100] C. S. Ha, M. E. Plesha, and R. S. Lakes, Smart Materials and Structures **25**, 054005 (2016).
[101] H. Tanaka, K. Suga, N. Iwata, and Y. Shibutani, Scientific Reports **7** (2017).
[102] F. Warmuth, F. Osmanlic, L. Adler, M. A. Lodes, and C. Körner, Smart Materials and Structures **26**, 025013 (2016).
[103] P. Vogiatzis, S. K. Chen, X. Wang, T. T. Li, and L. F. Wang, Comput Aided Design **83**, 15 (2017).
[104] H. Tan, L. Yu, and Z. Zhou, physica status solidi (b) (2017).
[105] S. Timoshenko and J. M. Gere, Inc., New YorM~ 1936, 371 (1936).
[106] D. G. Fertis, *Nonlinear mechanics* (CRC Press, 1998).
[107] K. Lin and C. Lin, International Journal of Non-Linear Mechanics **46**, 1293 (2011).
[108] C. Thurnherr, L. Ruppen, G. Kress, and P. Ermanni, Composite Structures **157**, 244 (2016).
[109] T. A. Schaedler and W. B. Carter, Annual Review of Materials Research **46**, 187 (2016).
[110] D. Zenkert and I. Nordisk, *The handbook of sandwich construction* (Engineering Materials Advisory Services Ltd. (EMAS), Cradley Heath, West Midlands, 1997).
[111] H. G. Allen, *Analysis and Design of Structural Sandwich Panels: The Commonwealth and International Library: Structures and Solid Body Mechanics Division* (Elsevier, 2013).
[112] T. C. Triantafillou and L. J. Gibson, Materials Science and Engineering **95**, 37 (1987).
[113] M. F. Ashby, *Metal foams : a design guide* (Butterworth-Heinemann, Boston, 2000).
[114] W. S. Burton and A. K. Noor, Computer Methods in Applied Mechanics and Engineering **145**, 341 (1997).
[115] H. J. Rathbun *et al.*, International Journal of Solids and Structures **43**, 1746 (2006).
[116] A. Petras and M. P. F. Sutcliffe, Composite Structures **44**, 237 (1999).
[117] B. L. Buitrago, C. Santiuste, S. Sánchez-Sáez, E. Barbero, and C. Navarro, Composite Structures **92**, 2090 (2010).
[118] I. G. Masters and K. E. Evans, Composite Structures **35**, 403 (1996).
[119] W. Becker, Composite Structures **48**, 67 (2000).
[120] F. Meraghni, F. Desrumaux, and M. L. Benzeggagh, Composites Part A: Applied Science and Manufacturing **30**, 767 (1999).
[121] H. Hu, S. Belouettar, E. M. Daya, and M. Potier-Ferry, Journal of Sandwich Structures and Materials **8**, 477 (2006).
[122] D. J. Sypeck, Applied Composite Materials **12**, 229 (2005).

[123] D. J. Sypeck and H. N. G. Wadley, Advanced Engineering Materials **4**, 759 (2002).
[124] Y. Hu, W. Li, X. An, and H. Fan, Composites Science and Technology **125**, 114 (2016).
[125] H. Wadley, Composites Science and Technology **63**, 2331 (2003).
[126] N. A. Fleck and I. Sridhar, Composites Part A: Applied Science and Manufacturing **33**, 353 (2002).
[127] F. Cote, R. Biagi, H. Bart-Smith, and V. S. Deshpande, International Journal of Solids and Structures **44**, 3533 (2007).
[128] J. Xiong, L. Ma, S. Pan, L. Wu, J. Papadopoulos, and A. Vaziri, Acta Materialia **60**, 1455 (2012).
[129] T. George, V. S. Deshpande, and H. N. G. Wadley, Composites Part A: Applied Science and Manufacturing **47**, 31 (2013).
[130] R. S. Lakes and K. Elms, Journal of Composite Materials **27**, 1193 (1993).
[131] R. Lakes, Science **235**, 1038 (1987).
[132] J. N. Grima and K. E. Evans, Journal of Materials Science Letters **19**, 1563 (2000).
[133] J. B. Choi and R. S. Lakes, International Journal of Fracture **80**, 73 (1996).
[134] K. E. Evans, Endeavour **15**, 170 (1991).
[135] A. Alderson and K. L. Alderson, Proceedings of the Institution of Mechanical Engineers, Part G: Journal of Aerospace Engineering **221**, 565 (2007).
[136] S. Mohsenizadeh, R. Alipour, M. Shokri Rad, A. Farokhi Nejad, and Z. Ahmad, Materials & Design **88**, 258 (2015).
[137] S. Hou, T. Liu, Z. Zhang, X. Han, and Q. Li, Materials & Design **82**, 247 (2015).
[138] J. P. M. Whitty, A. Alderson, P. Myler, and B. Kandola, Composites Part A: Applied Science and Manufacturing **34**, 525 (2003).
[139] F. Scarpa, L. G. Ciffo, and J. R. Yates, Smart Materials and Structures **13**, 49 (2004).
[140] K. E. Evans and K. L. Alderson, Engineering Science and Education Journal **9**, 148 (2000).
[141] A. Alderson, K. L. Alderson, G. Chirima, N. Ravirala, and K. M. Zied, Composites Science and Technology **70**, 1034 (2010).
[142] C. P. Chen and R. S. Lakes, Journal of Engineering Materials and Technology **118**, 285 (1996).
[143] J. Lee, J. B. Choi, and K. Choi, Journal of Materials Science **31**, 4105 (1996).
[144] D. U. Yang, S. Lee, and F. Y. Huang, Finite Elements in Analysis and Design **39**, 187 (2003).
[145] S. Gonella and M. Ruzzene, International Journal of Solids and Structures **45**, 2897 (2008).
[146] M. Assidi and J.-F. Ganghoffer, Composite Structures **94**, 2373 (2012).
[147] S. Yang, C. Qi, D. Wang, R. Gao, H. Hu, and J. Shu, Advances in Mechanical Engineering **5** (2013).
[148] H. Wan, H. Ohtaki, S. Kotosaka, and G. Hu, European Journal of Mechanics - A/Solids **23**, 95 (2004).
[149] M. H. Fu, O. T. Xu, L. L. Hu, and T. X. Yu, International Journal of Solids and Structures **80**, 284 (2016).
[150] F. Scarpa and G. Tomlinson, Journal of Sound and Vibration **230**, 45 (2000).
[151] C. Lira and F. Scarpa, Composites Science and Technology **70**, 930 (2010).
[152] Y. Hou, Y. H. Tai, C. Lira, F. Scarpa, J. R. Yates, and B. Gu, Composites Part A: Applied Science and Manufacturing **49**, 119 (2013).

[153] G. Imbalzano, P. Tran, T. D. Ngo, and P. V. Lee, Journal of Sandwich Structures and Materials, 1099636215618539 (2015).
[154] G. Imbalzano, P. Tran, T. D. Ngo, and P. V. Lee, Composite Structures **135**, 339 (2016).
[155] L. Yang, O. Harrysson, H. West, and D. Cormier, Materials Sciences and Applications **Vol.04No.08**, 7, 35338 (2013).
[156] P. Vogiatzis, S. Chen, X. Wang, T. Li, and L. Wang, Comput Aided Design **83**, 15 (2017).
[157] Z. Zhou, J. Zhou, and H. Fan, Materials Science and Engineering: A **688**, 123 (2017).
[158] J. Prasad and A. R. Diaz, Journal of Mechanical Design **128**, 1298 (2005).
[159] D. M. Correa, T. Klatt, S. Cortes, M. Haberman, D. Kovar, and C. Seepersad, Rapid Prototyping Journal **21**, 193 (2015).
[160] S. Shan, S. H. Kang, J. R. Raney, P. Wang, L. Fang, F. Candido, J. A. Lewis, and K. Bertoldi, Advanced Materials **27**, 4296 (2015).
[161] A. Rafsanjani, A. Akbarzadeh, and D. Pasini, Advanced Materials **27**, 5931 (2015).
[162] Y. Liu, T. A. Schaedler, and X. Chen, Mechanics of Materials **77**, 1 (2014).
[163] J. H. Lee, L. F. Wang, M. C. Boyce, and E. L. Thomas, Nano Letters **12**, 4392 (2012).
[164] J. Xu, Y. Li, Y. Xiang, and X. Chen, Nanoscale Research Letters **8**, 54 (2013).
[165] S. Yin, J. Li, B. Liu, K. Meng, Y. Huan, S. R. Nutt, and J. Xu, Composite Structures **160**, 1147 (2017).
[166] M. F. Ashby, Philosophical Transactions of the Royal Society A: Mathematical, Physical and Engineering Sciences **364**, 15 (2006).
[167] Y. Liu, T. A. Schaedler, A. J. Jacobsen, and X. Chen, Composites Part B: Engineering **67**, 39 (2014).
[168] A. Mouritz, E. Gellert, P. Burchill, and K. Challis, Composite structures **53**, 21 (2001).
[169] S. C. Han, J. W. Lee, and K. Kang, Advanced Materials **27**, 5506 (2015).
[170] D. W. Abueidda, M. Bakir, R. K. Abu Al-Rub, J. S. Bergström, N. A. Sobh, and I. Jasiuk, Materials & Design **122**, 255 (2017).
[171] Z. Qin, G. S. Jung, M. J. Kang, and M. J. Buehler, Science Advances **3**, e1601536 (2017).
[172] Y. Liu, T. A. Schaedler, A. J. Jacobsen, W. Lu, Y. Qiao, and X. Chen, Composite Structures **115**, 29 (2014).
[173] J. Zhou, X. Deng, Y. Yan, X. Chen, and Y. Liu, Composite Structures **131**, 966 (2015).
[174] L. Wang, J. Lau, E. L. Thomas, and M. C. Boyce, Advanced Materials **23**, 1524 (2011).
[175] Y. Liu and L. Wang, Composite Structures **128**, 274 (2015).
[176] R. H. Baughman, J. M. Shacklette, A. A. Zakhidov, and S. Stafstrom, Nature **392**, 362 (1998).
[177] J. N. Grima, R. Jackson, A. Alderson, and K. E. Evans, Advanced Materials **12**, 1912 (2000).
[178] A. Yeganeh-Haeri, D. J. Weidner, and J. B. Parise, Science **257**, 31 (1992).
[179] Y. Suzuki, G. Cardone, D. Restrepo, P. D. Zavattieri, T. S. Baker, and F. A. Tezcan, Nature **533**, 369 (2016).
[180] R. Lakes and K. Elms, Journal of Composite Materials **27**, 1193 (1993).
[181] J. Choi and R. Lakes, International Journal of fracture **80**, 73 (1996).
[182] A. Alderson and K. Alderson, Proceedings of the Institution of Mechanical Engineers, Part G: Journal of Aerospace Engineering **221**, 565 (2007).

[183] S. Mohsenizadeh, R. Alipour, M. S. Rad, A. F. Nejad, and Z. Ahmad, Materials & Design **88**, 258 (2015).
[184] T. Li and L. Wang, Composite Structures **175**, 46 (2017).
[185] Z. Wang and H. Hu, Textile Research Journal **84**, 1600 (2014).
[186] Z. Ge and H. Hu, Textile Research Journal **83**, 543 (2013).
[187] Y. Liu, H. Hu, J. K. Lam, and S. Liu, Textile Research Journal **80**, 856 (2010).
[188] H. Hu, Z. Wang, and S. Liu, Textile research journal **81**, 1493 (2011).
[189] Z.-D. Ma, H. Bian, C. Sun, G. M. Hulbert, K. Bishnoi, and F. Rostam-Abadi, Functionally-graded NPR (negative Poisson's ratio) material for a blast-protective deflector, 2010.
[190] G. Stavroulakis, physica status solidi (b) **242**, 710 (2005).
[191] Z.-D. Ma, Y. Liu, X. Liu, C. Sun, and Y. Cui, (Google Patents, 2013).
[192] F. Scarpa, IEEE Signal Processing Magazine **25**, 128 (2008).
[193] Y. Liu and H. Hu, Scientific Research and Essays **5**, 1052 (2010).
[194] Q. Liu, Literature review: materials with negative Poisson's ratios and potential applications to aerospace and defence, 2006.
[195] K. W. Wojciechowski, Molecular Physics **61**, 1247 (1987).
[196] A. A. Pozniak, J. Smardzewski, and K. W. Wojciechowski, Smart Materials and Structures **22**, 084009 (2013).
[197] K. El Nady, F. Dos Reis, and J. F. Ganghoffer, Composite Structures **170**, 271 (2017).
[198] Y. Jiang and Y. Li, Advanced Engineering Materials **19** (2017).
[199] K. ElNady, I. Goda, and J.-F. Ganghoffer, Computational Mechanics **58**, 957 (2016).
[200] N. Karathanasopoulos, H. Reda, and J.-f. Ganghoffer, Computational Materials Science **138**, 323 (2017).
[201] J. N. Grima, A. Alderson, and K. Evans, Physica status solidi (b) **242**, 561 (2005).
[202] V. V. Novikov and K. W. Wojciechowski, Physics of the Solid State **41**, 1970 (1999).
[203] P. M. Pigłowski, J. W. Narojczyk, A. A. Poźniak, K. W. Wojciechowski, and K. V. Tretiakov, Materials **10**, 1338 (2017).
[204] T. C. Lim, physica status solidi (RRL)-Rapid Research Letters (2017).
[205] V. Simkins, A. Alderson, P. Davies, and K. Alderson, Journal of materials science **40**, 4355 (2005).
[206] K. Alderson, V. Simkins, V. Coenen, P. Davies, A. Alderson, and K. Evans, physica status solidi (b) **242**, 509 (2005).
[207] S. Jayanty, J. Crowe, and L. Berhan, physica status solidi (b) **248**, 73 (2011).
[208] Z. Ge, H. Hu, and Y. Liu, Smart Materials and Structures **22**, 084005 (2013).
[209] L. Zhou, L. Jiang, and H. Hu, physica status solidi (b) **253**, 1331 (2016).
[210] A. A. Poźniak, K. W. Wojciechowski, J. N. Grima, and L. Mizzi, Composites Part B: Engineering **94**, 379 (2016).
[211] X. Wang, M. Jiang, Z. Zhou, J. Gou, and D. Hui, Composites Part B: Engineering **110**, 442 (2017).
[212] T. Fíla, P. Zlámal, O. Jiroušek, J. Falta, P. Koudelka, D. Kytýř, T. Doktor, and J. Valach, Advanced Engineering Materials (2017).
[213] R. Zhang, H.-L. Yeh, and H.-Y. Yeh, Journal of Reinforced Plastics and Composites **17**, 1651 (1998).
[214] P. Zhang and A. C. To, International Journal of Plasticity **80**, 56 (2016).

[215] E. M. Arruda and M. C. Boyce, Journal of the Mechanics and Physics of Solids **41**, 389 (1993).
[216] I. Masters and K. Evans, Composite structures **35**, 403 (1996).
[217] H. M. A. Kolken and A. A. Zadpoor, RSC Advances **7**, 5111 (2017).
[218] M. Ashby, Philosophical Transactions of the Royal Society of London A: Mathematical, Physical and Engineering Sciences **364**, 15 (2006).
[219] H. Tanaka, K. Suga, N. Iwata, and Y. Shibutani, Scientific reports **7**, 39816 (2017).
[220] T. Li, X. Hu, Y. Chen, and L. Wang, Scientific Reports **7**, 8949 (2017).
[221] J.-H. Lee, L. Wang, S. Kooi, M. C. Boyce, and E. L. Thomas, Nano letters **10**, 2592 (2010).
[222] Y. L. Liu and L. F. Wang, Composite Structures **128**, 274 (2015).
[223] T. J. Horn and O. L. Harrysson, Science progress **95**, 255 (2012).
[224] O. Cansizoglu, O. Harrysson, D. Cormier, H. West, and T. Mahale, Materials Science and Engineering: A **492**, 468 (2008).
[225] K. Leuven, Journal of Ceramic Science and Technology **5**, 245 (2014).
[226] A. Zocca, P. Colombo, C. M. Gomes, and J. Günster, Journal of the American Ceramic Society **98**, 1983 (2015).
[227] A. Szczurek, A. Ortona, L. Ferrari, E. Rezaei, G. Medjahdi, V. Fierro, D. Bychanok, P. Kuzhir, and A. Celzard, Carbon **88**, 70 (2015).
[228] Z. C. Eckel, C. Zhou, J. H. Martin, A. J. Jacobsen, W. B. Carter, and T. A. Schaedler, Science **351**, 58 (2016).
[229] G. X. Gu, M. Takaffoli, and M. J. Buehler, Advanced Materials **29** (2017).
[230] D. R. Clarke, Journal of the American Ceramic Society **75**, 739 (1992).
[231] L. Wegner and L. Gibson, International Journal of Mechanical Sciences **42**, 925 (2000).
[232] L. Wegner and L. Gibson, International journal of mechanical sciences **42**, 943 (2000).
[233] L. Wegner and L. Gibson, International Journal of Mechanical Sciences **43**, 1061 (2001).
[234] Y. H. Ha, R. A. Vaia, W. F. Lynn, J. P. Costantino, J. Shin, A. B. Smith, P. T. Matsudaira, and E. L. Thomas, Advanced Materials **16**, 1091 (2004).
[235] E. Hamed, E. Novitskaya, J. Li, P.-Y. Chen, I. Jasiuk, and J. McKittrick, Acta biomaterialia **8**, 1080 (2012).
[236] C. J. Hansen, W. Wu, K. S. Toohey, N. R. Sottos, S. R. White, and J. A. Lewis, Advanced Materials **21**, 4143 (2009).
[237] R. Jhaver and H. Tippur, Materials Science and Engineering: A **499**, 507 (2009).
[238] Z. Poniznik, V. Salit, M. Basista, and D. Gross, Computational Materials Science **44**, 813 (2008).
[239] X.-Q. Feng, Y.-W. Mai, and Q.-H. Qin, Computational Materials Science **28**, 486 (2003).
[240] R. J. Moon, M. Tilbrook, M. Hoffman, and A. Neubrand, Journal of the American Ceramic Society **88**, 666 (2005).
[241] L. Wang, J. Lau, E. L. Thomas, and M. C. Boyce, Advanced Materials **23**, 1524 (2011).
[242] C. Periasamy and H. Tippur, Mechanics Research Communications **43**, 57 (2012).
[243] A. Agarwal, I. Singh, and B. Mishra, Composites Part B: Engineering **51**, 327 (2013).
[244] G. Li, X. Zhang, Q. Fan, L. Wang, H. Zhang, F. Wang, and Y. Wang, Acta Materialia **78**, 190 (2014).
[245] D. W. Abueidda, A. S. Dalaq, R. K. A. Al-Rub, and I. Jasiuk, Composite Structures **133**, 85 (2015).

[246] H. Cho, J. C. Weaver, E. Pöselt, M. C. Boyce, and G. C. Rutledge, Advanced Functional Materials **26**, 6938 (2016).
[247] K. Wei, H. Chen, Y. Pei, and D. Fang, Journal of the Mechanics and Physics of Solids **86**, 173 (2016).
[248] T. Etter, J. Kuebler, T. Frey, P. Schulz, J. Löffler, and P. Uggowitzer, Materials Science and Engineering: A **386**, 61 (2004).
[249] M. Gao, Y. Pan, F. Oliveira, J. Baptista, and J. Vieira, Materials letters **58**, 1761 (2004).
[250] L. Valdevit, A. J. Jacobsen, J. R. Greer, and W. B. Carter, Journal of the American Ceramic Society **94** (2011).
[251] B. Haghpanah, L. Salari‐Sharif, P. Pourrajab, J. Hopkins, and L. Valdevit, Advanced Materials **28**, 7915 (2016).
[252] G. Bullegas, S. T. Pinho, and S. Pimenta, Composites Science and Technology **131**, 110 (2016).
[253] A. S. Dalaq, D. W. Abueidda, R. K. A. Al-Rub, and I. M. Jasiuk, International Journal of Solids and Structures **83**, 169 (2016).
[254] D. W. Abueidda, A. S. Dalaq, R. K. A. Al-Rub, and H. A. Younes, International Journal of Mechanical Sciences **92**, 80 (2015).
[255] D. W. Abueidda, R. K. A. Al-Rub, A. S. Dalaq, H. A. Younes, A. A. Al Ghaferi, and T. K. Shah, Composites Science and Technology **118**, 127 (2015).
[256] B. G. Compton and J. A. Lewis, Advanced materials **26**, 5930 (2014).
[257] L. S. Dimas, G. H. Bratzel, I. Eylon, and M. J. Buehler, Advanced Functional Materials **23**, 4629 (2013).
[258] Y. Swolfs and S. T. Pinho, in *Proceedings of the 31st Technical Conference of the American Society for Composites* (DESTech Publications, 2016), pp. 1.
[259] S. Hong, D. Sycks, H. F. Chan, S. Lin, G. P. Lopez, F. Guilak, K. W. Leong, and X. Zhao, Advanced Materials **27**, 4035 (2015).
[260] O. Al-Ketana, M. A. Assada, and R. K. A. Al-Ruba, (2016).
[261] O. Al-Ketan, R. K. A. Al-Rub, and R. Rowshan, Advanced Materials Technologies **2**, 1600235, 1600235 (2017).
[262] A. S. Dalaq, D. W. Abueidda, and R. K. A. Al-Rub, Composites Part A: Applied Science and Manufacturing **84**, 266 (2016).
[263] G. X. Gu, M. Takaffoli, and M. J. Buehler, Advanced Materials, 1700060, 1700060.
[264] D. W. Abueidda, R. K. Abu Al-Rub, A. S. Dalaq, H. A. Younes, A. A. Al Ghaferi, and T. K. Shah, Composites Science and Technology **118**, 127 (2015).
[265] O. Al-Ketan, M. Adel Assad, and R. K. Abu Al-Rub, Composite Structures **176**, 9 (2017).
[266] D. W. Abueidda, A. S. Dalaq, R. K. Abu Al-Rub, and H. A. Younes, International Journal of Mechanical Sciences **92**, 80 (2015).
[267] A. S. Dalaq, D. W. Abueidda, R. K. Abu Al-Rub, and I. M. Jasiuk, International Journal of Solids and Structures **83**, 169 (2016).
[268] C. Bonatti and D. Mohr, International Journal of Plasticity **92**, 122 (2017).
[269] L. Ai and X.-L. Gao, Mechanics of Advanced Materials and Structures, 1 (2016).
[270] D. Sen and M. J. Buehler, Scientific Reports **1**, 35 (2011).
[271] U. G. K. Wegst, H. Bai, E. Saiz, A. P. Tomsia, and R. O. Ritchie, Nature Materials **14**, 23 (2014).
[272] L. S. Dimas and M. J. Buehler, Soft Matter **10**, 4436 (2014).

[273] P. Murali, T. K. Bhandakkar, W. L. Cheah, M. H. Jhon, H. Gao, and R. Ahluwalia, Physical Review E **84**, 015102 (2011).
[274] P. Fratzl, H. S. Gupta, F. D. Fischer, and O. Kolednik, Advanced Materials **19**, 2657 (2007).
[275] U. G. Wegst, H. Bai, E. Saiz, A. P. Tomsia, and R. O. Ritchie, Nature materials **14**, 23 (2015).
[276] P. Zhang and A. C. To, International Journal of Plasticity **80**, 56 (2016).